Design and characterization of a test facility for large angle diffusers

H.B. Bijvoet

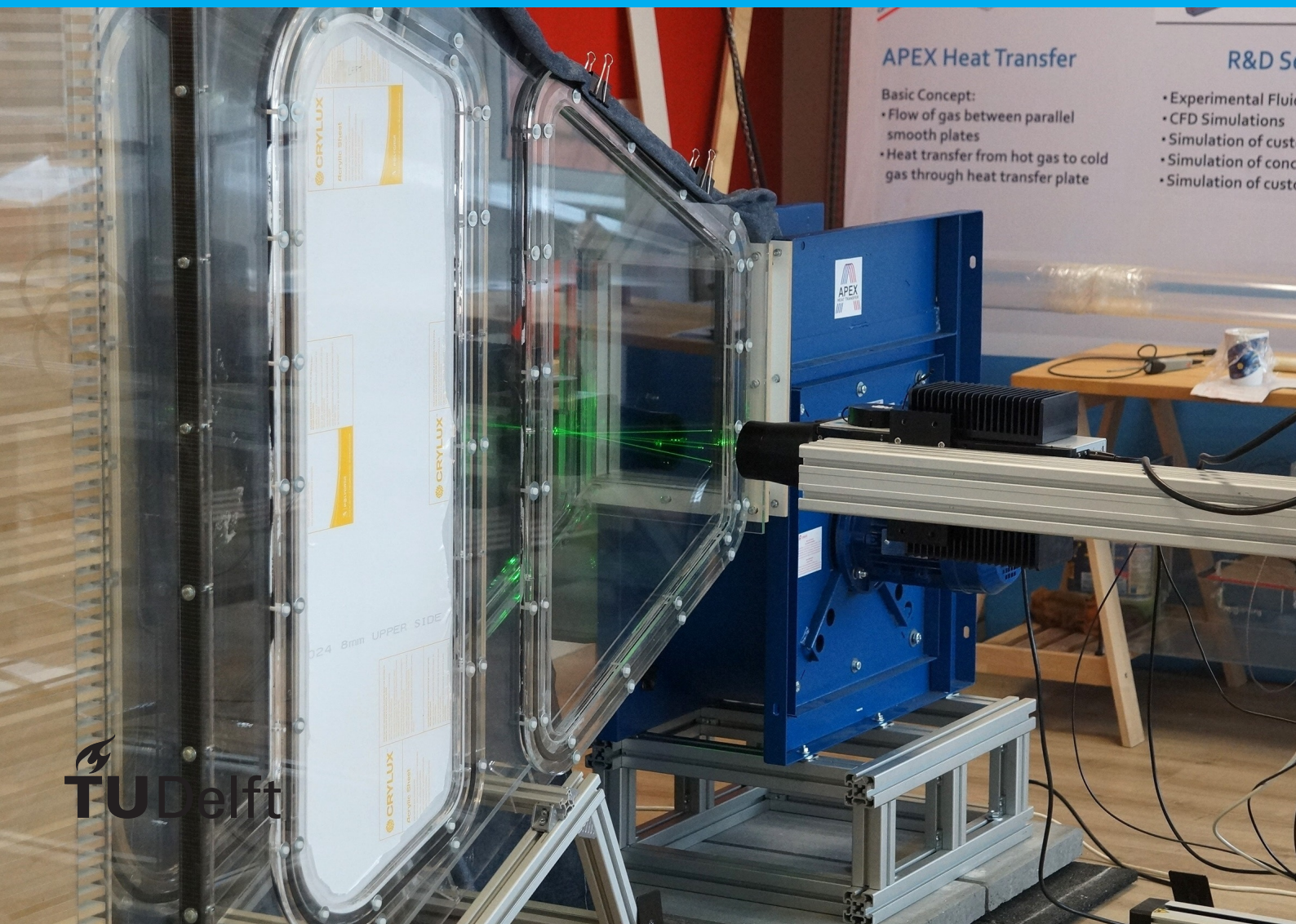

TU Delft

Design and characterization of a test facility for large angle diffusers

by

H.B. Bijvoet

to obtain the degree of Master of Science
at the Delft University of Technology,
to be defended publicly on Wednesday July 3, 2019 at 14:00.

Student number:	4165470	
Project duration:	May 17, 2018 – July 3, 2019	
Thesis committee:	Dr. ir. R. Delfos,	TU Delft, supervisor
	Dr. ir. J. Kitzhofer,	Apex Group, supervisor
	Prof. dr. ir. S. Klein,	TU Delft
	Dr. ir. G. Elsinga,	TU Delft

An electronic version of this thesis is available at http://repository.tudelft.nl/.

TU Delft

Nomenclature

Table 1: Overview of symbols used throughout this work.

Symbol	Definition	Units
A	Cross sectional area	m^2
b	Diffuser width	m
C_p	Static pressure recovery coefficient	-
D_h	Hydraulic diameter	m
f	Frequency	Hz
L	Diffuser centerline length	m
p	Static pressure	Pa
Q	Volume flow rate	m^3/s
T	Temperature	$^\circ C$ or K
t	Time	s or min
U	Velocity vector in Cartesian grid (u, v, w)	m/s
$\bar{u}$	Spatial mean velocity, over cross section (either normal average or bulk average)	m/s
u_{mean}	Temporal mean velocity	m/s
u, v, w	Velocity components in Cartesian grid	m/s
W	Diffuser height (length in plane in which channel diverges)	m
$\dot{W}$	Work	W
Greek alphabet:		
β	Perforated plate porosity	-
δ_1	Displacement thickness	-
η	Static pressure recovery efficiency	%
θ	Diffuser half angle	$^\circ$
μ	Dynamic viscosity	$kg/m/s$
ν	Kinematic viscosity	m^2/s
ρ	Density	kg/m^3
σ	Standard deviation	depends
ψ	Diffuser double angle	$^\circ$
Subscripts & superscripts		
1	Diffuser throat	
2	Diffuser outlet	
$*$	Ideal value	
$\dot{}$ (dot above symbol)	Indicates time rate of change	s^{-1}

Contents

1

Introduction

In heavy duty industry, such as the petro-chemical industry, fired heaters are used extensively to heat process fluids and to generate steam. Fired heaters are responsible for a large part of the energy consumption of the process industry. In these large pieces of equipment fossil fuels are burned and energy is transferred from the hot flue gasses to the *process fluid*. Fired heaters should be designed as fuel efficiently as possible. Reduced emission of CO_2, delayed depletion of natural resources are amongst the motives for high fuel efficiency, as well as economical aspects. Three different possible designs for fired heaters will be discussed below, they are shown in Figure 1.1. The most elementary design has only of a radiant section (Remster et al., 2013), case *I* in the figure. Down low in the heater the fuel is burned. The process fluid flows through tubes that are surrounded with the rising flue gas. Through radiation energy is transferred. These heaters have an overall thermal efficiency of up to 57.4 %. Besides a radiant section, the configuration of case *II* also has a convection section. Here, at lower temperature heat is transferred from the flue gas to the process fluid. This lowers the stack temperature and increases the thermal efficiency to at most 83.6 %.

For case *III* the highest efficiency is obtained with another upgrade; in an air-preheater at even lower temperature heat is transferred. This time however, heat is transferred to the combustion air instead of the process fluid. The complexity of the system does increase as the upgrade also requires two additional fans. The overall thermal efficiency can be as high as 92.4 %, making the upgrade worth the investment and the added complexity.

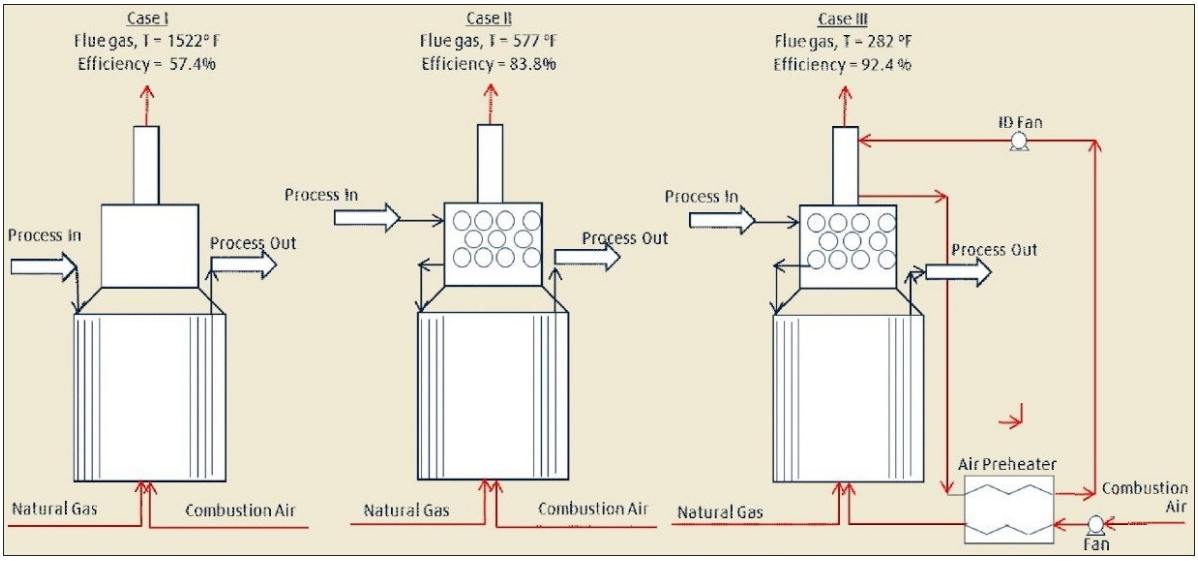

Figure 1.1: Overview of three configurations used for fired heaters. Fired heaters with a radiant coil, a convection coil and an air preheater have the best performance.

For this application generally plate type heat exchangers are used, with flat plates. Via forced draft ambient air is fed through the heat exchanger that can have a height of 15 m. For their size these heat exchangers require only a small flow rate, and so a single relatively small fan is used to drive the flow. The air is transported from the fan (rectangular outlet) to the air preheater (rectangular inlet) with a transition duct that has an increasing cross section, i.e. a diffuser. Often in industry floor space is limited and so often these diffusers have to be short. Limited floor space, ónly limited floor space can explain why in industry these *large angle diffusers* are used. Namely, the geometry of a large angle diffuser is such that high energy losses occur in them, and that a non-uniform flow enters the heat exchanger. This has several negative effects, both in the diffuser itself and the air preheater:

It in theory reduces the desired pressure increase over the diffuser (high pressure acts as the driving force for the flow through the air preheater its channels). Furthermore the non-uniform flow lowers the heat transfer duty in the air preheater and is a cause for non-uniform corrosion and plugging. This will be elaborated on in Chapter 2.

Since some 60 years, research has been done on diffusers in general. One fundamental difference between diffusers studied and diffusers seen in industry, is the velocity profile at the diffuser throat. In previous studies there is a uniform, or symmetric velocity profile at the diffuser throat, however the velocity profile emerging from a centrifugal fan is not at all uniform. For this reason it is hard to make a prediction of the systems performance based on literature. This research focuses on systems consisting of a centrifugal fan that blows

(a) Picture of a (flat) plate type heat exchanger, with application to air preheating of a fired heater.

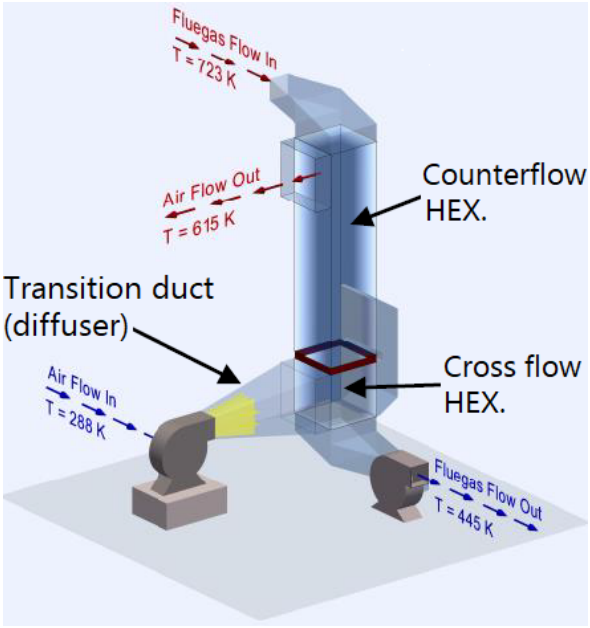

(b) Schematic representation of a centrifugal fan, diffuser and an air preheater.

Figure 1.2

ambient air into a large angle diffuser with rectangular cross sections. The two goals of such a system are to deliver a uniform flow to the heat exchanger positioned downstream of it, and to have low losses. Two factors called for more research on such a system: Firstly the poor performance of large angle diffusers itself and secondly, the discrepancy between the conditions that diffusers operate in, in literature versus those in industry.

2

Background

As said in Chapter 1, fired heaters can have a thermal efficiency of 92.4 % if a configuration with a radiation section, a convection section and a combustion air preheater is used. In Figure 2.1 an overview of such a fired heater is given. In the fired heater heat is transferred from the flue gas to the process fluid. In the air preheater energy is transferred from air to air; from the flue gas to the combustion air. This heat transfer occurs at relatively low temperature as the flue gas has already passed through the radiation and the convection sections of the fired heater.

The trajectory of the air through the system shown in Figure 2.1 is as follows: Via a centrifugal fan and a (diffuser) transition duct, ambient air enters the cold side of a heat exchanger. Here the air is preheated, in this example with three cross flow passes on the cold side. In the configuration shown, the heat transfer plates would lay in the plane of the image. The preheated air then flows towards the fired heater. Here it is used for the combustion of the fuel. The energy of the flue gas is transferred to the process fluid, via radiation and convection. The flue gas then either leaves via the stack, or it again enters the air preheater, now on the hot side. This depends on the stack damper positioned in between the burner, with which it can be controlled how much of the flue gas is used for the air preheating. In the air preheater the flue gas will preheat the combustion air. Downstream of the preheater there is another fan and finally all gas exits through the stack. As mentioned in Chapter 1, high losses occur in the diffuser transition duct. This work will focus on the fan-diffuser system in the red box of Figure 2.1.

2.1. Problem description

The goal of the above mentioned fan-diffuser system (in the red box of Figure 2.1) is to deliver air to the air preheater, in a way that optimum heat can be transferred. This must be done at minimum power input of the fan. Optimum heat transfer can occur if the low is spread out evenly over the air preheater its inlet. Two other considerations are that a non-uniform flow can lead to non-homogeneous corrosion, and non-homogeneous plugging of the heat exchanger. Both will shorten the lifetime or the maintenance interval of the equipment.

In diffusers the goal is to slow down the flow, with that the pressure should increase. Over the length of the diffuser, kinetic energy is thus converted into pressure energy. High pressure acts as the driving force for the flow through the channels of the air preheater. In practice, diffusers have often been found to not do a good job at this energy conversion process. The problem is flow separation. In Figure 2.2b for two diffusers the flow is shown. In the top diffuser there is no flow separation, in the bottom one there is. The bottom diffuser is also called stalled. If in a diffuser the flow separates from a wall, locally the flow will not slow down. Even though in such a case the average velocity does go down, the kinetic energy of the flow remains high. The result is poor flow distribution and a reduced high pressure at the air preheater inlet. Diffusers are discussed in Section 2.2. The conditions at the diffuser inlet also influence the performance of the system. These are set by the fan. Generally,

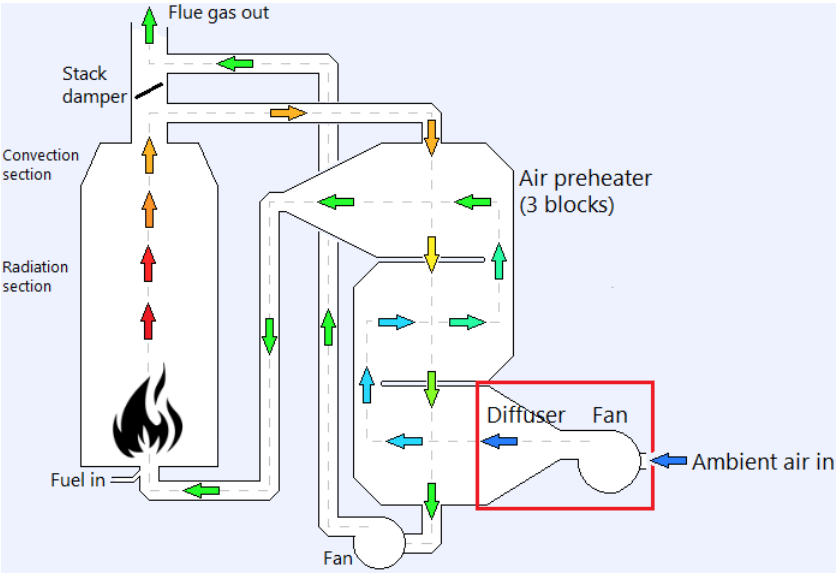

Figure 2.1: 2D drawing of the fired heater configuration with air preheater. The process fluid tubing is not shown.

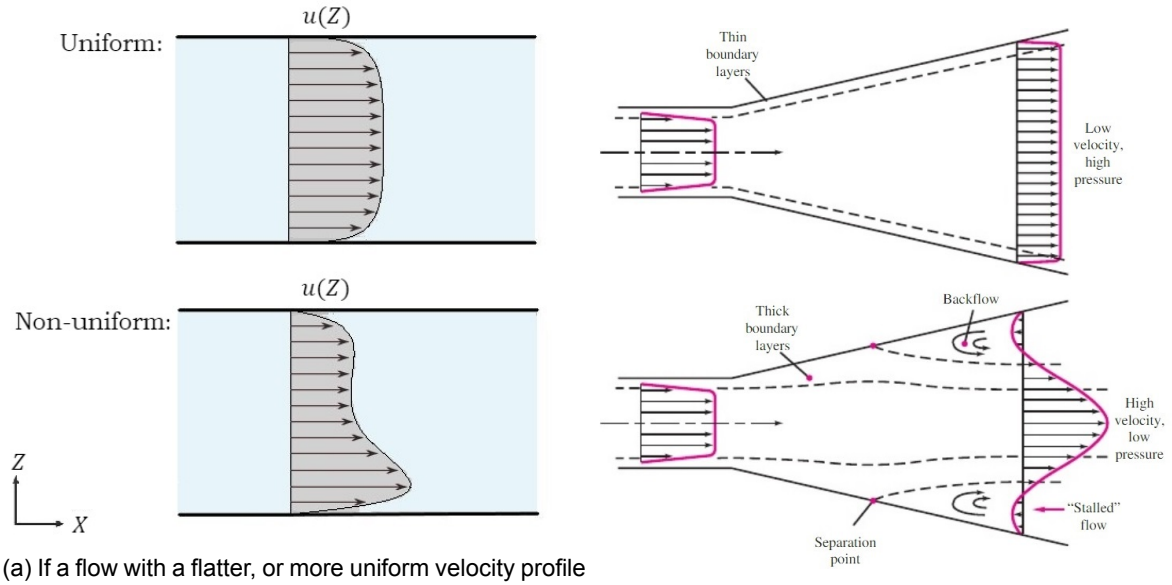

(a) If a flow with a flatter, or more uniform velocity profile such as the top one, enters a heat exchanger, all heat transfer channels will operate in their design conditions (except for the topmost and bottommost few channels). A non-uniform velocity profile will lead to off-design conditions.

(b) The velocity profiles and streamlines of a non-stalled diffuser, and a stalled diffuser. Note that multiple types of stall exist, each with their own velocity field, see Section 2.2. Taken from White (2011).

Figure 2.2

centrifugal fans are used to drive the flow for this application, these are discussed in Section 2.3. To conclude this section, the goal of this research is to improve the flow in a system consisting of a centrifugal fan that blows directly into a large angle diffuser with rectangular cross sections. Sections 2.4 and 2.5 will focus on the method with which to do so. The last section of this chapter will focus on the current state of the art.

2.2. Diffusers

Diffusers are used to slow down a high velocity flow, and with that to recover (increase) pressure. As said, the static pressure recovery depends on the losses in the diffuser, and the

decrease in flow of kinetic energy over the length of the diffuser. A fully flat velocity profile contains minimum kinetic energy for the flow area and mass flow rate. The more non-uniform the velocity profile, the more kinetic energy it will contain. In theory, the velocity profile at the diffuser outlet should thus be as flat as possible to have maximum pressure recovery. In Section 2.1 it was mentioned that also this velocity profile should be flat in order to have maximum performance of the air preheater.

The performance of a diffuser is closely related to the flow pattern. Four characteristic flow patterns can be seen in diffusers: 'No stall', 'transitory stall', 'bistable steady stall' and 'jet flow', see Figure 2.3.

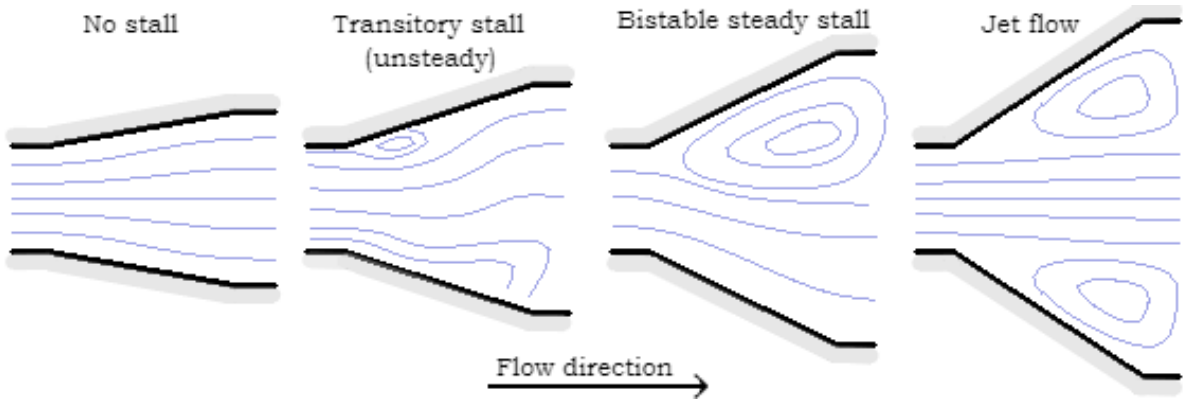

Figure 2.3: Diffuser flow regimes, note that for 'Large transitory stall', the position of the jet varies over time.

2.2.1. Flow regimes

Below the four flow regimes seen in diffuser are described. The below sections apply to a planar (widens in one direction) diffuser with a straight center line, with Reynolds numbers larger than 5×10^4 and Mach numbers lower than 0.2.

No stall: With the flow pattern of 'no stall', there is no (or hardly any) flow separation. The flow slows down with the expanding cross section. The flow at the diffuser outlet is very uniform, and so in theory there is high pressure recovery. This flow pattern however is only observed in diffusers with small divergence angles in which the flow does not slow down to a large extent. Little kinetic energy is thus converted into pressure energy and so they have a low effectiveness. The losses for this flow pattern are low.

Transitory stall: At larger divergence angles, the flow becomes unsteady. Big oscillations characterize this highly unsteady flow. Separation of the boundary layer occurs randomly, albeit in cycles of build-up and wash-out on both the walls alternatively. The position of the separated regions is not fixed, and the size also varies over a wide range. Generally for a planar diffuser, when the boundary layer separates from one wall, the flow will remain attached to the opposing wall. Zambonini (2016) found that the elapsed time between the formation of the separation, its growth and the final break-down of the structure is $100t$, where t is the time necessary for a fluid parcel to pass through the diffuser. This value is larger compared to characteristic times scales of the other regimes where variations are of the order of $10t$. Furthermore, the time necessary for the stall build-up phase is usually considerably longer than that necessary for stall wash-out. For this flow regime the pressure recovery is the highest.

Bistable steady stall / Fully developed two-dimensional stall: Diffusers that again have a larger angle will be in the regime of 'bistable steady stall' or 'fully developed two-dimensional stall' (depending on the source). For a planar diffuser the jet has two stable positions, it can stick to either one of the two diverging walls. The boundary layer separates from the opposing wall, the separation front coincides with the start of the diffuser. The pressure recovery is low. Kibicho and Sayers (2008) found that in this regime for a uniform flow entering the diffuser, it appears random to which wall the jet remains attached. Only some sufficiently large perturbation could reposition the jet. Furthermore they found that the pressure recovery in

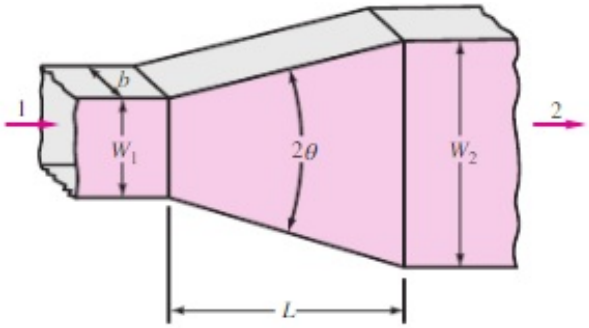

Figure 2.4: Geometric parameters of straight walled diffusers, the image and symbols are as in the work of White (2011).

the diffuser is independent of what wall the jet attaches to.
Jet flow: The worst performance of diffusers is found in the regime of 'jet flow'. The flow that enters the diffuser, detaches from both diverging walls (in a planar diffuser). Two recirculation zones exist, above and below the jet. The pressure recovery and flow distribution are as poor as they can get.
Hysteresis zone: In the graph of Figure 2.5, for some geometries, the diffuser operates in the 'hysteresis zone'. Here, the flow can oscillate between the states of bistable steady stall / fully developed two-dimensional stall, or that of jet flow (Zambonini, 2016).

At high Reynolds numbers, above 5×10^4 according to Blevins (1984), the flow pattern is independent of the Reynolds number. Mostly the flow depends on the geometry of the diffuser, in Figure 2.4 the symbols used to describe the geometry of planar diffusers are shown. In Figure 2.5 the relation between the diffuser geometry and the flow regime is given. Even though the figure might indicate otherwise, diffuser flow is affected by many more parameters. The following parameters have an influence on the flow in a diffuser (White, 2011):

- Geometric parameters, any two out of area ratio A_2/A_1, nondimensional length L/W_1 and double angle ψ. Additionally for flat walled diffusers, the aspect ratio b/W_1.
- Inlet boundary conditions:
  - Reynolds number (at low Reynolds numbers)
  - Turbulence intensity
  - Mach number
  - Boundary layer thickness
  - Swirl
  - Velocity profile
- Superimposed pulsations
- The type of resistance downstream of diffuser

The above list consists of too many parameters to practically take into account for the scope of this work, Section 2.5 gives several parameters with which to analyze the performance of the fan-diffuser system.

2.2.2. Diffuser performance

An important tool that traditionally is used to describe the performance of diffusers is the static pressure recovery coefficient, C_p. It is the ratio of pressure increase to the dynamic pressure at the diffuser throat, see Equation 2.1. In this form, one dimensional flow is assumed. A revised definition will be given in Section 2.5, that will be able to take into

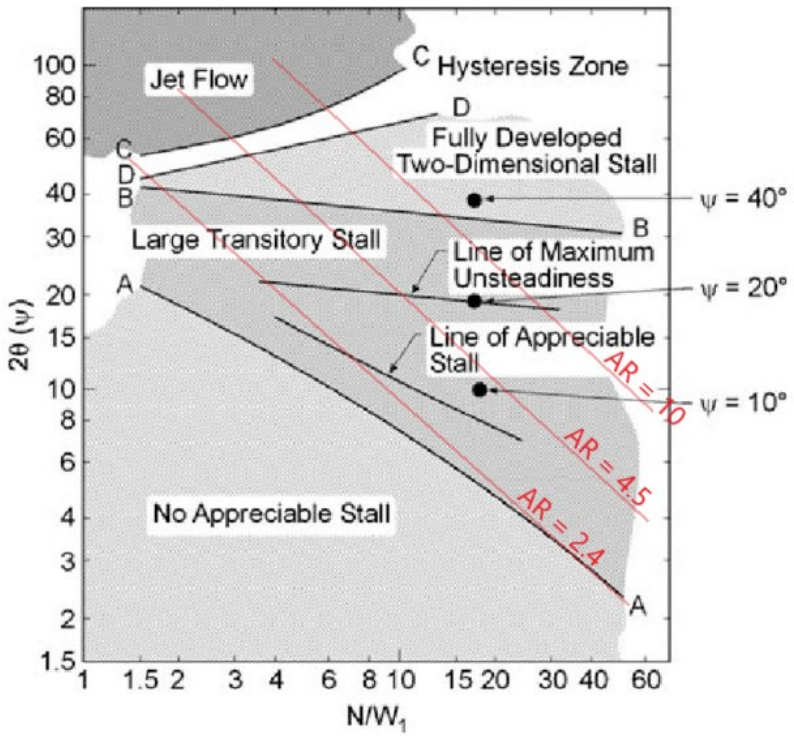

Figure 2.5: Diffuser flow regimes (Kline and Fox, 1958). The axes are such that lines of constant area ratio (AR) are straight lines with a slope of approximately $-45°$, i.e. the red lines.

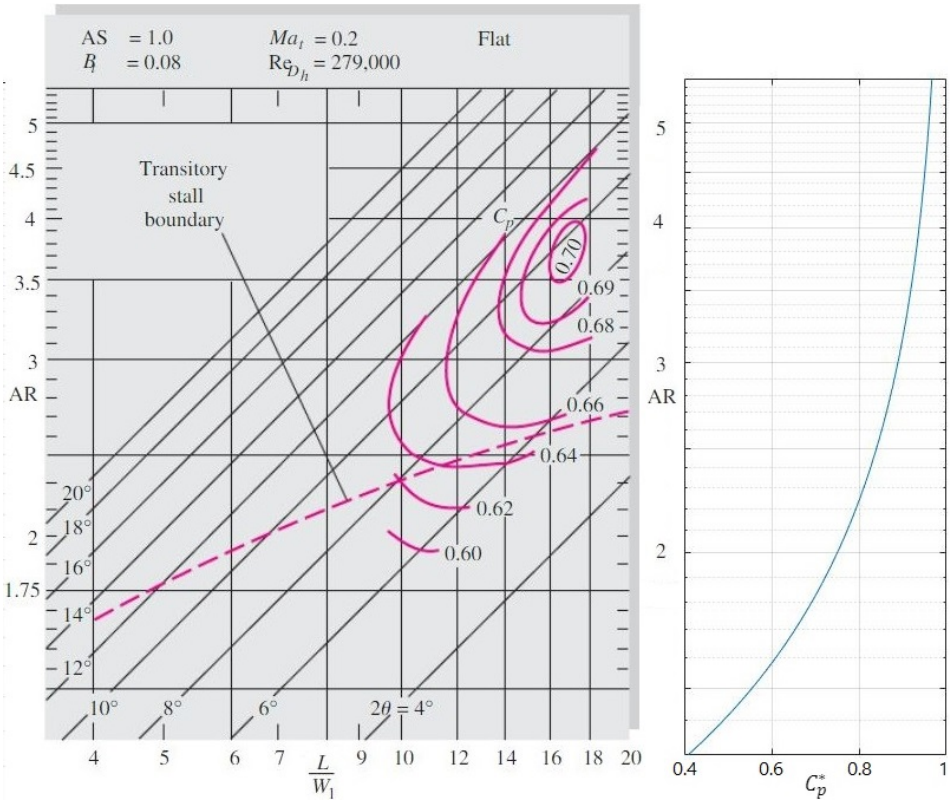

Figure 2.6: On the left; predicted diffuser performance, as a function of the diffuser geometry (White, 2011). Valid for the conditions stated above the graph. On the right there is the ideal pressure recovery coefficient. The graphs are shifted such that the two vertical axes, that both give the area ratio, are aligned. This allows for an easy comparison between the ideal, and the predicted pressure recovery coefficient.

account the non-uniformity of the velocity field, and the pressure. C_p is also called the diffuser effectiveness.

$$C_p = \frac{\Delta p}{\frac{1}{2}\rho \bar{u}_1^2} \tag{2.1}$$

An ideal static pressure recovery coefficient (or ideal effectiveness) is based on the Bernoulli equation. For predictive purposes this C_P^* is of no use, as in real life viscous effects and non-uniformly distributed velocities and pressures come into play. It is based solely on the area ratio of the diffuser, see Equation 2.2.

$$C_p^* = 1 - \left(\frac{A_1}{A_2}\right)^2 \tag{2.2}$$

The ideal effectiveness can be used to define the static pressure recovery efficiency, η. It is simply the ratio of the actual, measured, diffuser effectiveness over the ideal diffuser effectiveness, see Equation 2.6.

Now, having described some elementary tools with which to analyze the performance of diffusers, take a look at Figure 2.6. In the left graph a prediction of the C_p is given, based on the geometric parameters of the diffuser. It must be noted that the graph is very specific, it applies only to diffusers that are geometrically similar that operate in the conditions listed above the graph. It merely acts as an example, and to show the relation between the pressure recovery, and the geometry of the diffuser. On the right side of Figure 2.6, the ideal pressure recovery is plotted. The two graphs are shifted such that the two area ratio axes exactly line up; this makes for an easy comparison between C_p and C_p^* (recall that $\eta = C_p/C_p^*$).

For the geometries shown in the graph, generally a longer diffuser performs better, especially when looking at diffusers of higher area ratios. The figure thus shows that limited floor space has a negative effect on the pressure recovery coefficient, as it will lead to short diffusers.

2.2.3. Pressure recovery vs. flow distribution

In theory a uniform velocity profile at the diffuser outlet, results in optimum pressure recovery. Namely, a uniform velocity profile yields minimum flow of kinetic energy. This allows for the most kinetic energy to have been converted into pressure energy over the length of the diffuser. In practice this is not the case. The best performance is reached in the region near line $A - A$ in Figure 2.5. Maximum pressure recovery occurs for diffusers that lay near the 'line of appreciable stall'. It must thus be noted that diffusers that have high pressure recovery, also come with a rather poorly distributed and highly unsteady flow. The maximum efficiency is reached in the unstalled region.

2.3. Centrifugal fans

The conditions at the diffuser throat largely determine the diffuser performance (Section 2.2.1); they are set by the centrifugal fan, that for the scope of this work is always assumed to be directly upstream of the diffuser. This section will focus on this type of fan.

Centrifugal fans are widely used in industry, mostly in applications were for the brake horsepower, a low flow rate is required, at higher pressure. This is due to the low *specific speed* centrifugal fans have (White, 2011). Also they are durable, cost effective, and have a wide operating range. Backward curved fan blades are generally the preferred choice as opposed to forward curved, their fan characteristics are more stable and they are generally more efficient (Robert Jorgensen, 1982). Forward curved fan blades can be subject to *pump surge*, transient fluctuations in the flow rate delivered. These are however used in application where a high flow rate is required, at low pressure.

Due to their geometry, centrifugal fans have a non-uniform outlet velocity profile. The fluid, that enters the fan axially (along the axis of rotation of the fan blades, or the *eye* of the casing), is then accelerated outwards, radially. It moves through the fan blades and is then redirected in the scroll, such that the fluid flows towards the fan outlet tangentially. Because of this redirecting, most of the flow will be on the outside part of the outer wall. As

(a) A uniform outlet velocity profile. (b) A non-uniform outlet velocity profile.

Figure 2.7: Schematic drawing of a centrifugal fan, and two outlet velocity profiles.

a result in practice the outlet velocity profiles seen are like that of Figure 2.7b, instead of the profile shown in Figure 2.7a (in one dimension). In reality the velocity is not only a function of the height over the outlet area, also over the width the velocity can vary significantly. Furthermore the flow emerging from centrifugal fans can also have secondary flow structures. Often a swirling flow exits a centrifugal fan (Brun and Kurz, 2005), which is a direct cause for head losses.

2.4. Experimental approach

Two approaches exist to gain understanding of diffuser flow. On the one hand there is computational fluid dynamics (CFD), on the other hand there is the approach of experimental fluid dynamics (EFD). Both come with there pros and cons. In Table 2.1 a brief overview is given of these. Two items were decisive in opting for the experimental approach: The flow in large angle diffusers can be highly unsteady and unpredictable, any of small perturbations can have large effects on the flow, this makes it very hard to trust the output of a simulation, it will have to be validated with experimental measurements. Furthermore, to in the first place be able to perform the CFD analysis, the boundary conditions of the system must be known, these were unknown at the time, and would have had to be measured, again, with experimental work. It was clear that firstly experimental work had to be done to understand what happens in large angle diffusers fed by a centrifugal fan.

Table 2.1: Brief overview of the strengths and weaknesses of CFD and EFD.

CFD		**EFD**	
+	−	+	−
Less time consuming Flexible model Instantaneous field	Uncertain on quality of output Boundary conditions required Turbulence closure relations required that are unknown in this category of flows	Measure in real world Easy to understand	Scaling phenomena Needs (scale) model Mean velocity field

2.4.1. Dynamic similarity

One drawback of EFD has to do with scaling. Building a model of a fan-diffuser system is only of use if there is dynamic similarity between the cases of the lab and that in industry. This starts with geometric similarity, which is easily achieved, as the test diffuser has no specific real life twin that dictates a geometry. This means that some generic geometry can be chosen, so that the outcomes of this work will be as widely applicable as possible.

Dynamic similarity with a hypothetical real life twin however, is a lot more difficult to achieve than geometric similarity. Any nondimensional group thought to be relevant, must match the value as seen in practice. Furthermore all boundary conditions in nondimensional

form, must be the same for the lab case and what is found in industry. Sardar (2001) nondimensionalized the Navier Stokes equations for a non-inertial frame of reference, in a study concerning centrifugal fans. It was found that the Reynolds number, the Strouhal number, and the Euler number should match, these are defined as in Equation 2.3. Note that the Euler number is defined just as the static pressure recovery coefficient, C_p (Equation 2.1). For the Strouhal number, the f denotes some characteristic frequency such as the fan speed. For the nondimensionalization, see Appendix A.3.

$$Re = \frac{\rho\,\bar{u}\,D_h}{\mu} \qquad Str = \frac{f\,D_h}{\bar{u}} \qquad Eu = \frac{\Delta p}{\rho\,\bar{u}^2} \tag{2.3}$$

As mentioned before, in industry diffusers can be $15\,m$ in height, and the flow velocities are in the range of $60\,m/s$. Both of these are highly impractical to recreate in the lab; for a $1.5\,m$ hydraulic diameter at the inlet, the Reynolds number would be $Re = 6 \times 10^6$ at room temperature. Now assuming a hydraulic diameter of $0.28\,m$ (which is by no coincidence exactly what the windtunnel built has, see Chapter 3), for matching Reynolds numbers, the flow velocity must be $321.4\,m/s$. Not implying that this velocity was ever going to be reached due to practical considerations; studying the flow at this velocity makes no sense as near the speed of sound, dynamic similarity was always going to be lost, as compressibility effects play a major role near $Mach = 1$. However, literature suggests that for Reynolds numbers well above the transition to turbulence, variations in Reynolds number have little effect on the flow. The exact wording depends on the source, as according to Moore and Kline (1958) above values of a few thousand the flow regime is independent of the Reynolds number, whereas according to Blevins (1984) above 5×10^4 the flow regime ánd performance is independent of the Reynolds number.

To conclude this section, an experimental approach is preferred over the approach of CFD. Some test facility should be built, in which the flow in a fan-diffuser system can be characterized, with the main goal of optimizing the flow in terms of pressure recovery and flow distribution. Of course, in industry many types of diffusers exist. Diffusers of rectangular cross section can already have a large variety of shapes. For this reason it would be ideal to have a test facility that is not limited to one geometry. It was decided that a *testing platform* for diffusers should be build. Here, with relative ease, diffusers of different geometry can be studied. With this, the flow in a diffuser that is intended to be built in industry can be, can be studied firstly at a smaller scale.

2.5. System performance

The performance of a fan-diffuser system will be quantified using four performance parameters. In no particular order these will be discussed in the following paragraphs:

Kinetic energy flux factor at the diffuser outlet

Generally in engineering, it is desirable to express field or volume quantities with a single quantity, for easy understanding and comparing. For describing the non-uniformity of a velocity field, the kinetic energy flux factor (α) is used. It is defined as the flow of kinetic energy of a given velocity profile, divided by that of a flat velocity profile for the same flow rate and flow area. Note that a flat velocity profile contains the minimum amount of kinetic energy, again for given flow rate and flow area (see Section 2.2). Its value cannot be below one, át one, the corresponding flow has a fully flat velocity profile (that does not meet the no slip condition). In Equation 2.4 a definition for α is given. The term $\bar{u}$ denotes the *normal* spatial mean velocity, distinguishing between the normal average and the bulk average (the decision to use the normal average velocity was based on the observation that using the bulk average gave values for the kinetic energy flux factor that were below one).

$$\alpha = \frac{1}{A}\int_A \left(u\,/\,\bar{u}\right)^3 \mathrm{d}A \tag{2.4}$$

The nature of the velocity profile at the diffuser outlet has an effect on both the performance of the diffuser and that of the fan. As explained in Section 2.1 in diffusers kinetic energy

must be converted into pressure energy. In theory to have maximum pressure recovery, there should be minimum flow of kinetic energy at the diffuser exit. On the side of the air preheater: These are designed to cope with a uniform mass flux over their inlet areas. A high α_2 will thus lead to a decrease in performance of the heat exchanger.

For some hypothetical flow fields, the kinetic energy flux factor is given in Figure 2.8, in order to gain an understanding for α. The velocity profile used was $u(Y,Z) = (1-(Y/C)^n) \cdot (1-(Z/C)^n)$, where C is half the chord of the square area, was used. For the exponent n the values of 2, 4, 8 & 12 where used. As the profile becomes flatter, the α goes to one, indicating that for the given flow area and mass flow, a lower flow of kinetic energy is achieved.

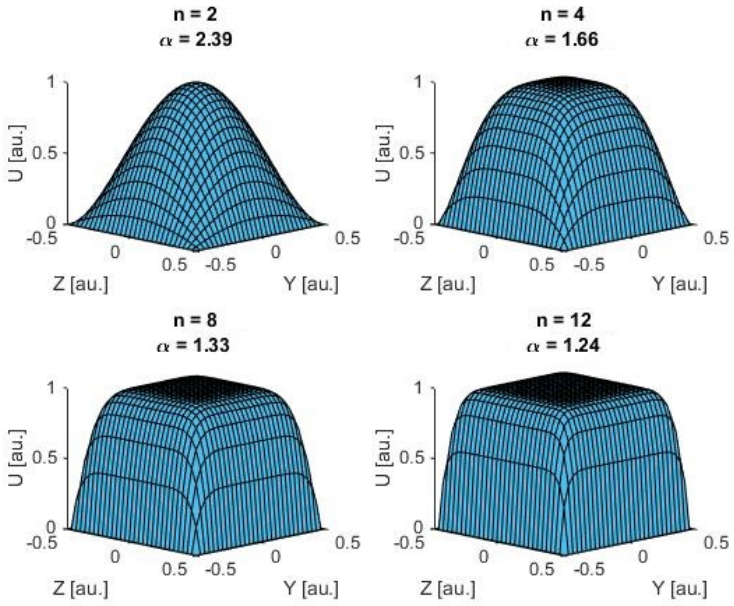

Figure 2.8: The velocity profile $u(Y,Z) = (1-(Y/C)^n)\cdot(1-(Z/C)^n)$, is plotted for four values of the exponent $n = 2, 4, 8 \,\&\, 12$. In the formula, C is half the chord of the square flow area. For all profiles, the kinetic energy flux factor α was predicted analytically.

Static pressure recovery coefficient

Historically, the increase of static pressure over the length of the diffuser, was seen as the most important performance parameter for diffusers. The C_p indicates to what degree the flow of kinetic energy at the diffuser throat is converted into static pressure. It is a measure for how effective a diffuser is.

A definition for C_p was already given with Equation 2.1, this expression however is too simplistic as it is based on scalar values for the velocity and pressure in each cross section. In reality a non-uniform field can exist for the velocity and pressure, due to nonlinear relations between the velocity, pressure and the C_p, the use of these scalar values will lead to errors.

See Equations 2.5a and 2.5b: For the term of the pressure rise, the difference is taken between the mass flow weighted mean pressure[1] at diffuser throat and diffuser outlet. The kinetic energy flux factor will be used to correct for the non-uniformity of the velocity field. Note that $\bar{u}_1$ represents the normal average velocity in the diffuser throat ($\bar{u}_1 = Q/A_1$). The kinetic energy flux factor is as defined in Equation 2.4. Note that the denominator in Equation 2.5b is exactly the same as the mass flow rate weighted average dynamic pressure, see Equation 2.5c. Here, both terms give the mass flow rate weighted average flow of kinetic energy. For sake of simplicity it was chosen to use the definition of C_p without the area integral

[1] In the formula it appears as the volume flow rate weighted average, which is equivalent as the flow is (assumed to be) incompressible.

(which still exists in the definition for α).

$$\Delta p = \frac{1}{Q}\Big(\int_{A_2} pu\,\mathrm{d}A - \int_{A_1} pu\,\mathrm{d}A\Big) \tag{2.5a}$$

$$C_p = \frac{\Delta p}{\frac{1}{2}\rho \bar{u}_1^2 \cdot \alpha_1} \tag{2.5b}$$

$$\frac{1}{Q}\int_{A_1} \frac{1}{2}\rho u^3\,\mathrm{d}A = \frac{1}{2}\rho \bar{u}_1^2 \cdot \alpha_1 \tag{2.5c}$$

It is important to know that in this work a slightly different definition for C_p is used, than in literature. This renewed definition better copes with the non-uniform flow.

Static pressure recovery efficiency

Complementary to the effectiveness C_p, an efficiency is used as performance parameter. Normalizing the static pressure recovery coefficient with its ideal value, gives what is called the static pressure recovery efficiency, defined as in Equation 2.6, also see Equation 2.2.

$$\eta = C_p / C_p^* \tag{2.6}$$

Dissipation in diffuser

For the time rate of energy dissipation in the diffuser, $\dot{W}_{viscous}[W]$, the equations of 2.7 were used. These are a direct result of conservation of energy, their derivation is given Appendix A.1. For these equations it was assumed that the system is adiabatic.

$$\Delta \dot{E}_{kin} = \int_{A_1} \frac{1}{2}\rho u\big(u^2 + v^2 + w^2\big)\,\mathrm{d}A - \int_{A_2} \frac{1}{2}\rho u\big(u^2 + v^2 + w^2\big)\,\mathrm{d}A \tag{2.7a}$$

$$\dot{W}_{pressure} = \int_{A_1} pu\,\mathrm{d}A - \int_{A_2} pu\,\mathrm{d}A \tag{2.7b}$$

$$\dot{W}_{dissipation} = \Delta \dot{E}_{kin} + \dot{W}_{pressure} \tag{2.7c}$$

2.6. State of the art

Below an overview is given of the methods to control the flow in large angle diffusers. All methods aim to prevent boundary layer separation.

- Long guiding vanes (Figure 2.9b): Effectively, a large angle diffuser can be split into several diffusers of more favorable geometry, if over (almost) its whole lengths partitions are used. One large angle diffuser will then consist out of several diffusers. All these *subdiffusers* will have the same area ratio as the original diffuser (if all the guiding vanes are placed concentrically), however they'll be more elongated / have a smaller angle. Looking at the diffuser performance diagrams, Figures 2.5 and the right graph of 2.6, this splitting up of diffusers would be equivalent to moving down or diagonally towards the bottom right, respectively. In the system obtained after splitting up a single diffuser, wall frictional losses will become more prevalent. Furthermore, no mixing can occur between the flow in the several channels. For this reason care must be taken that a sufficiently uniform velocity profile enters the subdivided duct, or -if good knowledge of the flow is present- that all the inlets and outlets of the subdiffusers are placed such that a more constant mass flux is obtained at the outlet, by varying the area ratio from channel to channel. It can be chosen to only split up the channel, over a part of the length of the original diffuser. This would reduce frictional losses, and to allow the streams of the subdiffusers to mix. Most likely it is best to have the subdiffusers in the upstream part of the diffuser.

- Short guiding vanes (Figure 2.9c): With these the goal is to steer the flow, in order to prevent separation and to spread over the full opening angle of the diffuser. They can be placed at or just downstream of the diffuser throat. They must be designed such that the flow remains attached to the vanes. Good knowledge of the inlet conditions must be present, in order to properly design such vanes in terms of the angle of attack, profile and placement. Either straight or curved airfoils can be used to control the flow in this manner. Just downstream of the vanes, the flow will not at all be uniform, several jets are likely to exist at that cross section. If the resistance inherent to the downstream process equipment is adequate, these will vanish without any extra flow control, this would be ideal. However it is possible that these jets will persevere right until the diffuser outlet. If so, a perforated plate could be used to even out the flow up to smaller scale (at high cost in terms of pressure drop).
- Perforated plates (Figure 2.9d): Out of all mentioned, this method to control the flow in large angle diffusers was studied the most. Here the work of Sahin and Ward-Smith (1987) and that of Noui-Mehidi et al. (2005) will be summarized, it must be noted that the studies were focused on respectively the pyramidal (rectangular to rectangular, widening in two directions, with two planes of symmetry) and the asymmetric (rectangular to rectangular, widening in two directions) type of straight walled diffuser, instead of the two-dimensional type. Sahin & Ward-Smith tested three types of perforated plates, having porosities of 0.4, 0.5 and 0.58. It was found that for the pyramidal type of diffuser optimum results are obtained with two perforated plates of porosity $\beta = 0.5$, placed just downstream of the throat, and just upstream of the diffuser outlet. With a plate porosity of 0.4 the flow accumulated near the diffuser walls due to a too high resistance, with an increased porosity of 0.58 insufficient spreading action was observed. In the work of Noui-Mehidi et al. it was found that for a specific asymmetric large-angle diffuser three plates with $\beta = 0.45$ placed just downstream of the throat, approximately half-way the diffuser and just upstream of the diffuser outlet, resulted in the best flow uniformity. Furthermore they stated that the performance of a diffuser with perforated plates was very sensitive to their configuration and porosity. Secondly, with perforated plates, it is possible to vary the porosity over the cross section of the diffuser and with that, more effectively spread the flow than with plates of constant porosity. At any region of above average velocity, a less porous plate can be inserted in order to divert flow to other regions, and vice versa. No literature was found describing this second method of using various porosity media. Perforated plates can be effective, however a high price is paid as a large pressure drop over the plate can be expected.
- Wire gauzes (Gibbings, 1973): Gibbings studied a circular to square diffuser (of an angle equal to that of the test diffuser built, however larger area ratio). He found that inserting a pyramid of wire gauzes, with its apex pointed in the upstream direction and an opening along the channel walls, gave an acceptable degree of flow uniformity at the outlet, an acceptable total pressure loss and an acceptable degree of flow steadiness. Planar wire gauzes can as well be used, similar to how perforated plates have been described.
- Vortex generators: These are rather common in preventing flow separation, in applications where the flow is bounded by a laminar boundary layer. By triggering a transition to turbulence, these devices are quite effective (Logdberg, 2006). However for the present study, the oncoming flow is turbulent and furthermore vortex generators are only effective for small adverse pressure gradients, such as those at airplane wings. For turbulent flow in large angle diffusers they unlikely to be effective.

2.7. Chapter conclusion

Fan-diffuser systems, especially those with a large angle diffusers, have been found to perform poorly. This calls for more research on fan-diffuser systems. Another factor is that in previous work, the diffusers were subject to uniform inlet conditions. This makes it difficult to predict the performance of diffusers in industry, as these are usually not subject to uniform inlet conditions.

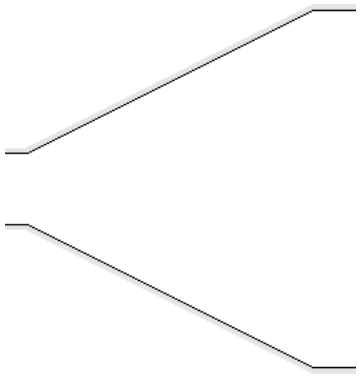

(a) Empty diffuser, flow is from left to right.

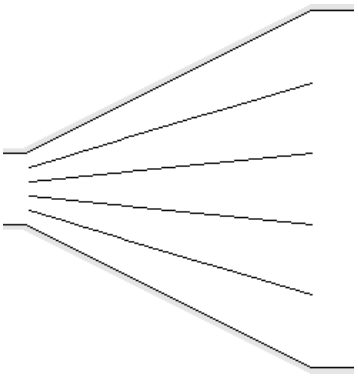

(b) Diffuser with long guiding vanes (subdiffusers).

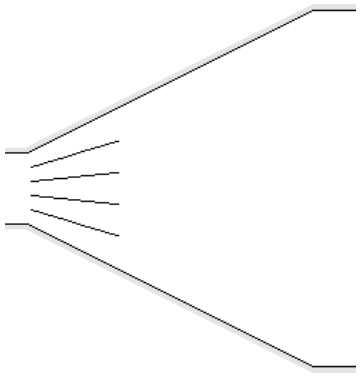

(c) Diffuser with short guiding vanes, these allow for mixing of the streams that firstly are separated and so, potientially a better distribution of the flow.

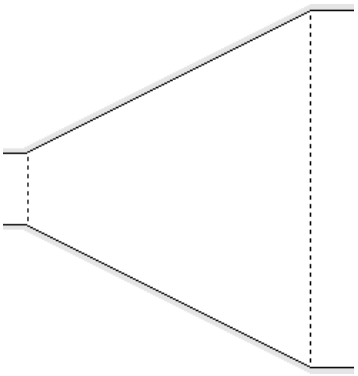

(d) Diffuser with perforated plates, or any other type of porous medium that offers resistance to flow.

Figure 2.9: A schematic representation of the three most common methods for optimizing the flow in diffusers (flow is from left to right).

A test facility was built in order to do research on fan-diffuser systems, as for the current problem a computational approach cannot be trusted without any validation, see Section 2.4.1.

It was designed such that without too much effort, diffusers of various geometries can be tested. The design of this testing platform will be described in the next chapter. With this platform the flow in fan-diffuser systems can be studied before the system is built at industry scale. The performance of the system can be quantified using the four performance parameters described in Section 2.2.2, namely the static pressure recovery coefficient, the static pressure recovery efficiency, the kinetic energy flux factor at the diffuser outlet and the time rate of energy dissipation in the diffuser. Besides these it is important to have knowledge of the flow in general, i.e. the velocity field must be known at relevant positions. In the diffuser throat it is most important to have knowledge of the velocity field, all three velocity components should be known there in order to perform an optimization of the flow. Also at the diffuser outlet it is important to have knowledge of velocity field.

Once a diffuser has been characterized, an optimization could start. The methods described in Section 2.6 can be used for this. After modifying the diffuser, again pressure & velocity measurements can then be performed in order to see the effect of the modification. This process of optimizing the flow in a fan-diffuser system will be beyond the scope of this work.

3

Experimental set-up

A test facility was built in the fluid mechanics lab at Apex Group, in order to gain knowledge on flow through large angle diffusers. In order to asses the performance, it was required to measure velocities and pressures. Flow velocities need to be measured with laser optical instruments, and so specific sections had to be transparent. Furthermore, the laser optical methods imposed that the system would be a closed loop, as the expected flow rate could not practically be filled with enough and homogeneously spread out seeding particles. In this chapter the experimental set-up will be described.

3.1. Centrifugal fan

The fan used to drive the flow was of the type 'MBRC 40/12 M4 $0,75kW$' produced by the manufacturer Casals. It is a vaneless, single inlet centrifugal fan with backwardly curved blades. It has good geometric similarity with fans seen in industry for the application of driving the flow through an air preheater. In Figure 3.3 the fan curve is shown, the pressures plotted were taken from the manufacturers website (Casals Ventilation, 2018). The hydraulic power plotted was derived via multiplying the flow rate and the total pressure. The point of maximum power can clearly be seen, it lays at $1.13\,m^3/s$ & $411\,W$. The fan blades rotate at $1400\,RPM$, the engine is a single phase 4-pole induction motor.

3.2. Design of the windtunnel

In this section it will be elaborated on how the design of the windtunnel came about, the materials and joining methods will also be explained. Figure 3.5 gives a top view of the system built. The parts denoted with 'Diffuser', 'APH model' (air preheat model) and the numbered parts, are all the separate modules. These are connected to each other such that the system is air tight. The use of separate modules allows for easy modifying of the system, and for recycling of certain parts in future studies. With relative ease, the diffuser section can be replaced in order to study a diffuser of another geometry.

3.2.1. Shape of diffuser

After the decision was made on what fan to use, the overall shape of the measurement section had to be set. Basic geometric parameters had to be set, namely the area ratio, length and width. Firstly however it was decided that the diffuser would be symmetric, that it widens only in one direction, and that it would have no corner in it. In industry this is often not the case, however for the scope of this work it is desirable to have a geometry that is as generic as possible.

The area ratio would be $A_2/A_1 = 5$, the nondimensional length was set at $L/W_1 = 4$. This gives a diffuser double angle of 53.1°. The height and width (W_1(!) and b_1 respectively) of the fan outlet were 322 and $254\,mm$, with these the exact shape and size of the diffuser was set, see Table 3.1. With these sizes, the windtunnel is more or less as large as it can be, any

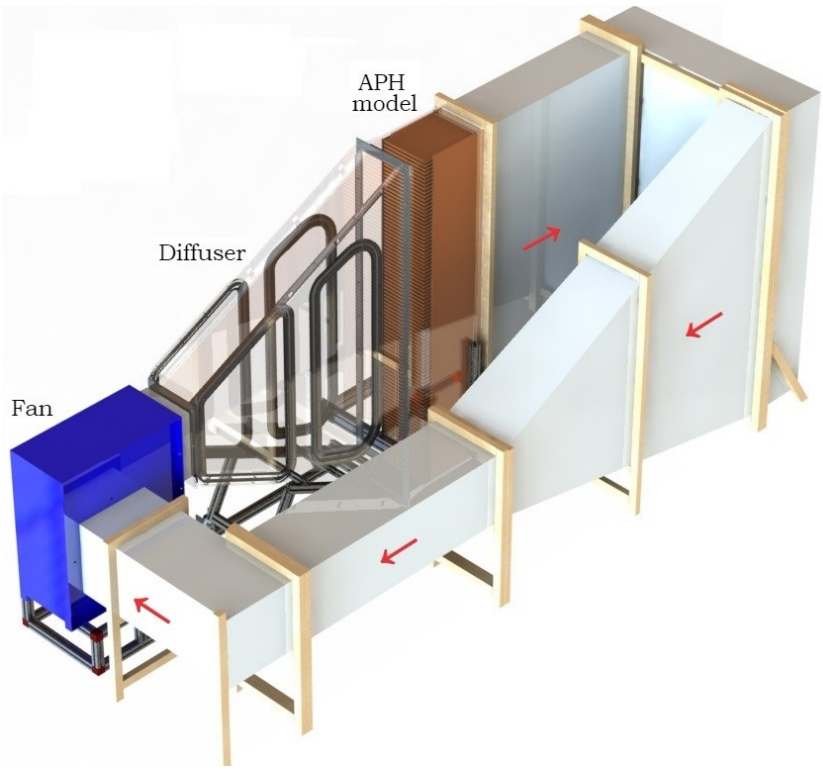

Figure 3.1: Impression of the windtunnel built. The red arrows indicate the direction of the flow.

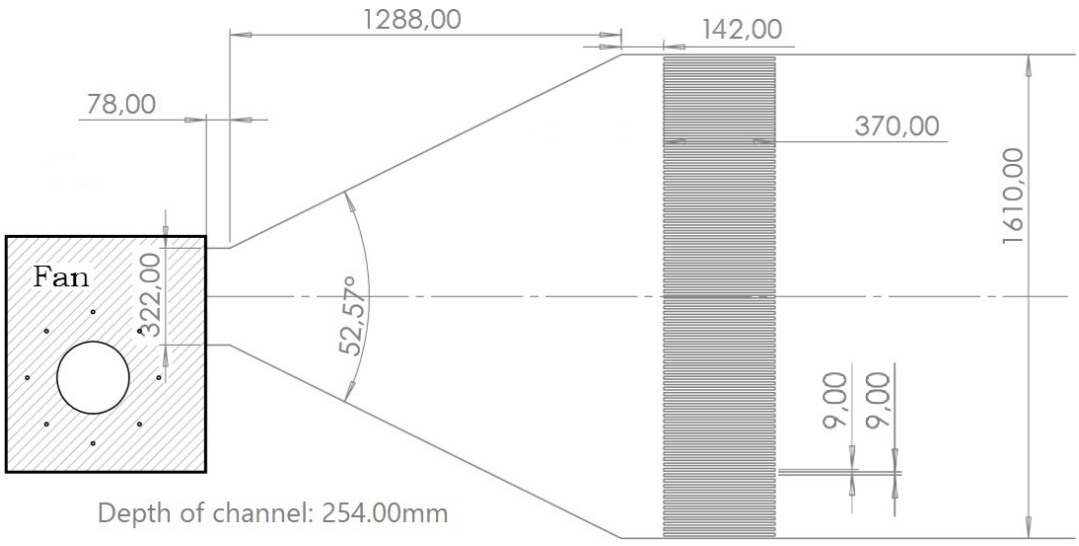

Figure 3.2: Relevant dimensions of the fan, diffuser and the air preheater model.

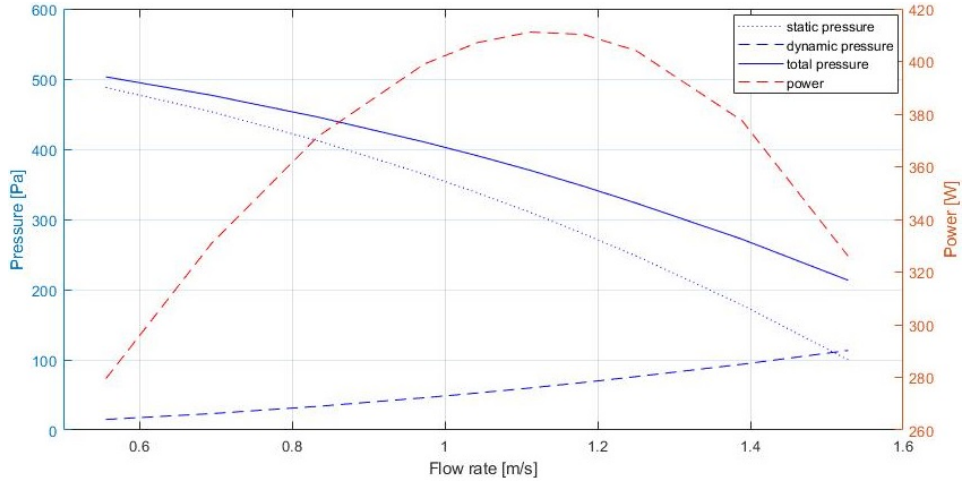

Figure 3.3: Fan curve of fan used, as presented by the manufacturer Casals Ventilation (2018).

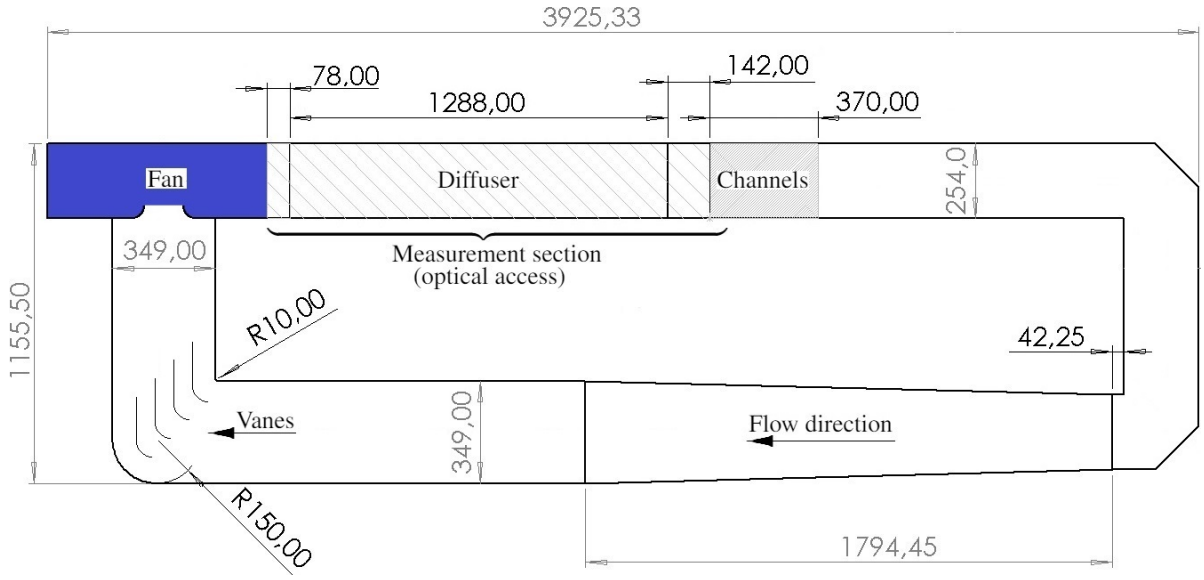

Figure 3.4: Top view from the test facility, with the internal dimensions of the duct.

larger and practical considerations such as ceiling height, and maximum size of the perspex that can be laser cut would become limiting. This is desirable as the larger the windtunnel, the more dynamically similar it becomes with the systems seen in industry.

Expected diffuser performance

With the area ratio and the length being $A_2/A_1 = 5$ and $L/H_1 = 4$, the performance and flow regime can be predicted. According to Figure 2.5, the diffuser will operate in the bistable steady stall regime. Regarding the pressure recovery coefficient, as said in Chapter 2, diffuser performance maps are specific to the conditions set during measuring (these maps are based on empirical work). No graph was found that describes a diffuser with similar conditions, and so no useful prediction for the C_p can be given. A rough estimate can be given however. Blevins (1984) gave a prediction of $C_p \approx 0.35$. This number applies to a diffuser with free discharge, a uniform flow at the inlet, and a boundary layer of $2\delta_1/W_1 = 0.015$. White (2011) gave no C_p for the current geometry, see Figure 2.6. The ideal pressure recovery is $C_p^* = 0.96$, from Equation 2.2.

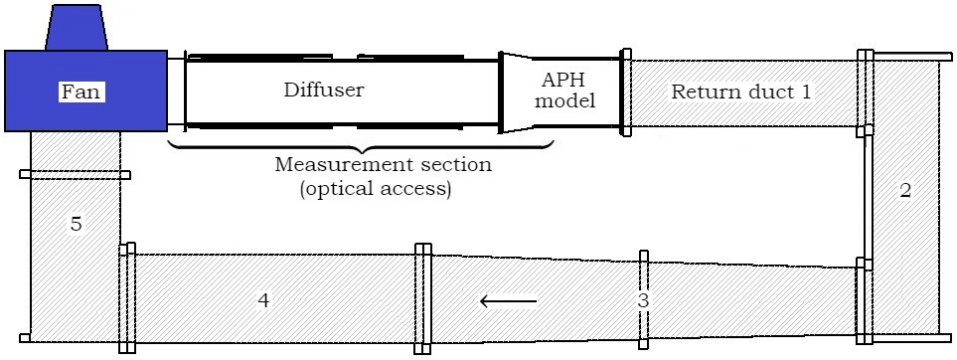

Figure 3.5: Top view of the test facility built. Apart from the fan, it consists of seven modules. A short straight section downstream of the fan, the diffuser and the first part of the air preheater model have optical access. The remaining modules of the return duct are made out of wood.

$W_1 = 322\,mm$
$W_2 = 1610\,mm$
$b = 254\,mm$
$L = 1288\,mm$
$\psi = 2\,\theta = 53.1°$

Table 3.1: Relevant dimensions of the diffuser in the measurement section.

3.2.2. Measurement section

As said before, the measurement section of the windtunnel had to provide access for the laser optical flow measurement technigues, and so these two specific modules were made out of transparent perspex. Sheets of $8\,mm$ thickness were used as these were a good compromise between stiffness and costs. They were laser cut and glued together using acrylic glue (Acrifix $1S0117$): A needle was used to place a small amount of glue at an exposed edge of the interface between two perspex parts. As the two were firmly pressed together, capillary forces would drive the fluid such that the whole interface is covered in glue.

To have physical access, 4 doors were present in the measurement section. This was required for easily mounting inserts needed for optimization, and to clean the inside of the channel. After some time during laser optical measurements, the seeding particles would settle on the walls, this limited optical access and thus interferred with the measurements. In order minimise their influence on the measurement, the doors were designed such that they lay flush with the rest of the inner surface. Only a small gap would exist on the inside of the channel, this gap has the width of the laser used for the cutting process, in the range of 0.1 to $0.3\,mm$.

It is shown how the door design allows it to lay flush on the inside of the channel, see Figure 3.6. The door (shaded green) is bolted on to the channel wall (shaded blue) with M5 bolts. These grip into threaded perspex parts glued onto the main channel wall, with a design such that a groove is between that houses a seal that goes around the perimeters of the door. The seal is compressed when the door is properly mounted, decreasing chance at leakage. At all points, these bolts are used side by side, with the goal of eliminating an unwanted moment acting on the channel wall and door (especially the glued connections in the assembly of the door). A large amount of bolts was used for this, to spread the load required for compressing the seal. Furthermore, to minimise chances at damaging the perspex, nylon bolts were used in conjunction with large diameter washers.

3.2.3. Resistance

For the current work, the diffusers are always assumed to be followed by a plate type heat exchanger. The related resistance to flow must be simulated in the windtunnel as it will influence the flow.

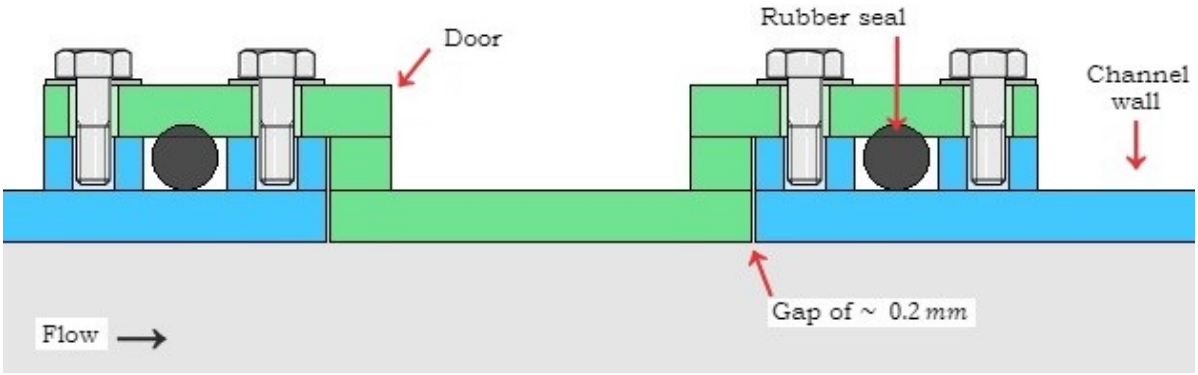

Figure 3.6: The inside of the channel is down below. The door (green), is bolted on to the channel wall (blue), in this process a seal (dark grey) is compressed, sealing the inner channel from the surroundings (this seal runs along the perimeter of the door). All the blue and green parts are of $8\,mm$ thick perspex (glued onto each other for the parts of same coloring), the seal is a $10 \times 10\,mm^2$ foam rubber strip, with adhesive on one of its side, used to fasten it to the channel wall.

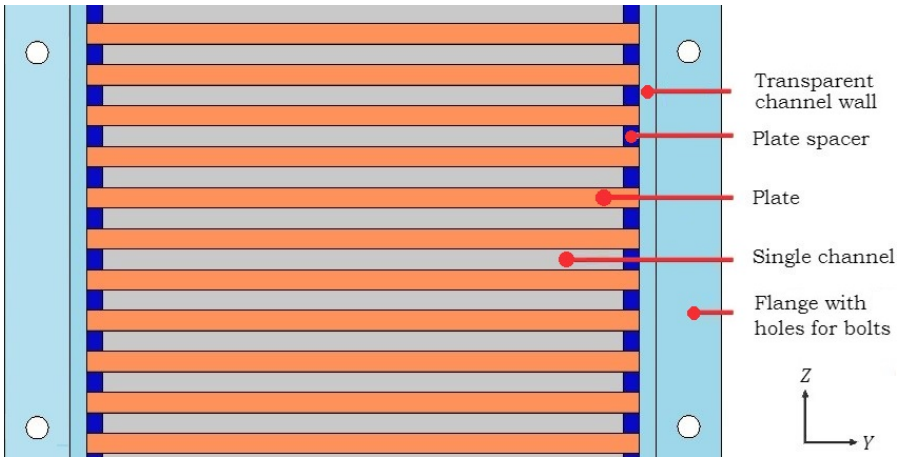

Figure 3.7: Schematic drawing of the plate stack, looking at it in the streamwise direction (along the X-axis). The flow would be *into* the paper.

Horizontal plates of $9\,mm$ thickness were stacked on top of each other, spaced by $9\,mm$[1]. The spacers in between the plates were simple wooden strips, nailed to the plates on the left and right side. The channel was designed such that these spacers would not create a forward or backward facing step at their upstream or downstream sides. This is achieved by locally having a slightly wider duct, the extra width exactly houses the spacers, see Figures 3.7 and 3.8; the horizontal distance in between the spacers is $254\,mm$, exactly the width of the channel up- and downstream of the plates. In the later of the two drawings, it can be seen how the plate extends somewhat ($50\,mm$) into the upstream direction, with this optical access is gained for the first few centimeters of the channels, allowing for LDA measurements to be performed inside the channels. This is a vital measurement, as only measuring inside the channels will give a reliable picture of how the mass flow is distributed over the height of the plate stack.

3.2.4. Return duct

In order to perform the desired laser optical velocity measurements, adequate seeding must be present in the flow. With the equipment at hand only a limited flowrate can be foreseen with enough seeding particles. It was expected that the seeding generator could not supply an adequate rate of seeding, for this reason it was necessary to recycle the air (with the seeding particles) that passes through the system. Once it was decided that a closed system would be built, some other requirements came up. It had to have a pressure drop that was not

[1]Note that in the configuration of Figures 1.1 and 2.1, the plates would be in the vertical plane.

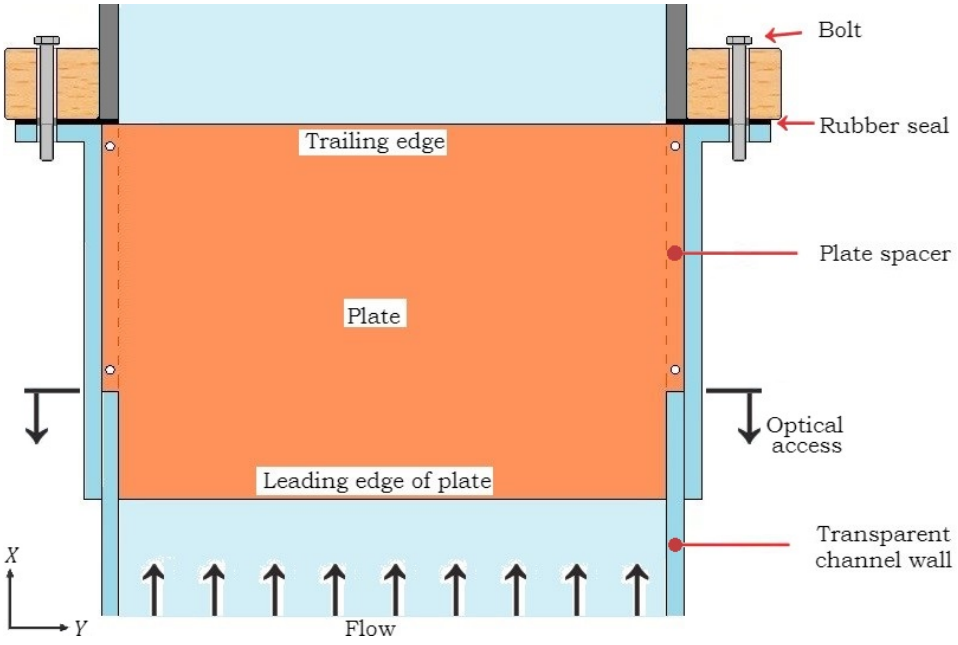

Figure 3.8: Schematic drawing of the plate stack, looking at it from top. Flow is from bottom to top.

too high, it had to be cost effective and most importantly it should not influence the flow in the measurement section. This meant that firstly, a non-swirling flow should enter the fan, as the performance of centrifugal fans is influenced by the conditions at their inlets (Robert Jorgensen, 1982). Secondly, a $1\,m$ straight section was downstream of the heat exchanger model, such that the corner in the duct, would not influence the flow field in the measurement section.

Return duct module 1

For the above reason, it was decided that downstream of the plate stack, adequate length of straight duct was required. This first module would be a straight duct, with the same cross section as the diffuser outlet and heat exchanger geometry model (with the plates).

Return duct module 2

In this duct, the first two 90° turns are present. Here the cross section is still large ($1.61 \times 0.254\,m^2$) and so the velocities are low. For this reason the design of these corners is not critical. Nevertheless, the outside of both corners was bevelled, as can be seen in Figure 3.4.

Return duct module 3

Over the length of this module, the cross section was reduced from $1.61 \times 0.254\,m^2$ to $0.349 \times 0.349\,m^2$. As a result this was quite a complicated module to build by hand, as all of the walls are angled. Adding to this, it is also a large part.

Return duct module 4

In this simple straight duct, the seeding particles were inserted into the flow for the laser optical measurements. This module also housed the thermocouple used to monitor the temperature in the system (see Section 5.2).

Return duct module 5

In order to fit onto the fan inlet, the inner dimensions of the duct leading up to the fan, had to be $0.349 \times 0.349\,m^2$. This dimension defined the dimensions of the ducts in between the nozzle (return duct module D) and the fan inlet.

This last module gave house to the last 90° corner. For two reasons its design is more critical than that of the previous corners. Firstly, due to its smaller cross section, the average

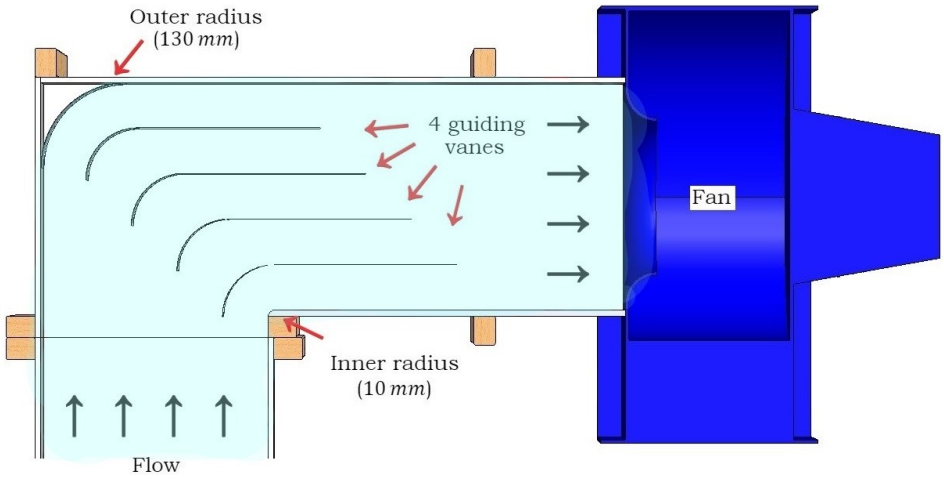

Figure 3.9: Schematic representation of the $5th$ module in the return duct, note the four guiding vanes to straighten the flow before it enters the centrifugal fan.

velocity will be higher than in the previous two corners. For a given *local loss coefficient* the losses will thus be higher. Secondly, the velocity profile emerging from the corner will enter the fan and so specific care must be taken to straighten the flow.

As to optimise this module, a rounded inner edge, 4 guiding vanes, and a rounded outer edge were used, see Figure 3.9. The rounded inner edge had a radius of $10\,mm$, the outer edge had a radius of $130\,mm$. The four guiding vanes were aluminum sheets bent into shape. All vanes had a round initial section (90° with a radius of $80\,mm$) and a straight tail in order to have a straightening effect. Literature suggested that in order to have a straightening effect, the tail of the guiding vanes had to be at least four times the distance in between them (Idelchik, 1986). With four guiding vanes and an overall channel width of $349\,mm$, the tails had to be of length $280\,mm$.

Sealing of the separate modules

In order to prevent leakage, seals were used in between the separate modules. Foam rubber strips ($35 \times 8\,mm^2$) were used, these had adhesive on one of the long sides which was used to fasten the rubber to either the perspex or wooden flanges. Bolts going through holes in the flanges and the rubber strip, would compress the rubber and seal the system. See Figure 3.10.

3.2.5. Pressure drop

Before the windtunnel was built, an effort was made to make the corresponding system resistance curve; its pressure drop as function of the volume flow rate. With it, a gross estimate of its actual flow rate was done. For all points along the windtunnel where a substantial pressure drop was expected, the local pressure drop was predicted via the method of *local loss coefficient*. In Table 3.2 the local loss coefficients (K) are shown, all were found in the work of Idelchik (1986). With these, the static pressure drop was calculated. Also, using the areas of the fan inlet and outlet, the difference over the fan, in dynamic pressure as function of the flow rate was found, using the simple one dimensional approach of $p_{dyn} = \frac{1}{2}\rho\bar{u}^2$ where $\bar{u} = Q/A$. Subsequently the system resistance curve together with the fan curve were plotted, see Figure 3.11. Their intersection lies at $Q = 1.34\,m^3/s$, which is the expected volume flow rate of the windtunnel. (Now with hindsight, the volume rate turned out to be $Q = 1.14\,m^s/s$, see Section 5.3.)

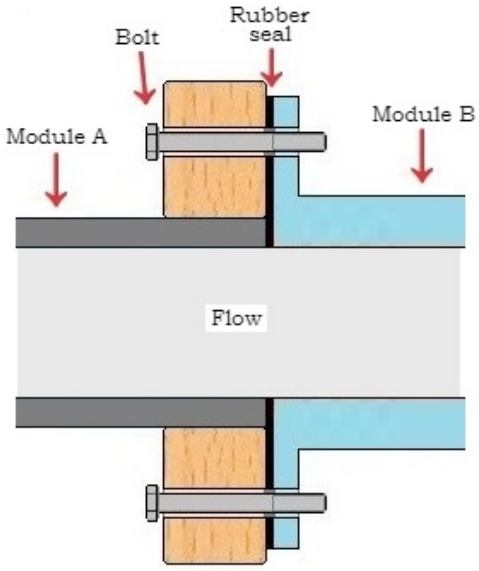

Figure 3.10: Separate modules (here; modules A & B) were connected with $M6$ bolts. Once these were fastened, rubber seals would be compressed such that an air tight connection is maintained.

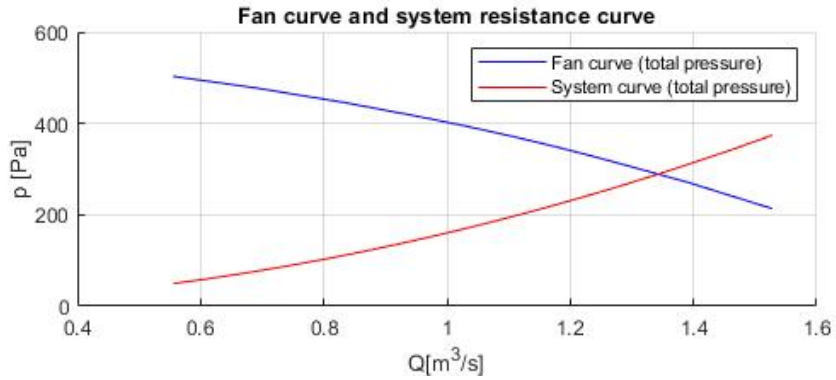

Figure 3.11: The fan curve and system resistance curve, total (stagnation) pressures are plotted. Their intersection lies at $Q = 1.34\, m^3/s$.

Position:	Diffuser	Plate stack	$1st$ turn	$2nd$ turn	Nozzle	$3rd$ turn	Fan inlet
K**:**	0.82	5.59	0.85	0.85	0.04	0.22	0.03

Table 3.2: Local loss coefficients (K) at all the relevant positions along the windtunnel. Third turn has considerably lower loss factor due to guiding vanes in it. Frictional losses in the straight sections are not taken into account.

4

Measurement equipment & post processing

In this chapter the measurement equipment will be described, as well as all relevant steps in the post processing of the data.

4.1. Flow visualization

For visualization of the measurement results, Matlab and Paraview were used. Furthermore a *real life* visualization was performed, to qualitatively observe the macroscopic flow structures. Flexible plastic strips were attached to the inner wall of the transparent section, with which locally the direction of the flow was shown.

4.2. Pressure

For measuring the pressure distribution throughout the windtunnel, either the pressure in the bulk of the flow, or that at the wall could be measured. It was decided that only wall pressure measurements were to be performed. The reason being that for measuring pressures in the bulk, a Pitot tube would have to be used. These have to be aligned with the flow at each position, which is very hard to accomplish in this flow. Using a Pitot tube was thus not worth the effort when considering that also many holes would have to be drilled into the channel walls.

Over a single cross-section the pressure was assumed to be near constant and so it is acceptable to limit to wall pressure measurements. With hindsight, this statement holds for all positions downstream of the air preheater model, not for cross-sections at the diffuser throat and outlet. At these positions however, respectively 24 and 28 wall pressures measurements were taken, spread out along the perimeter (Section 5.4), and so still rather good insight of the physics was gained.

4.2.1. Tool for wall pressure measurements

As in total at 63 different locations (see Section 5.4) a pressure measurement was performed, it was important to have a method that allows for easy, quick and consistent measuring. The wall pressures were recorded with a needle in conjunction with an electronic manometer controlled via a computer. The manometer was of the type *'Testo 435-4'*, the software used was the *'Testo comfort software'*. Holes of diameter $1\,mm$ were drilled, to make an entrance for the $0.8\,mm$ needle. When not in use these holes were closed with a piece of tape. For the measurement it is important that the tip of the needle lays flush with the inner surface of the wall. A tool was made that allowed for easy positioning of the needle. See Figures 4.1, 4.2a & 4.2b; the tool comprises of two pieces of perspex glued to one another. The upper one has a hole (with a conical top part to have a larger surface for glueing) slightly larger than the needle itself, the lower one has a larger hole, which houses part of the needle and

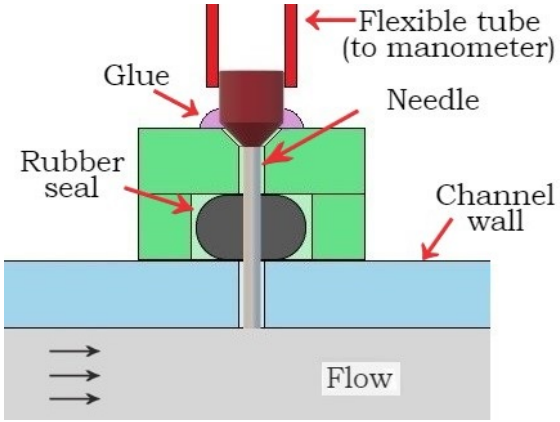

Figure 4.1: Schematic drawing of tool made for recording the wall pressures through out the system.

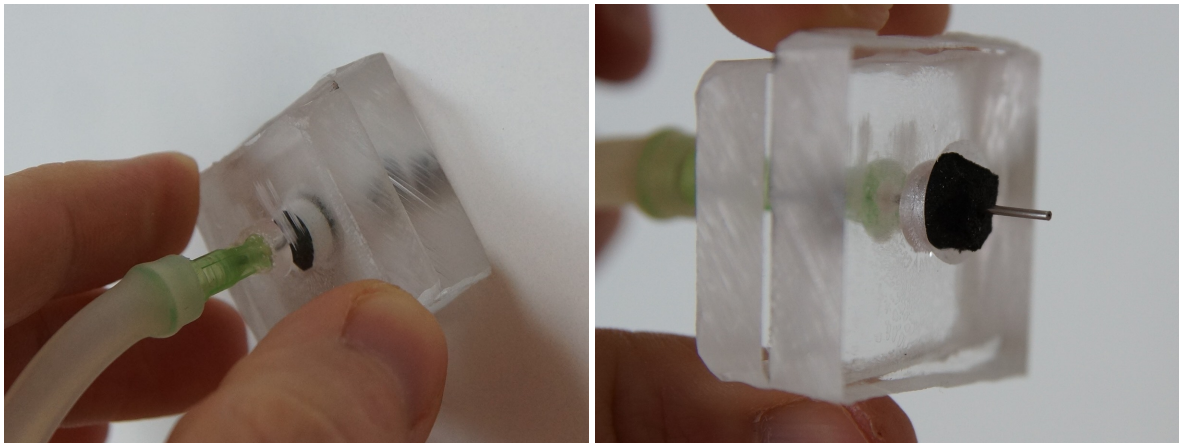

(a) (b)

Figure 4.2: The tool made for easily measuring the wall pressures. The tool is pressed against the outside of the channel (left), then the end of the needle is in line with the inner surface of the wall, the rubber seal will then prevent leakage.

a rubber seal. If the tool is pressed against the outer wall, no leakage occurs as the rubber seal is compressed and the tip of the needle is positioned in-line with the surface. In Figure 4.3 it shown how for several positions the pressure varies over time. Note that the pressure remains quite constant over time.

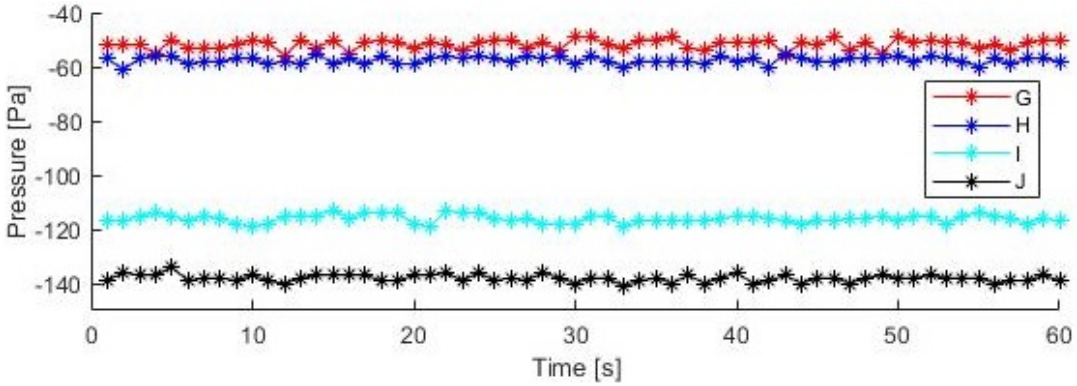

Figure 4.3: Plotted is how the wall pressure was measured at four points along the axis of the windtunnel. In Figure 5.23 the positions G, H, I & J are shown. The measurements were very consistent.

4.3. LDA

4.3.1. System

For the Laser Doppler Animometry 'Dantec Dynamics' equipment was used, more specifically the 'FlowExplorer' in conjunction with the 'F60 BSA flow processor'. The FlowExplorer is a single unit housing all the emitting and receiving optics required for measuring two velocity components. The burst spectrum it puts out, is processed in the processor. The software used to monitor and control the laser, sensor and the traverse was 'BSA flow software' (Dantec Dynamics, 2019a). All relevant specifications of the LDA system are listed in Table 4.1. With the $300\,mm$ focal length, the LDA system was able to measure across the whole width of the measurement section as its internal width plus one wall thickness was $262\,mm$.

The strengths of LDA are that measurements can be done at high spatial resolution and at high frequency, making it an excellent method for producing turbulence level data. As a drawback it has that it is only a pointwise measurement technique.

Table 4.1: LDA system specifications

Laser power	$500\,mW$
Fringe spacing	$1.33\,\mu m$
Measurement volume	$42 \times 41 \times 210\,\mu m$
Stop criterium	$45\,s$
Average data rate	$1.3\,kHz$

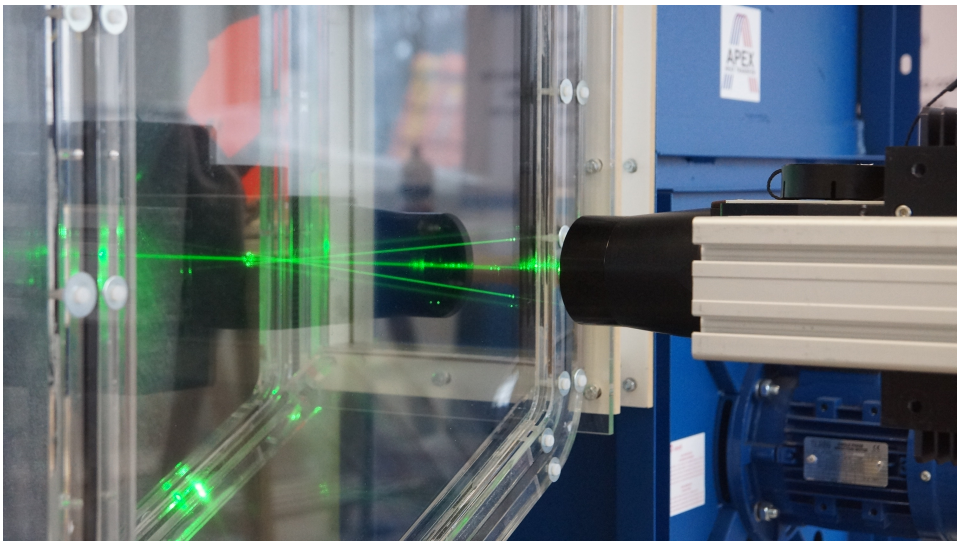

Figure 4.4: Photograph of the LDA system in use.

Stop criterion

For the LDA, at every point the velocity was measured for $45\,s$. This is longer than all characteristic time scales in the flow. In Figure 4.5 it is shown, for a specific point, how the mean velocity measured up to signal i (where i goes up chronologically), progresses when i goes from 0 to n, which is the total number of signals picked up by the sensor. This term is given in mathematical form in Equation 4.1. In the graph it can be seen that mean velocity hardly changes at the end of the measurement, indicating that statistical convergence is reached (note the small range in the vertical axis).

$$\frac{\bar{u}(i)}{\bar{u}(n)} = \frac{\frac{1}{i}\sum_{i=1}^{i} u_i}{\frac{1}{n}\sum_{i=1}^{n} u_i} \tag{4.1}$$

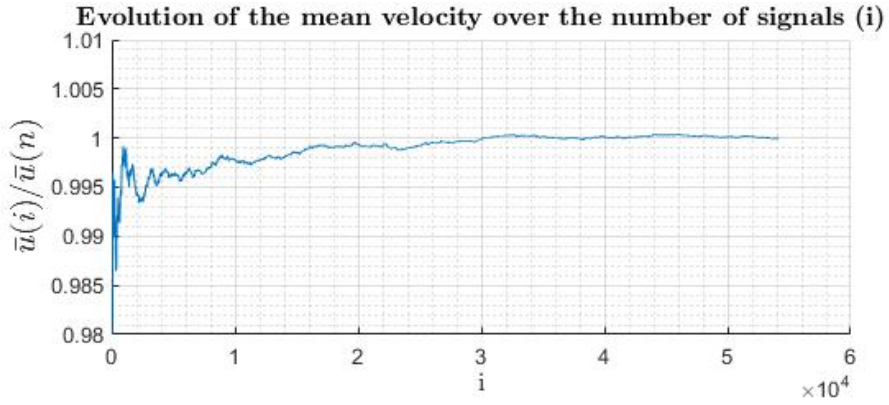

Figure 4.5: For a specific point, $n \approx 54000$ signals were picked by the sensor of the LDA system. The normalized mean from the first signal picked up, to signal number i (on the horizontal axis) is plotted. The normalization was done with the mean velocity over all signals sensed ($\bar{u}(n)$). Note the small range in the vertical direction. It can be seen that the mean velocity hardly changes after some 10000 signals (in other words, time could have been saved for measuring this specific point).

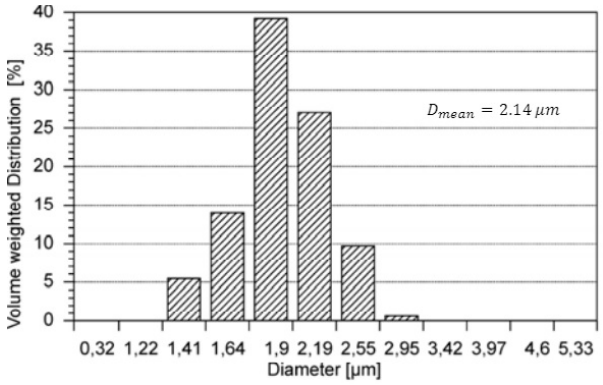

Figure 4.6: Particle size distribution of the DEHS seeding.

4.3.2. Seeding & seeding generator

DEHS (di-ethyl-hexyl-sebacat) was used in conjunction with a seeding generator to supply the airflow with seeding particles. In the seeding generator the liquid is atomized. Making use of the Venturi effect, the DEHS-oil is drawn into a high velocity air stream. Upon entering this stream, the DEHS atomizes. The resulting stream of air with the seeding particles in it is fed to the windtunnel.

4.3.3. Post processing: Zero peak correction

During LDA measurements the quality of the measurement can be checked to some extent by monitoring the measurement histogram. In this histogram, all velocities measured up to the present, are given. The histogram of Figure 4.7 would indicate that the current measurement can be trusted. Now compare it to the top one of Figure 4.8. This last histogram clearly indicates that something is wrong. The peak at zero velocity does not fit ones expectation, considering that the rest of the histogram makes the viewer strongly believe the there is a mean flow velocity of around $21\,m/s$. Looking at the overall shape of the histogram, one will have the strong believe that the true mean flow velocity is around $21\,m/s$. The peak at zero meters per second does not fit to that expectation. The peak at zero velocity is believed to be erroneous and so it must be corrected for before calculating the local mean velocity. A simple algorithm was used: Per measurement point, in the histogram, all data in the range of $U = \pm 2\,m/s$, were rejected and replaced via linear interpolation using the adjacent data. The result is the lower histogram in Figure 4.8, a corrected mean velocity is based on this histogram.

This method can have some drawbacks: Firstly the algorithm does not take into account

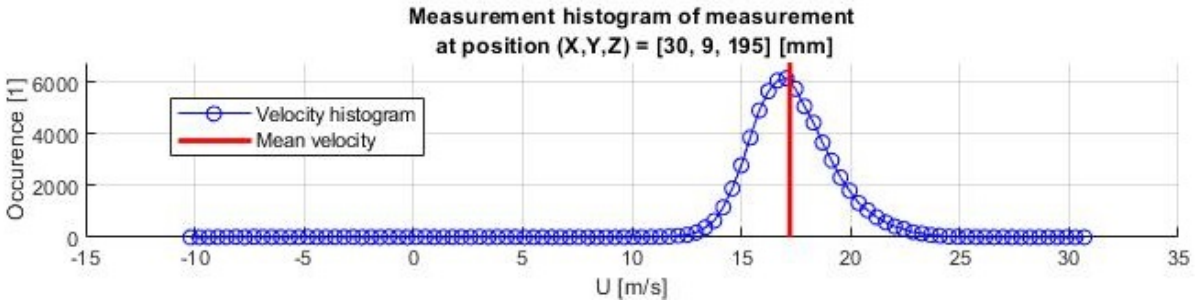

Figure 4.7: A measurement histogram for a LDA measurement.

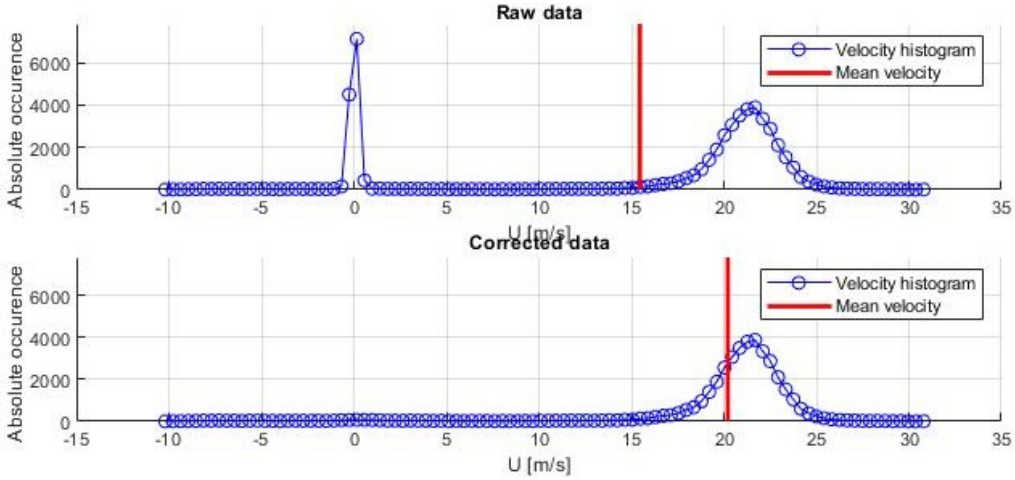

Figure 4.8: The measurement histogram for LDA at a single point. The top plot gives the raw data, with the erroneous peak at zero meters per second. In the bottom plot the corrected data is presented.

that for some points in space, a peak at zero velocity can actually be expected, for these specific points the interpolation will introduce an error. If the true, physical histogram is narrow (in the range of $4\,m/s$) and intersects with the specific interval where the correction is done, this method will not work well (luckily in this specific flow points, were zero velocity does occur in reality, the histogram will most likely be wide).

4.3.4. No slip boundary condition

After the correction for the zero peak that was observed at some points, the velocity data set, was complemented with zeros at the positions of the channel walls. In other words, the zero velocity at the channel walls was not measured as measuring at the wall is not possible with LDA, it was assumed based on the no slip condition.

4.3.5. Some notes on the LDA measurements

As you can see in Table 5.1, LDA measurements were performed at 5 five positions. Three of these brought with them some difficulties. At A the goal was to most accurately characterize the velocity field and so it was required to measure close the walls, reflections of the laser beams were found to be problematic in this. Positions B and D were less relevant, a coarser grid was used and so the above gave no problems in these cases. At positions E and F, the windtunnel had an internal height of $1.61\,m$, which brought with it its own challenges.

Points in the channel inaccessible to LDA

As the LDA system has a focal length of $f = 300\,mm$, and for both sets of lasers, the lasers are spaced by $60\,mm$. This geometry makes it impossible to measure the vertical velocity component in the corners of the duct that are far away in the perspective of the LDA system. See Figure 4.9, in fact for a triangular region (marked in pink) having the same angle as

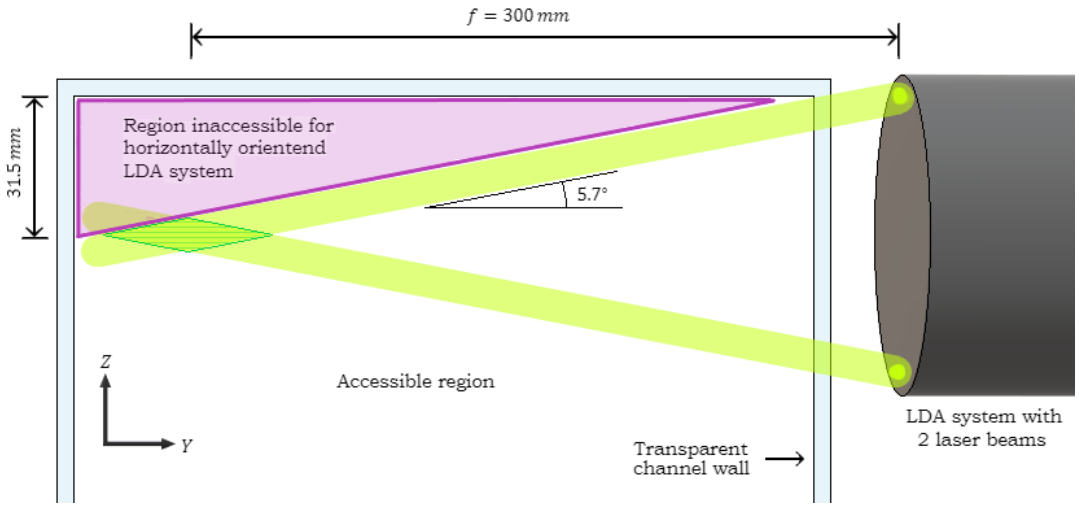

Figure 4.9: Schematic overview of LDA system, it explains how in a certain regions (marked in pink) no LDA measurements can be done, as the one of the laser, the top one in this case, has to pass through the transparent wall at an unfavorable angle).

the half angle the lasers (yellow) have in between them (5.6°) it is not possible to measure there with LDA. This all is under the assumption that refractive phenomena interfere with the measurement too much, as the top laser passes through the top wall of the channel.

In the above text and Figure 4.9 it is explained how measuring the w-component of the flow can be problematic in the far top & bottom edges of the channel. It must be noted that a similar problem occurs for measuring the u-component, however only at positions where the duct is widening in the vertical direction. The two lasers used two measure the u-component of the flow, lay in the horizontal plane. In the case of a diffuser, the laser closest to the diffuser throat will lay above/below the channel if the measurement volume lays close to the top/bottom wall. It must then pass through the perspex wall at an unfavorable angle. This can interfere with the measurement.

Measuring close to the wall

When the measurement volume lies near a transparent surface, the reflections and scattering of the laser beams interfere with the measurement. As said in Section 4.3, the workaround for this was an extra post-processing step, where the too large amount of measured velocities near $0\,m/s$ is filtered out. This worked rather well for some points, but for some points filtering out the peak afterwards was not adequate. The physical model had to be adjusted. Firstly matte black paint was used at specific points on the inside wall, and even when this proved to be ineffective, black velour tape was used. This worked well, however it did introduce small forward and backward facing steps, at the leading and trailing edge of the tape that was used.

Measuring over a large height

As said in Chapter 4, with the traverse it is possible to move the LDA system over $1\,m$ in the vertical direction. At some points this is too little, as the internal height of the channel can be up to $1,61\,m$. To obtain the velocity field at these locations, the cross section was split into an upper and a lower half. Firstly one was measured, then the height of the LDA system with respect to the traverse would be adjusted such that measurements could be performed at the other half. There was some overlap between the two halves, see Figure 4.10. In the left contour plot, the upper half is laid over the lower one, vice versa for the right plot. You can see some discrepancy between the two, however the error made is acceptable. The two data sets were combined, in the overlapping region, the mean value of the two datasets was taken on for further use.

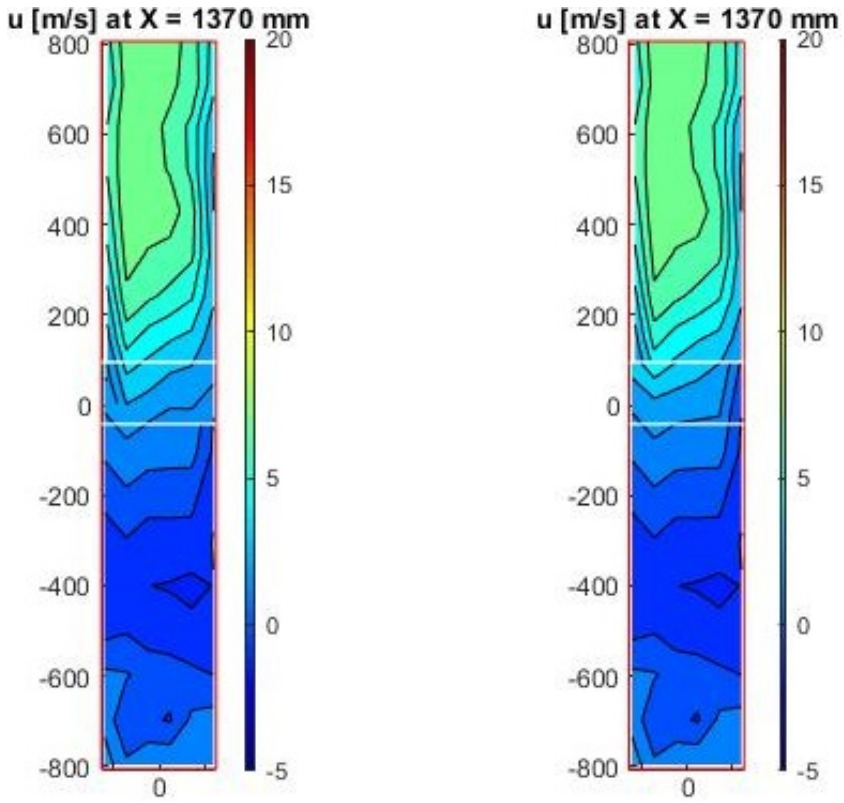

Figure 4.10: Streamwise velocity component at position E (see Table 5.1). Firstly the upper half was measured, then the lower half, the two measurement show good similarity in the region where they overlap. The region in between the white lines at $Y = -42\,mm$ and $Y = 95\,mm$, is where the two data sets overlap.

Measuring close to the floor of the lab

Another difficulty related to the channel height, is that at the same points where the channel height is $1.61\,m$, the duct reaches to within approximately $10\,cm$ of the floor of the lab. It was possible to measure at this height, however only with a tilted laser system, tilted around the X-axis. This means that it was still possible to measure the all-important U velocity component, however the second measured velocity component would then no longer be the W in the coordinate system used throughout. W could only be measured with the LDA system oriented horizontally, and so for the lowest $165\,mm$ of the channel it could not be measured.

Dirt & DEHS oil

At position A, the grid for the LDA measurement consisted of 70 points. Every point was measured at for one minute, and so characterizing the whole cross section took approximately 70 minutes. At other positions this took less time, however it was still in the same order of magnitude. Furthermore it was expected that only in the beginning of a measurement seeding had to be added, however due to a combination of leakage, evaporation and settling down, a constant supply was necessary. All in all this meant that seeding particles had to be added to the flow for a long period of time. When the DEHS oil settles down onto the transparent walls of the measurement section, the optical properties of it are changed. Namely, the oil does not settle into a layer of constant thickness, streaks (characteristic length in order of magnitude millimeters) of oil can be observed on the inside wall, and so the way in which the optical properties change depends on position, see Figure 4.11. If one or both laser beams are deflected too much, the fringe pattern required, changes or disappears if the laser do not any longer intersect. This creates either erroneous measurements or no measurement at all. To prevent this from happening, care must be taken that the surfaces the laser passes through is as clean as possible.

Figure 4.11: Streaks of DEHS oil that has settled down on the inside of the channel. Picture shows part of a door that was removed at the time.

4.4. PIV

In this section the PIV measurements and the related post-processing sequence will be explained. The hardware used for the PIV measurements consisted of a laser, and a CCD camera. The 'Litron Lasers Bernouilli' laser was used, for the camera the $4.3\,MP$ 'Dantec Dynamics FlowSense EO' was used. In Table 4.2 the specifications of the PIV system are summed up.

Table 4.2: PIV system specifications

Laserpulse energy	$200\,mJ$
Wavelength	$532\,nm$
Max. frequency	$15\,Hz$
Camera chip (CCD)	$4.3\,MP$
Camera lens	$24\text{-}70\,mm$
Resolution	120 - $360\,\mu m/pix$
Interrogation area min. size	$16 \times 16\,pix$
Max. particle displacement	13.9
Number of double images	200
Frame rate (double im.)	$10\,Hz$

The laser and camera were mounted on a traverse. After mounting these, the exact settings of both the laser and the camera had to be set. The laser had a variable focal length as the light emitted is not fully coherent, firstly it is convergent and *after* the focal length it is divergent. This focal length can thus be adjusted. This was important to keep in mind when mounting the components to the traverse. Near the region of focus the highest optical power density is reached, which leads to optimum illumination of the seeding particles. There are two requirements that play a role in determining a good focal length for the laser. Firstly, for the reason described above, it is often important to let this region of focus lay within the channel, at the point where the PIV measurement is done[1]. Secondly, the focal length itself determines how *long* the region of focus will be, see Figure 4.12. The longer the focal length, denoted with f_1 and f_2, the larger the length is over which the light sheet has a high optical power density.

This second requirement was something to keep in mind while mounting the laser and camera. A limiting factor in this was the ceiling height: For obvious reasons, the PIV system must at all times stay below the ceiling of the lab. This complicated things as before shutdown

[1] As a remark, there are conditions where it is not beneficial to have the light sheet as thin as is possible, as this makes the PIV system more prone to out of plane motion of the fluid.

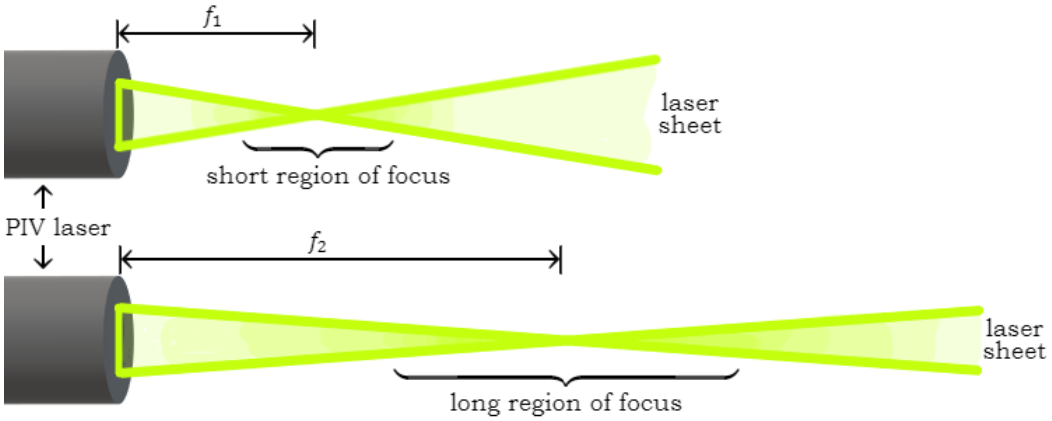

Figure 4.12: Schematic drawing of two PIV lasers emitting a light sheet (not two be confused with a LDA system emitting two separate laser beams). Both light sheets are in the plane that is horizontal and perpendicular to the page. The upper laser has a short focal length f, the lower laser has a longer focal length. The longer the focal length, the more elongated the region is where the laser light sheet is thin enough in order to have adequate optical power density for a PIV measurement.

the traverse would always go to its *home position*, which happened to be at the highest point it could get to, as can be seen in Figure 4.13 this led to small margins.

For the camera, the aperture, zoom and the focus had to be set. The plane of interest should be zoomed in upon as much as possible, and should of course be in focus (now referring to the focus of the camera, not the laser). For performing PIV measurements in larger planes, as was done for position C (Table 5.1 & Figure 5.8), extra considerations had to be made. As a larger plane must be illuminated with the laser, a lower optical power density is achieved and so particles will light up to a lesser extent. To compensate, the camera/lens must be set to a large aperture, as with this will maximize the amount of light getting to the camera chip.

After setting up the laser and camera, the system must be calibrated. For this a calibration target was used, a white A3 sheet with a known dot-pattern printed on it, attached to a flat piece of wood. The target was then carefully placed in-line with the laser sheet, and an image was recorded. With this calibration image the scale factor / magnification factor was calculated.

As a final step, it must be verified that within the image, a reference point is present, in order to place the measurements in space. If no point of reference if present within the particle images, an extra image has to be recorded. A ruler was used, partially placed in the image, with its origin at a known point of reference that lies outside the image, with this it is then known where exactly in space the PIV measurements were performed.

4.4.1. Seeding & seeding generator

For the PIV, the same seeding particles ($DEHS$) were used as with the LDA, and the same seeding generator as with the LDA measurements, see Section 4.3.2.

4.4.2. Post processing

For the PIV measurements the goal was to find the mean velocity field. Directly after capturing the raw particle images, within the environment of the DynamicStudio software (Dantec Dynamics, 2019b), several post processing operation were performed. The goal of these steps was to extract the mean velocity field ($2D2C$) from the 200 double images taken in each plane. The following steps were performed:

- **Image masking:** The regions in the images captured, where there is no flow, are masked. From here and on these specific pixels will no longer be analyzed.
- **Image Min/Max:** In this step, out of the 200 double images, per pixel only the minimum greyvalue is selected. The image built up from these minimum values is said to be the background image.

Figure 4.13: (left image) The requirement for a large focal length for the laser, resulted in the laser being mounted as high as possible. Before shutdown, the traverse would move to its fully up position, leaving only very small margins. (right image) Also when measuring in the horizontal planes, height was an important factor; the vertical distance between the camera and the light sheet had to be at least the height of the channel at the point where measurement where done.

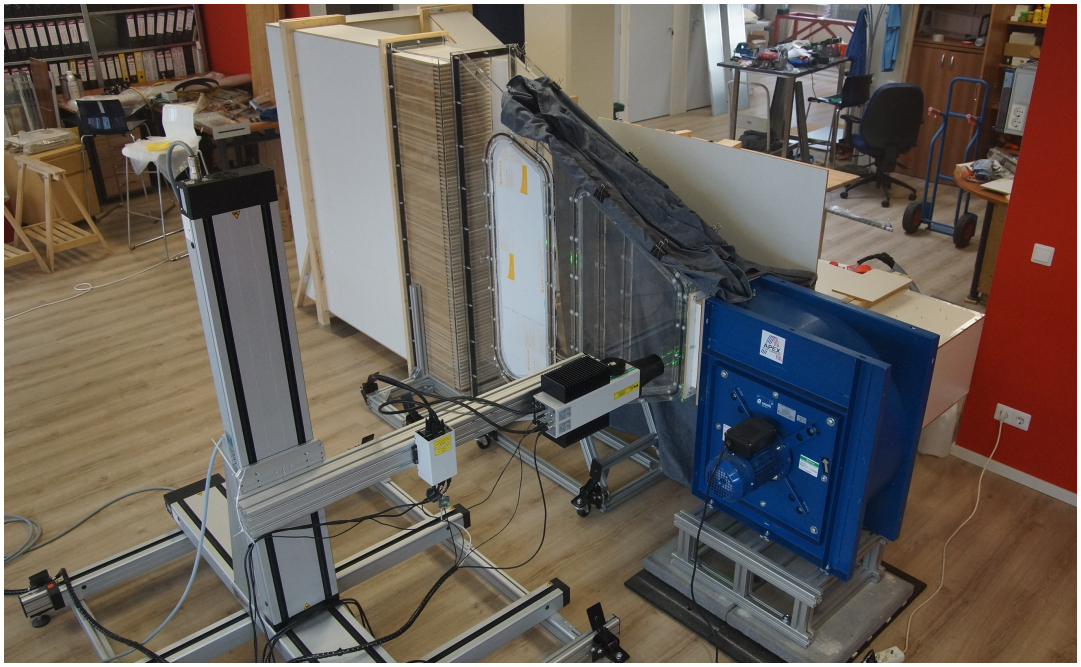

Figure 4.14: Picture of the windtunnel, while LDA measurements were performed.

- **Background subtraction:** The image obtained in the previous step, is now 'subtracted' from all the particle images. The grey value for every pixel is corrected with the minimum grey value that was found. This increases the signal to noise ratio.
- **Adaptive PIV:** The Adaptive PIV is a method for calculating velocity vectors based on particle double images, the method iteratively adjusts the size and shape of the interrogation area in order to adapt to local seeding densities and flow gradients. In this step, the 200 double images, are converted into 200 vector fields.
- **Vector Statistics:** In this last step, the relevant statistics are calculated, based on the 200 vector fields. The local mean, and the root mean square of the two in plane velocity components are found.

After these above steps in the environment of DynamicStudio, the data processing was done with Matlab:

- **Writing data to a 3D Cartesian grid:** From DynamicStudio the data is put out in lists, where in the order of increasing x and then y (in the coordinate system of the image, the local coordinate system) all datapoints are placed. In this first step the structure of the data was changed to a three dimensional array. The coordinate transformation from the local to the global coordinate system, used throughout, was performed here as well. This simplifies further data processing and visualizing in Matlab. The result is a $3D2C$ description of the mean velocity field, which two of out three velocity components are in the set, depended on the orientation of the light sheet for the concerning measurement.
- **Impose no slip condition:** Both with LDA and PIV it is not possible to measure infinitesimally close to the wall, at all times however the velocity at the wall is known. The no slip boundary condition imposes zero velocity at all walls. In this step the positions of the insides of the walls are added to the arrays containing the $X,Y\&Z$ data, and at the corresponding positions in the $\bar{u},\bar{v}\&\bar{w}$ arrays, zeros were added.
- **Combine data sets:** For the PIV measurements, the goal was to obtain a $3D3C$ description of the mean velocity field. To get there, two $3D2C$ (one containing $\bar{u}\&\bar{v}$, the other containing $\bar{u}\&\bar{w}$) datasets would be combined into one. Before this could be done, both datasets had to be interpolated onto a grid where the elements have the same locations in space.

  Interpolate onto new grid: See Section 4.4.3 for a description of this post processing step.

  Combine: This step is described in Section 4.4.4.
- **Obtain the spatial gradient tensor:** Based on the $3D3C$ mean velocity field, the mean gradient tensor can be found.

4.4.3. Interpolation step

As said in the previous section, the data put out by the DynamicsStudio software was rearranged into three dimensional arrays, then the no slip condition was imposed. The next step was to interpolate the data onto a new grid. As explained, the reason for it is to be able to combine the two data sets.

For this step the matlab command 'interp3' was used. It provides several interpolation methods, amongst the options were linear, cubic, spline and 'makima' (a modified akima method). Literature regarding the command (Mathworks, 2019a) claims that the line, surface or volume that is obtained via whichever interpolation method, at all times intersects with the original data points. However it was found that for the interpolation of three dimensional data, only linearly interpolated data intersects with the original data. See Figure 4.15, it gives a comparison of two methods of interpolation when applied to the three dimensional streamwise velocity component field, as measured with PIV in the straight section in between the fan and the diffuser. The value of U is plotted along three arbitrary vertical lines in space, for the original data, for the case of linear interpolation, and for the case of spline

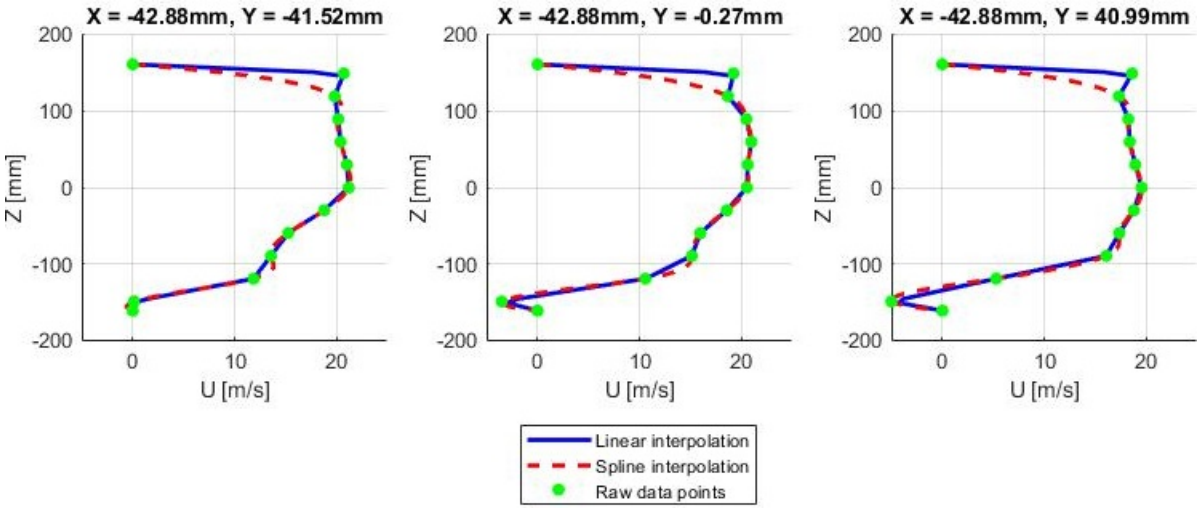

Figure 4.15: The value of $\bar{u}$ is plotted along three arbitrary vertical (X&Y coordinates given above plot) lines in space, for the original data, for the case of linear interpolation, and for the case of spline interpolation. Note that for the case of spline interpolation the interpolated data does not intersect with the original data, in the second data point from the top. Other higher order methods showed behavior similar to that of the spline method.

interpolation. It can be seen that not at all points an intersection occurs between the original data (green dots) and the data found after interpolation with the spline method. The interpolated data, along the lines plotted, has 64 datapoints, the original data has 13 (including two added data points at the wall, for the no slip condition). Other higher order methods showed behavior similar to that of the spline method.

For this reason, the linear interpolation method was chosen. A drawback is that when later on the spatial gradient tensor is obtained, any quantity based on it, will appear very *square* in a contour plot. For the sake of having a nicer plot, it was chosen overcome this by smoothening the data before taking the spatial derivative. The Matlab command 'smooth3' was used for this. As an example, see Figure 4.16 in which the X-component of the vorticity is plotted, for position A (Table 5.1 & Figure 5.8): In the left plot, no smoothening of the linearly interpolated velocity field was performed, leading to this *square* appearance. In the right plot, the data wás smoothened before taking the spatial gradient tensor, the difference can clearly be seen.

4.4.4. Multiplane PIV

With the PIV system at hand, two in-plane mean velocity components can be measured, in a planar region oriented in a streamwise direction. To have knowledge of the complete mean velocity field in a volume, the following method was used:

The volume of interest was sliced up in several planes, both horizontal and vertical. In the vertical planes the mean velocities in the X&Z direction were measured, in the horizontal planes those of the X&Y direction. With the traverse, it was possible to calibrate, and then to measure all planes that e.g. were oriented horizontally. Then the setup was disassembled, reset and calibrated for the vertical planes. After measuring all the planes, the horizontal planes were stacked on top of one another, and the vertical planes were placed side by side. This gave two data sets, both describe the velocity field in a volume in terms of two out of three velocity components. One set contained the $\bar{u}$ & $\bar{v}$ (mean velocity) components, the other set contained the $\bar{u}$ & $\bar{w}$ components. Both datasets were then interpolated onto a grid that is the same for both, this allows for combining the datasets. This grid had a spacing of approximately $10 \times 10 \times 10\, mm^3$. For $\bar{u}$, at every point the arithmetic mean was taken out of the two datasets whereas for $\bar{v}$ and $\bar{w}$, the one value measured was taken on. In the end this gave a $3D3C$ mean velocity field. This method can only be applied to the true mean velocity field. If due to a too short measurement time, no true mean is obtained in at least one of the two data sets, the two are not compatible.

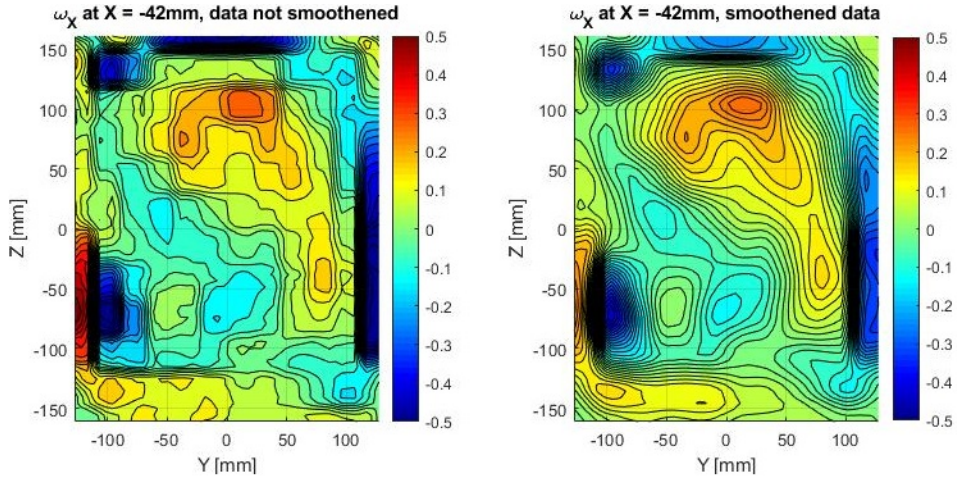

Figure 4.16: In both plots the X-component of the vorticity (ω_X) is shown, in the left plot it is based on the velocity field that has not been smoothened before taking the spatial derivative. In the right plot, the velocity field was smoothened before further analysis. The difference is clear, the right plot looks *nicer*, it must however be stressed that the difference is just an extra processing step, in the end both are based on the same raw data.

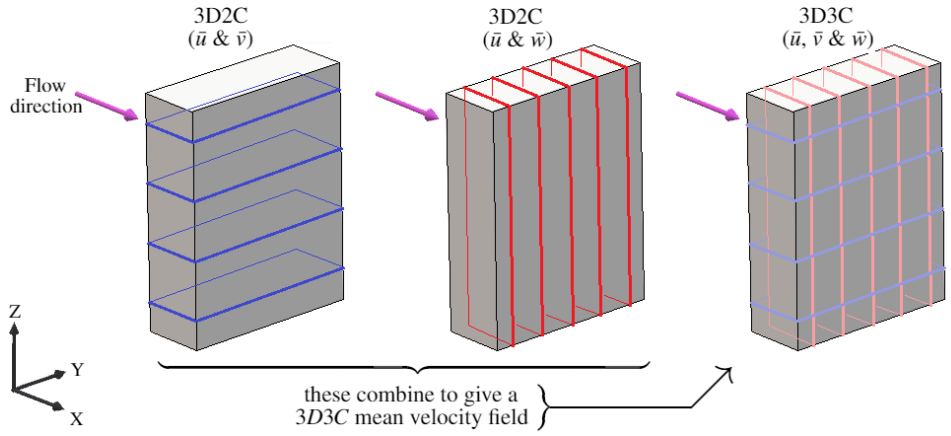

Figure 4.17: Firstly two velocity components were measured in separate planes. This were stacked parallel to each other, this gave a $3D2C$ description of the mean velocity field, two of them to be exact. These were then combined into a single $3D3C$ mean velocity field.

4.5. Data reduction

All data presented in this work, other than velocities and pressures as these were measured, are based on the measured quantities. In this section all relevant formulas used will be given. The formulas will also be given in discrete form. It is worth mentioning that the velocity field was known on a discrete grid with steps ΔX, ΔY and ΔZ.

4.5.1. Performance parameters

In Section 2.5 four performance parameters were defined with which to quantify the performance of a fan-diffuser system. These will be covered firstly (except for the static pressure recovery efficiency, as simply $\eta = C_p/C_p^*$):

Kinetic energy flux factor at diffuser outlet:

$$\alpha = \frac{1}{A}\int_A \left(u/\bar{u}\right)^3 \mathrm{d}A \approx \frac{1}{A}\sum_{i=1}^{i_{max}}\sum_{j=1}^{j_{max}} \left(u_{i,j}/\bar{u}\right)^3 \cdot \Delta Y_i \cdot \Delta Z_j \tag{4.2}$$

Static pressure recovery coefficient: As mentioned in Section 2.5, the traditional one-dimensional definition for C_p is too simplistic for the current case. A definition for C_p more

suited here, is based on surface integrals, see Equation 4.3:

$$C_p = \frac{\Delta p}{\frac{1}{2}\rho \bar{u}_1^2 \cdot \alpha_1} \tag{4.3}$$

The α_1 is as in Equation 4.2. Regarding the term Δp, in Section 2.5 (Equation 2.5a) it was defined as the difference between two surface integrals. These surface integrals had to be approximated however, as the pressure was not measured in the complete cross section (only wall pressure measurements were performed, see Section 4.2). The surface integrals were reduced to a line integrals: In each cross section of interest, along horizontal lines the mean pressure and the mean velocity were taken. Then, these were used in the discrete formula of Equation 4.4, that gives the approximation of the surface integral. Note that b represents the channel width.

$$\int_A pu \, \mathrm{d}A \approx b \sum_{j=1}^{j_{max}} \bar{p}_j \bar{u}_j \, \Delta Z_j \Big|_A \tag{4.4}$$

Time rate of energy dissipation in diffuser: Terms for flow of kinetic energy and rate of pressure work are included here:

$$\dot{W}_{dissipation} = \Delta \dot{E}_{kinetic} + \dot{W}_{pressure} \tag{4.5}$$

The separate terms are given below. A control volume with a single inlet (A_1) and a single outlet (A_2) was assumed. A_1 corresponds to the diffuser throat, A_2 corresponds to the diffuser its outlet. As with the Δp of the static pressure recovery coefficient, for the rate of pressure work term, the surface integral that ideally would be used, was approximated with a line integral. As before, this was a consequence of only performing wall pressure measurements. This approximation is rewritten in Equation 4.6b, and was used to evaluate Equation 4.6a.

$$\dot{W}_{pressure} = \int_{A_1} pu \, \mathrm{d}A - \int_{A_2} pu \, \mathrm{d}A \tag{4.6a}$$

$$\int_A p\bar{u} \, \mathrm{d}A \approx b \sum_{j=1}^{j_{max}} \bar{p}\bar{u} \, \Delta Z_j \tag{4.6b}$$

Kinetic energy terms: The decrease in kinetic energy over the length of the diffuser is as in Equation 4.7a. Separate flows of kinetic energy, in discrete form, are as in Equation 4.7b.

$$\Delta \dot{E}_{kinetic} = \int_{A_1} \frac{1}{2}\rho\bar{u}\left(\bar{u}^2 + \bar{v}^2 \; + \bar{w}^2\right) \mathrm{d}A - \int_{A_2} \frac{1}{2}\rho\bar{u}\left(\bar{u}^2 + \bar{v}^2 \; + \bar{w}^2\right) \mathrm{d}A \tag{4.7a}$$

$$\int_A \frac{1}{2}\rho\bar{u}\left(\bar{u}^2 + \bar{v}^2 \; + \bar{w}^2\right) \mathrm{d}A \approx \sum_{i=1}^{i_{max}} \sum_{j=1}^{j_{max}} \frac{1}{2}\rho\bar{u}_{i,j}\left(\bar{u}_{i,j}^2 + \bar{v}_{i,j}^2 \; + \bar{w}_{i,j}^2\right) \cdot \Delta Y_i \cdot \Delta Z_j \tag{4.7b}$$

4.5.2. Turbulence intensity

For the turbulence intensity multiple definitions can be used, all come with their pros and cons. In general the turbulence intensity is defined as the ratio of the standard deviation of the velocity to some mean flow velocity. What characteristic mean velocity to use, is up for discussion:

- **Mean velocity at given point:** The temporal mean velocity in the specific point can be used. This will give high turbulence levels in region of low velocity, for the same magnitude of the fluctuations.
- **Mean velocity of cross section:** The temporal ánd spatial (over cross section) mean velocity can also be used. Plots showing the turbulence intensity in a cross section will then be easier to interpret, as throughout each cross section the same normalization is used. However still between different cross sections, different characteristic mean velocities are used. Comparing cross sections will then be difficult.

- **Another characteristic velocity:** It makes sense to use a single characteristic velocity for the definition of the turbulence level, with this none of the above mentioned drawbacks will exist. It was chosen to use the mean velocity in the diffuser throat.

To conclude this section, with Equation 4.8 the definition for the turbulence intensity used in this work is given (where σ is the standard deviation of the velocity):

$$\epsilon(X,Y,Z) = \frac{\sigma(X,Y,Z)}{\bar{u}_1} \tag{4.8}$$

4.5.3. Spatial gradient

The spatial gradient tensor of the mean velocity field was found using the Matlab command 'gradient' (Mathworks, 2019b). The spatial gradient was required in order to find the (mean) vorticity components of the flow.

4.5.4. Vorticity

The definitions for the three components of the vorticity used throughout this work are given in the equations of 4.9. They are based on the mean velocity field.

$$\omega_X = \frac{\mathrm{d}\bar{w}}{\mathrm{d}Y} - \frac{\mathrm{d}\bar{v}}{\mathrm{d}Z} \tag{4.9a}$$

$$\omega_Y = \frac{\mathrm{d}\bar{u}}{\mathrm{d}Z} - \frac{\mathrm{d}\bar{w}}{\mathrm{d}X} \tag{4.9b}$$

$$\omega_Z = \frac{\mathrm{d}\bar{v}}{\mathrm{d}X} - \frac{\mathrm{d}\bar{u}}{\mathrm{d}Y} \tag{4.9c}$$

5

Measurements & Results

In this chapter the results of all measurements will be presented without any analysis. The analysis will be given in Chapter 6. Firstly the results of some qualitative measurements, where flexible strips were used to show the local flow direction, will be given. Secondly the transient behavior of the temperature in the system was studied, the goal was to find out whether the system would warm up to such an extent that it would influence the measured variables, and if so, to come up with a strategy to prevent this from happening. Thirdly, for all velocity measurements the results will be shown. Per position the velocities themselves will be presented and the derived quantities such as turbulence intensity and vorticity. To conclude this chapter, the results of all pressure measurements will be given.

Throughout this work, a single test facility and at all times a single coordinate system is used to refer to any position. The origin is located in the centroid of the cross section were the channel starts to widen, see Figure 5.1.

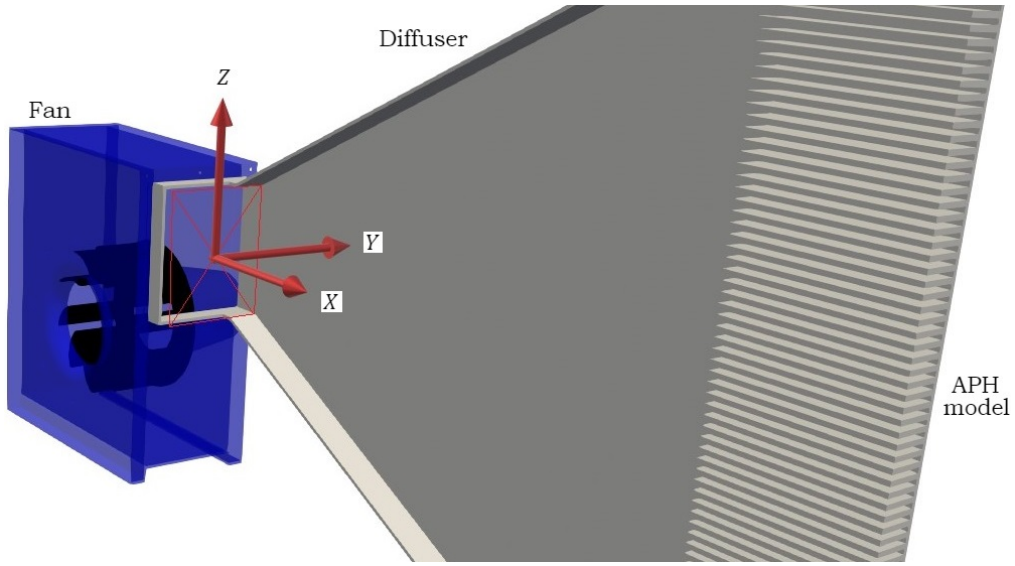

Figure 5.1: Location of the origin used throughout this work: It lays in the centroid of the cross section where the channel starts to diverge. The fan, the diffuser and the air preheater (APH) model can be seen as well. The flow is in the positive X-direction.

5.1. Results from visualization with smoke and plastic strips

5.1.1. Plastic strips

An effort was made to do a large scale visualization with plastic strips that follow the flow. At relevant positions, these were attached to the inner wall, or to a steel rod of $4\,mm$ thickness placed inside the channel. Halfway the diffuser, this rod was glued to the top and bottom walls, such that it was placed vertically in the channel; it is believed to have a negligible effect on the overall flow pattern as the flow in the diffuser is well turbulent. It is also believed that the flow is insensitive to the perturbation of the plastic strips. Note that the strips at positions $1, 2, 3$&4, referring to Figure 5.2, are placed in the vertical centerplane of the duct, whereas those at 5&6 are attached to the left side wall (when looking into the downstream direction). The channel was illuminated with high power LED's and pictures were taken. See Figures 5.2 and 5.3. In the first one, the plastic strips are not adequately visible with the naked eye and so they were highlighted with yellow and red: The yellow dot indicates the position were the strip is attached to the wall or rod, the red stripe indicates the direction the strip has at thát moment, for most positions a good indication of the flow directions at all times. Not all strips however had a fixed orientation, those at positions $1, 2, 3, 4$&5 díd, those just below the centerline, connected to the steel rod (in between 3 and 4) showed large fluctuations, and those in the rectangle at position 6 also showed fluctuations, albeit to a much lesser extent. From this first image it can be derived that a jet exists, it is attached to the top wall. Underneath the jet, there is a large region of recirculation, spanning the whole length of the diffuser. Note that the lengths of the vectors drawn in the photographs have no meaning, they are as long as the plastic strips appear in the photograph, which is merely a projection of its actual length. Interestingly, another smaller recirculation zone was observed, in the lowest corner of the diffuser, indicated by the upward orientation of the bottom two strips, in the right one of the two in the middle, in the rectangle at position 6.

Now moving on and inspecting Figure 5.3, it can be seen that the flow that is attached to the top wall, has a clear nonzero velocity component in the Y-direction. Most likely this indicates that the flow has a swirling motion in it. In Figure 5.4 an interpretation is given of the results of the experiment with the plastic strips. The results are largely as expected, except for the small recirculation zone down low, denoted with the number 2.

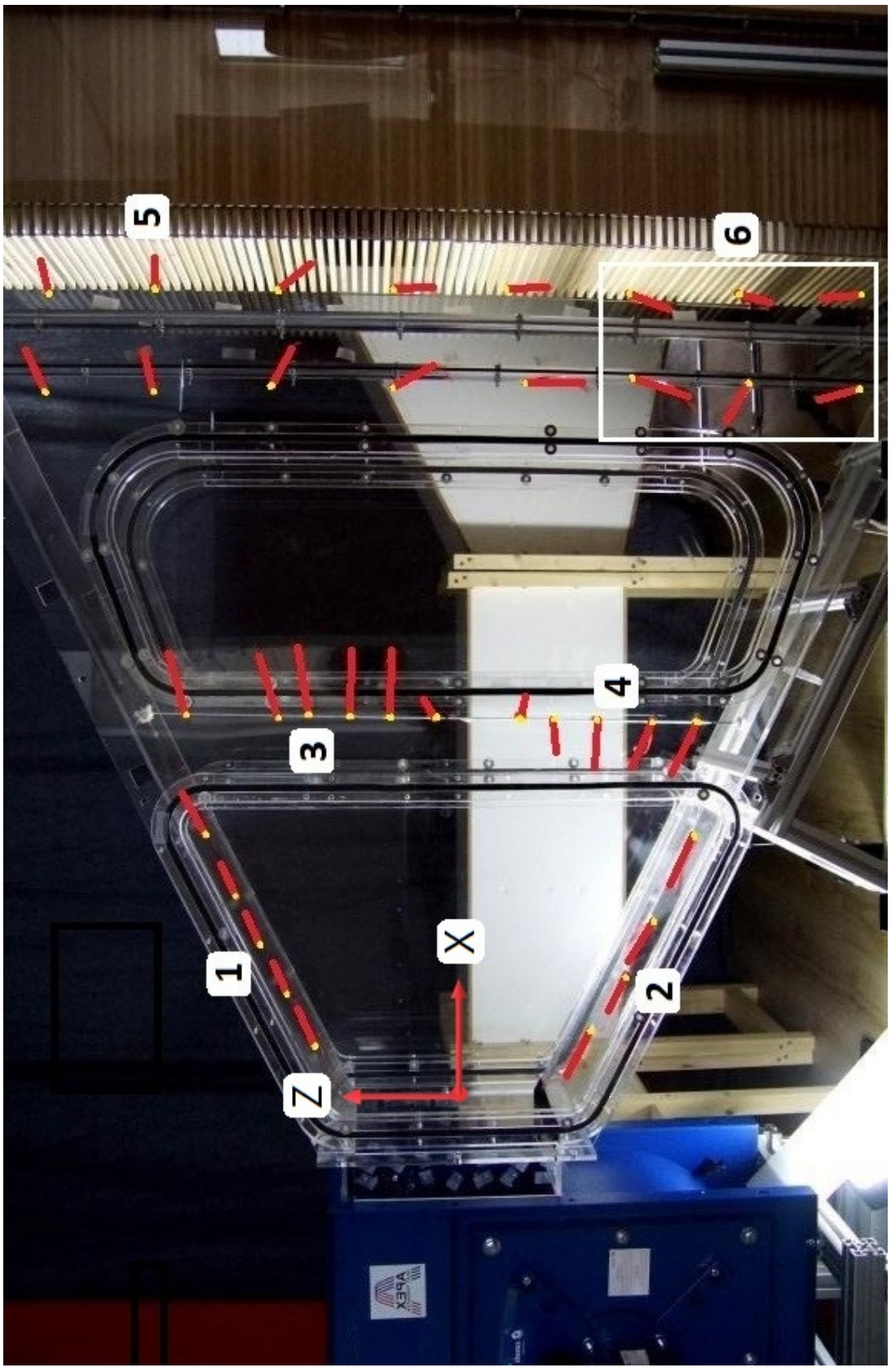

Figure 5.2: A side view of the measurement section of the windtunnel, with plastic strips indicating the local direction of the flow. The strips are highlighted here in red, the *base* of the strip is marked in yellow.

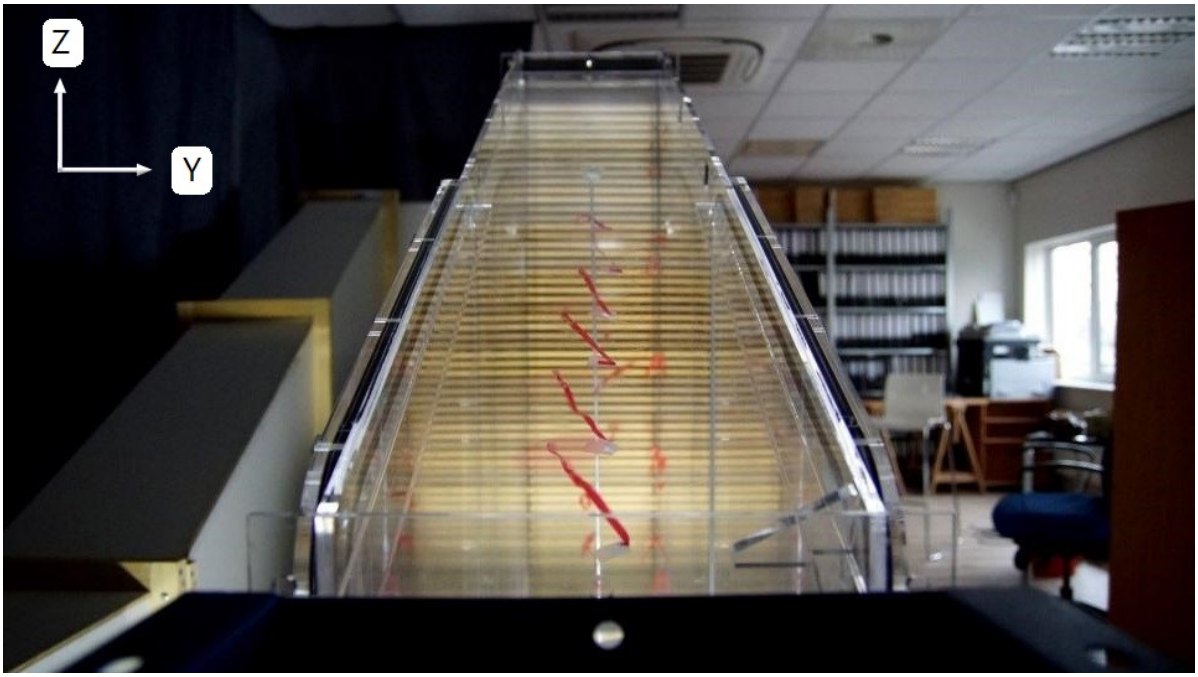

Figure 5.3: A view from the top surface of the diffuser. Note how the strips show that the jet, attached to the top surface, is swirling. This image was mirrored along its vertical centerline (and does not agree to other drawings of the windtunnel).

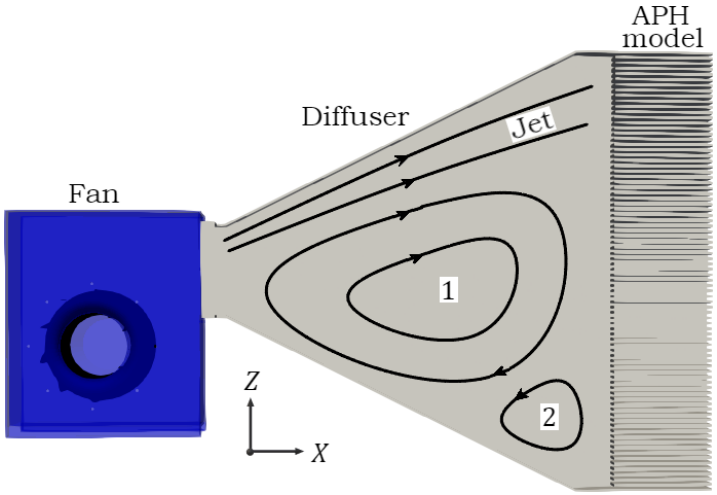

Figure 5.4: Schematic drawing of large scale structures in the flow, derived from the visualization with plastic strips in the flow.

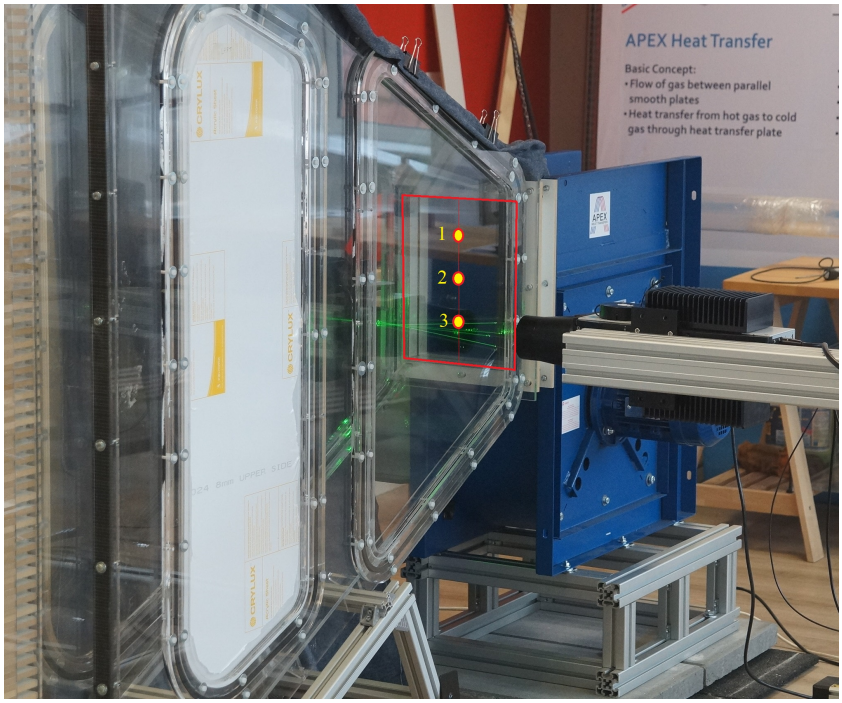

Figure 5.5: Points were measurements have been performed, specifically aimed at mapping the transient behavior of temperature in the windtunnel.

5.2. Transient behavior of temperature

For the LDA and PIV measurements it is desirable to measure at the highest possible resolution, which is inherent to measuring for a longer period of time. Solely taking into account the measurements resolution, more measurement points is better. However over time the air entrained in the system will heat due to the movement of the fan blades. This heating could influence the measurements, which is undesirable. So, before measuring the velocity field at relevant positions, it must be known how the temperature in the system develops over time when the fan is running, and whether this has an effect on the velocity field. In order to make a well informed decision on the measurement grid, an experiment was conducted, where over time the air temperature in the system was monitored, and where LDA measurements at three points would show the (if any) development of the velocity field over time.

5.2.1. Method

The velocity field was measured at three points, see Figure 5.5. Measuring all of these points took $87\,s$ from start to end (at $20\,s$ per point, the remainder is taken up by the moving of the traverse). Compared to the time scales expected for possible thermal effects, a negligible amount of time and so it was said that the velocity field measurements were instantaneous. The temperature was monitored with a thermometer (Omega HH12C) and two K-type thermocouples; one was placed with its tip in the middle of the return duct, where as the other one was placed in the ambient air. It is assumed that the temperature throughout the system, is constant at any given time. From startup the velocity at the 3 points in the diffuser and both temperatures were recorded at intervals of 10 minutes. For the laser measurements the system settings were constantly adjusted in order to obtain a data acquisition rate near $1kHz$.

5.2.2. Results

Firstly, looking at the dynamic behavior of temperature (see Figure 5.6), it can be seen that the temperature of the air within the system relative to its surroundings increases from 0 to

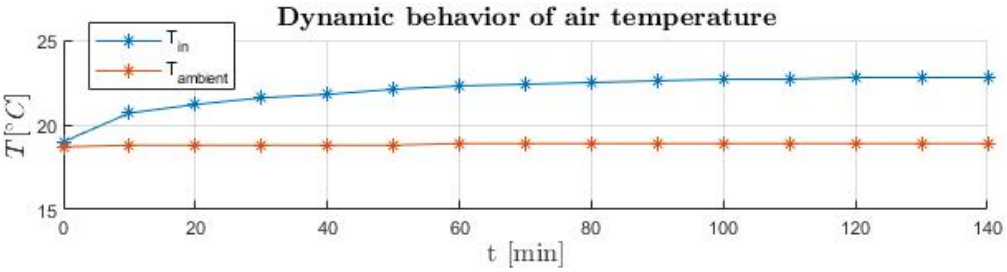

Figure 5.6: Dynamic behavior of air temperature in ducting, at the end, the temperature difference is $4.0°C$.

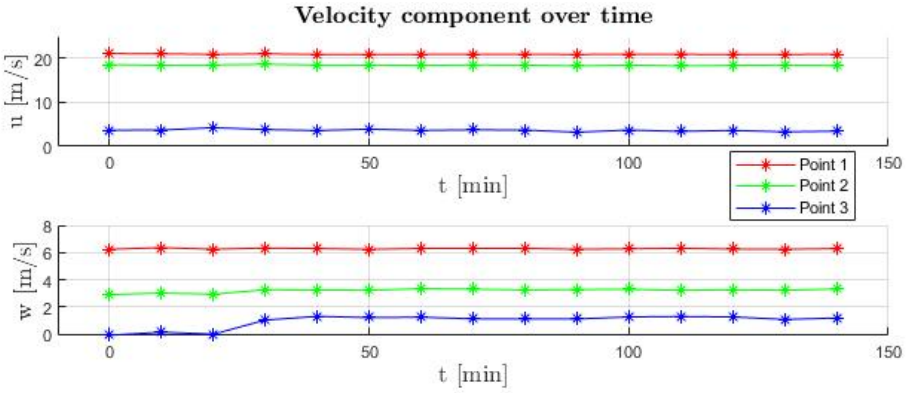

Figure 5.7: Local mean velocity at three points over the time of measurement.

approximately $+4.0°C$, over a time period of 140 minutes. It is assumed that a more or less steady state has been reached at that time, measuring for a longer period of time would have provided little more information, and so measurements were stopped. Between temperatures of $260K$ and $320K$, an increase in temperature of $4.0K$ will give at most a change in density of -1.6%, and at most a change in dynamic viscosity of $+2.5\%$. It is hard to predict how sensitive the system is to these changes, however it is possible to look at how the velocity changes over time. Looking at the dynamic behavior of the three measured velocities, it can be seen that they are largely constant. Only the velocity in the point 3, the lowest point, shows a sudden increase at 25 minutes into the measurement. It is unknown why; three (the first three) erroneous measurements are unlikely to be the cause, as the particle counts for the LDA measurements were all good.

The experiment was repeated in order to see if this sudden increase in the W velocity component at point 3 repeated itself. It did not and with that said, it is not worth the effort of diving deeper into this small anomaly.

5.2.3. A criterion for maximum measurement time

The dynamic behavior of the temperature is as expected. Initially the temperature in the system rises relatively quickly, before converging slowly towards a steady state temperature difference with the surroundings. Several approaches to the problem are:

- Let system warm up, by letting the fan run for some time.
- Actively heat the system, in order to speed up the warming up process.
- Measure at a coarse grid.
- Measure at a coarse grid, that does get finer towards the edges of the duct.
- Measure at a random grid.
- Reduce the measurement time per point or plane.

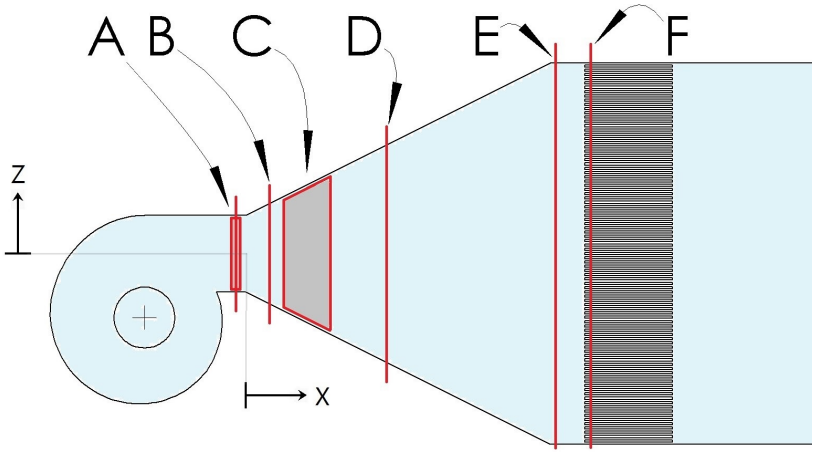

Figure 5.8: Position where laser optical velocity measurements have been performed, in Table 5.1 it can be seen per position, what quantities were measured. At position A, with LDA a cross section was characterized, and with PIV a volume was characterized (see Table 5.1). The plane coincided with this volume, which explains why at position A both a plane ánd a volume are highlighted.

- Use a semi-closed loop, making use of air replacement.
- Accept a theoretical error, take no action.

In the end what is important, is that the measured quantities do not change over the course of a measurement (or several, if datasets are combined). Looking at the transient behavior of the temperature in the system, it is clear that no action aimed at reducing the measurement time, has to be undertaken. Even when measuring for an extended period of time, from initial startup of the fan, it is unlikely to have data disturbed by an increasing temperature.

5.3. Velocity measurements: Results

In the oncoming sections the results of the measurements will be presented, in the order of the position along the centerline of the diffuser. Per position, firstly the measured variables will be given, i.e. all velocity components measured at thát specific cross section (these differ per method used, LDA or PIV). After that, the quantities derived from the measured variables will be presented. In table 5.1 an overview is given of the positions where measurements have been performed, also it is shown what variables have been measured per position.

In total, at six positions (planes or volumes) the velocity field was measured, for reference, the cross sections are marked and denoted with $A, B, C, D, E\&F$ in Figure 5.8. With knowledge of the flow at these cross sections, it can be observed how the flow develops over the length of the diffuser. Depending on the position, either both LDA and PIV, or one of the two methods was used.

Position in Figure 5.8	X-coordinate(s)	Method	Measured quantity	Remark
A	-62 to $-24mm$	PIV	UVW	Diffuser throat
A	$-41\,mm$	LDA	U	”
A	$-41\,mm$	Manometer	p_{wall}	”
B	$100\,mm$	LDA	UW	
C	160 to $350mm$	PIV	UVW	
D	$595\,mm$	LDA	UW	
E	$1370\,mm$	LDA	UW	Diffuser outlet
E	$1370\,mm$	Manometer	p_{wall}	”
F	$1455\,mm$	LDA	U	Inside channels

Table 5.1: Overview of measurements performed, in the measurement section of the windtunnel (some other measurements were done throughout the length of the windtunnel).

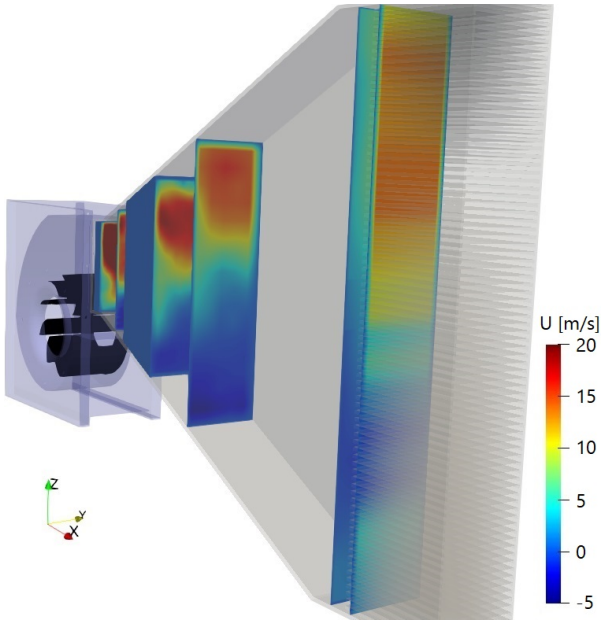

Figure 5.9: Results of all velocity measurements, colouring is linear to the X-component of the fluid velocity.

5.3.1. Interpretation of visually presented data

For the following sections it is important to be aware of several conventions used for plotting the results. Throughout this chapter 'filled contour plots' are often used for visualization; as a convention it was chosen that the point of view is at all times such that the reader will be looking into the upstream direction (this can also be seen by looking at the directions of the positive Y and $Z-$axes that reveal that the positive X-axis points out of the paper, and comparing it to Figure 5.1. Another convention is that for all the filled contour plots that show the fluid velocity component along the X-axis, the same color range is used, namely from -5 to $20\,m/s$, independent of the range of the data plotted. For all contour plots in this chapter the actual range of the data plotted is given in the description, between brackets. Furthermore, in most of these contour plots white dots can be seen, these indicate the exact positions at which measurements have been performed. For the case of LDA measurements they can clearly be distinguished from one another, for PIV however, a dot is plotted per interrogation area in the PIV planes and as these lie closely together, white lines appear in the graph, these show the plane of the PIV measurement.

As a preview, in Figure 5.9, u is shown at positions A through F, to better be able to interpret the plots that follow from here. It can be seen how the jet described earlier in Section 5.1, sticks to the top surface of the diffuser.

5.3.2. Results: Position A

Out of all, at position A, most measurements have been performed. Here the results from LDA, PIV and wall pressure measurements will be presented. Also measurements have been done on the fan without any ducting, for the sake of comparison these results will be shown as well.

Measured quantities

Inspecting Figures 5.10a and 5.10b, in which u is shown as measured by LDA and PIV, good similarity between the two plots can be seen. This, to some extend, proves the quality of both measurements. In Figure 5.11a the v component of the flow is measured, the plot is consistent with earlier observations made with the plastic strips attached to the top wall of the diffuser, see Figure 5.3 in Section 5.1. Here it was assumed -maybe somewhat prematurely- that the jet has a swirling motion, this however is confirmed by looking at Figure 5.11b, in which it can be seen that on the left and right sides of the jet, an up- and downward motion exists. In 5.12 all velocity components are plotted, u is shown with the contours whereas

v & w are presented with the white vectors. Here again, clearly it can be seen that the jet has a secondary, swirling motion.

It is worth mentioning that the inlet of the fan is on the left side (negative Y) and that the axis of rotation of the blades lies at a negative Z, also note that -as throughout this work- the reader is looking in the upstream direction. The direction of the swirling motion is then consistent with the direction expected by intuition, considering the placement and rotation of the fan blades. In Figure 5.13 the mean u is compared for the LDA and PIV measurements, along four lines in space. Very similar results were found.

Derived quantities

When it comes to turbulence intensity, the two measurement techniques again show very similar results, see Figures 5.14a and 5.14b.

In Figures 5.15a, 5.15b & 5.15c all three components of the vorticity are plotted, these are derived from the $3D3C$ mean velocity field measured with the multi-plane PIV approach described in Section 4.4.4. The plots are as expected, as ω_Y and ω_Z have peaks near the top/bottom and left/right walls respectively, although it must be said that the vorticity found in these regions depends heavily on the grid and the way in which the no slip boundary condition is enforced. Furthermore, it does not come as a surprise that these plots of the vorticity are consistent with the velocity field, simply because they are derived from them, all that is proven is that the algorithm that calculates the vorticity components is correct.

Fan without ducting

As said, LDA and PIV measurements where performed as well on the fan without any of the ducts installed. These measurements were considerably more easy to do, as due to the absence of any perspex channel walls, hardly any reflections were present. On single complication had to do with the seeding, with the fan blowing freely into space, and collecting the air from this same large space, it was harder to have seeding that was dense enough, and adequately spread out.

For the case of the fan without ducting, the LDA measurements were performed at a plane parallel to the fan outlet, $100\,mm$ (corresponding to $X = 32\,mm$ in the coordinate system used for the windtunnel) in the downstream direction. In this plane, only within the projection of the fan outlet measurements were performed, for the next time it would make more sense to include some of the surrounding area.

For the PIV measurements measurement wére done outside of this projection of the fan outlet. The volume that was characterized extends from the fan outlet, to $400\,mm$ downstream of it (corresponding to $X = 332\,mm$ in the coordinate system used throughout this work).

In Figures 5.16a and 5.16b, it is plotted how u was measured with LDA and PIV. As opposed to comparisons made between LDA and PIV for the case with ducting installed, not very good similariy is seen. When comparing the profile of u for the case with (Figures 5.10a & 5.10b) and without the ducting, it can be seen that the ducting plays no significant role in determining the velocity profile. This observations holds also when inspecting Figures 5.17, 5.18a, 5.18b and 5.19, in which the other velocity components are plotted.

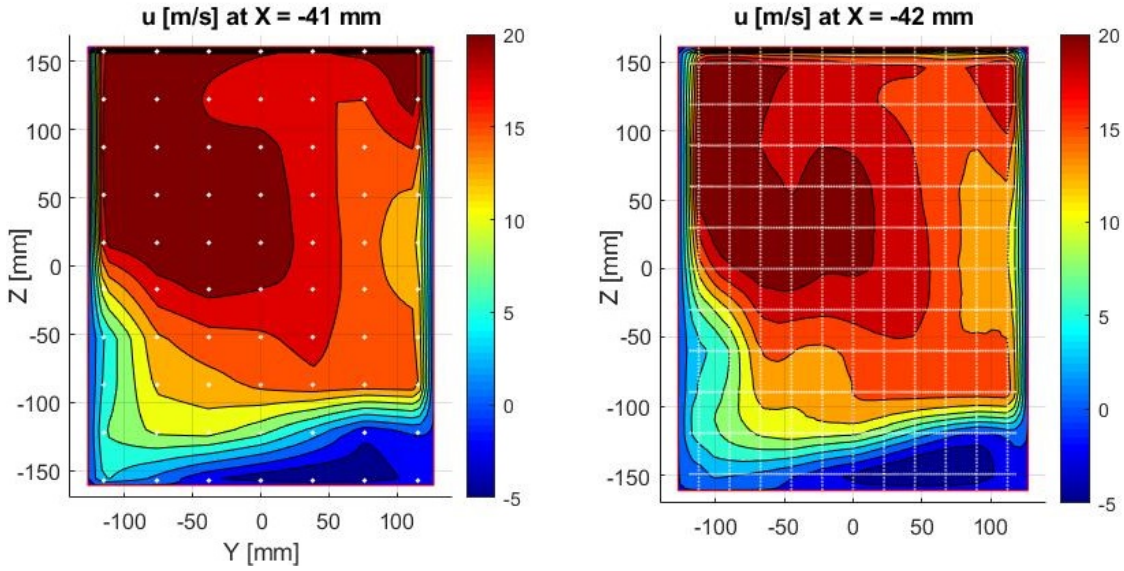

(a) $\bar{u}$ as measured with LDA ($-4.7 \rightarrow 22.1\,m/s$). (b) $\bar{u}$ as measured with PIV ($-5.0 \rightarrow 22.8\,m/s$).

Figure 5.10: The results of the LDA and PIV measurements showed good similarity to one another, indicating the quality of the measurements.

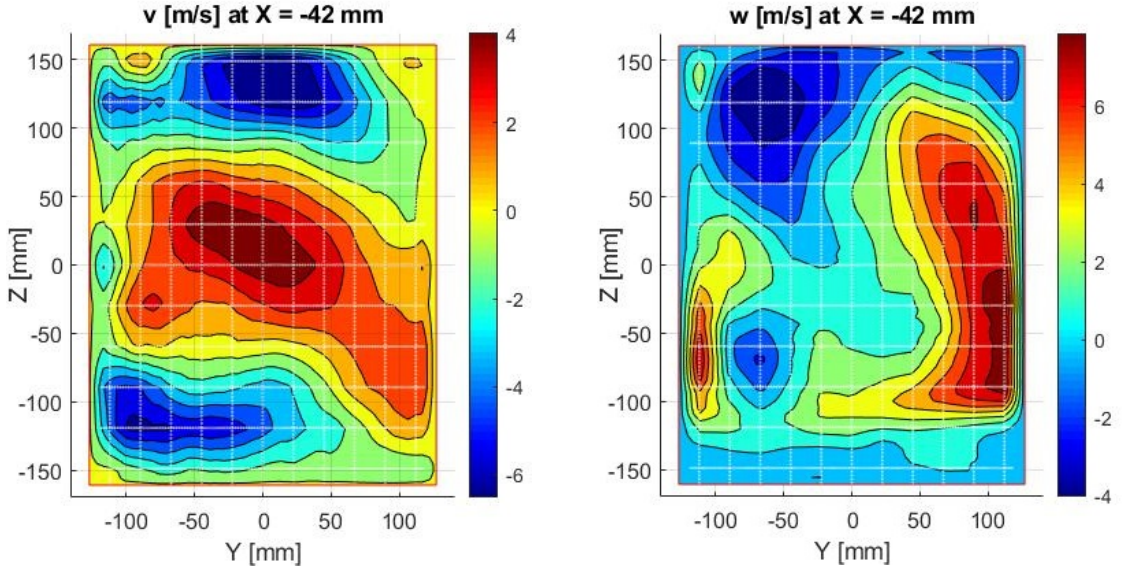

(a) $\bar{v}$ as measured with PIV ($-6.5 \rightarrow 5.1\,m/s$). (b) $\bar{w}$ as measured with PIV ($-4.0 \rightarrow 9.1\,m/s$).

Figure 5.11: The two transverse velocity components (v & w), measured with PIV.

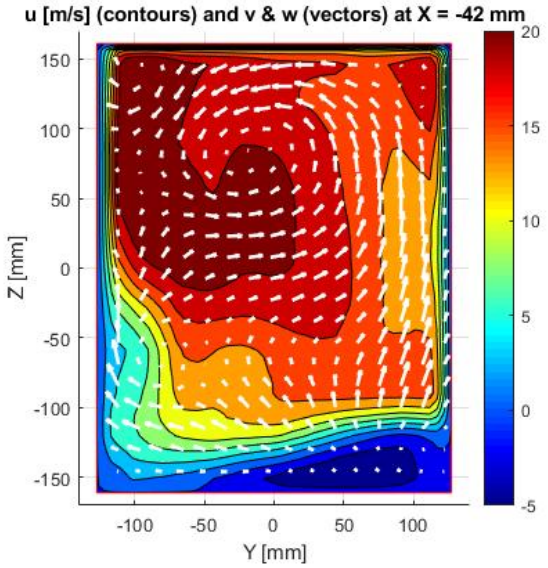

Figure 5.12: All three velocity components plotted in a cross section. The absolute values for $\bar{u}$ have the range $-5.0 \rightarrow 22.8\, m/s$, $\bar{v}$ & $\bar{w}$ can be read of in Figures 5.11a and 5.11b. A swirling motion can be seen, about the point $(Y, Z) \approx (-20, 80)\, mm$.

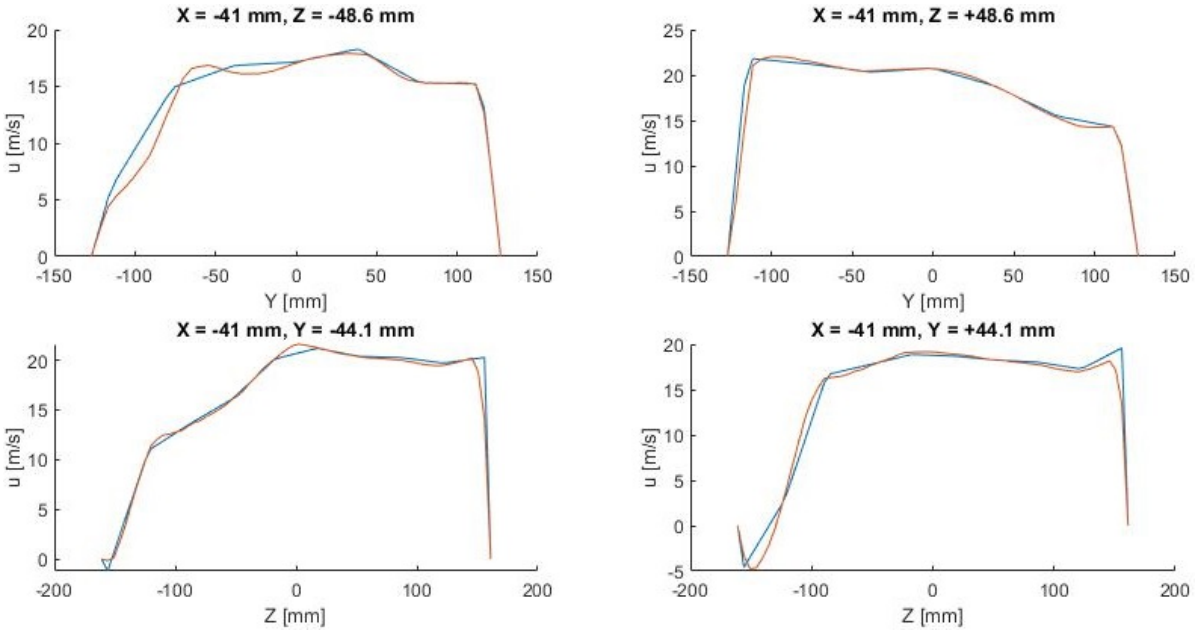

Figure 5.13: Here, along four arbitrary lines in space the streamwise velocity component is plotted for comparison. The blue line represent the LDA measurement, the red line represents the PIV measurement. Above the plots the specific location of the line is given.

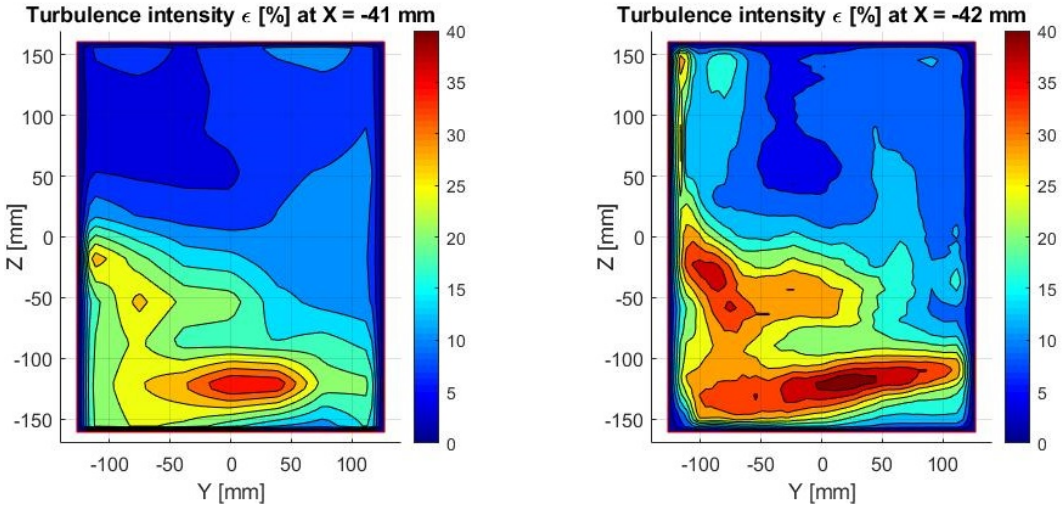

(a) LDA ($0 \rightarrow 37.5\,\%$) (b) PIV ($0 \rightarrow 44.5\,\%$)

Figure 5.14: The turbulence intensity given in percentages, for the two measurement methods used. These two plots use the same color scaling.

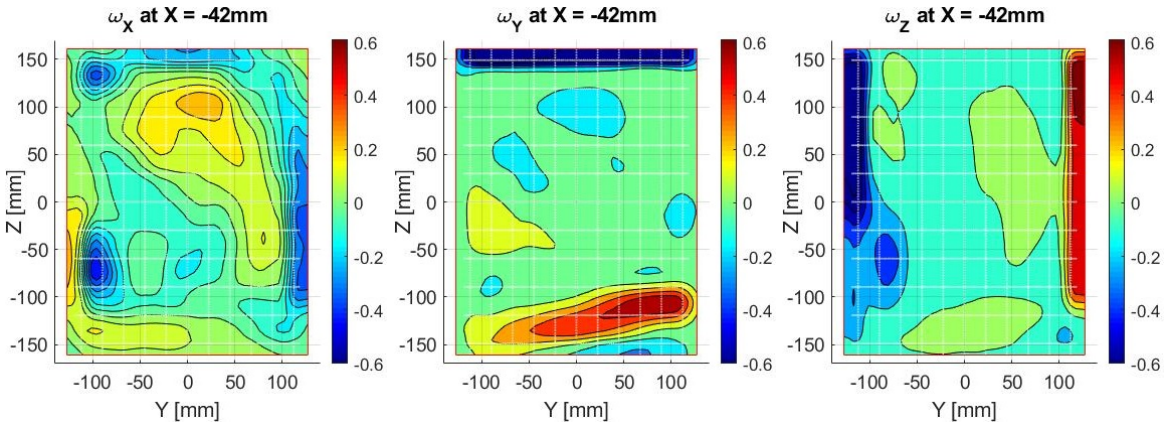

(a) X-component ($-0.3 \rightarrow 0.4\,\frac{m/s}{mm}$) (b) Y-component ($-0.9 \rightarrow 0.7\,\frac{m/s}{mm}$) (c) Z-component ($-0.9 \rightarrow 0.8\,\frac{m/s}{mm}$)

Figure 5.15: All three components of the vorticity, derived from the PIV measurements. For these three plates the same range is used for the coloring.

The below plots (Figures 5.16a through 5.20) apply to the fan without any ducting, blowing freely into the atmosphere. For these plots the origin has the same position wrt. the fan as with all other plots (for the cases with ducting). The plane of $X = 32\,mm$ corresponds to a plane parellel to the fan outlet, at $100\,mm$ downstream of it.

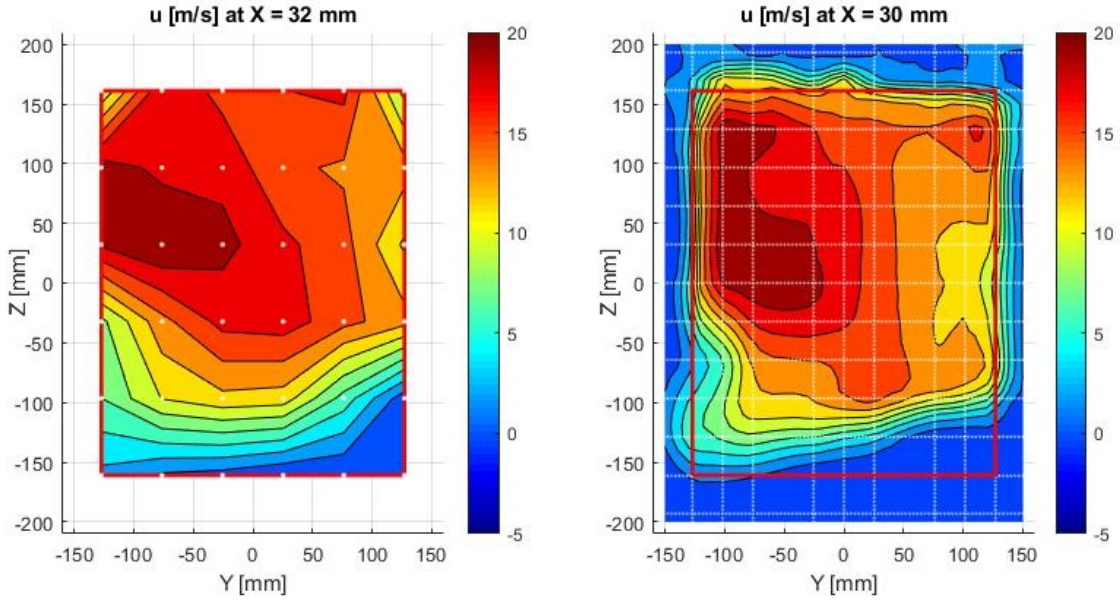

(a) $\bar{u}$ as measured with LDA. $(-0.2 \rightarrow 20.9\,m/s)$ (b) $\bar{u}$ as measured with PIV. $(-0.6 \rightarrow 21.1\,m/s)$

Figure 5.16: Two velocity fields (u) for the fan blowing freely into space. As for the case with the ducting installed, there is good similarity between the velocity field measured with the two methods.

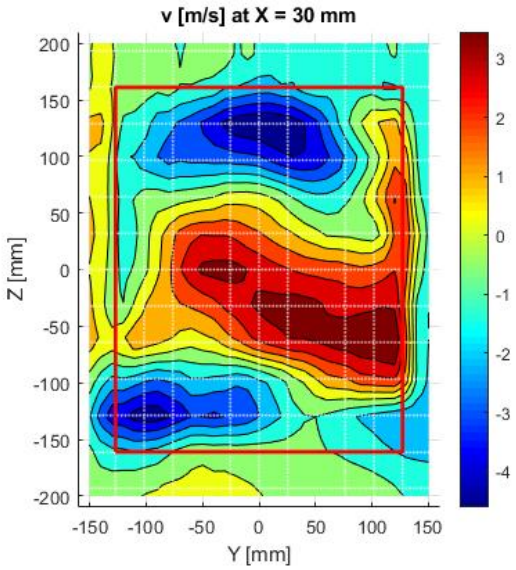

Figure 5.17: $\bar{v}$ as measured with PIV, for the case of the fan without ducting. $(-4.6 \rightarrow 4.3\,m/s)$

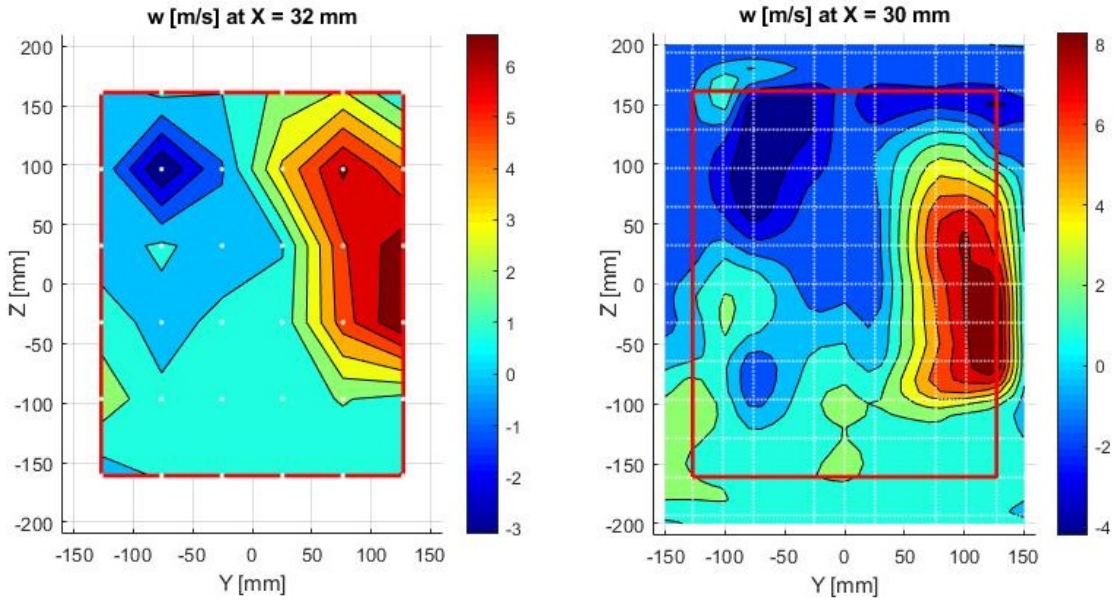

(a) $\bar{w}$ as measured with LDA. $(-3.1 \rightarrow 7.6\, m/s)$

(b) $\bar{w}$ as measured with PIV. $(-4.2 \rightarrow 9.5\, m/s)$

Figure 5.18: The vertical mean velocity component for the fan without ducting.

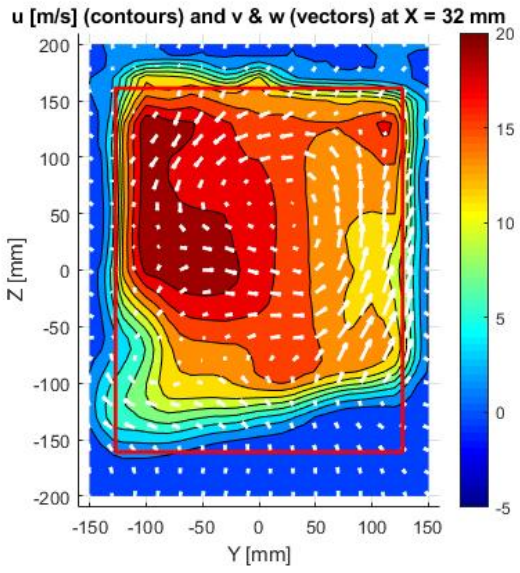

Figure 5.19: All three velocity components as measured with PIV, for the fan blowing freely into the atmosphere. For the case of the fan as with windtunnel, a swirling jet was observed. The same goes for this case of the fan without any ducting. The absolute values for v & w can be read of in Figures 5.17, 5.18a and 5.18b.

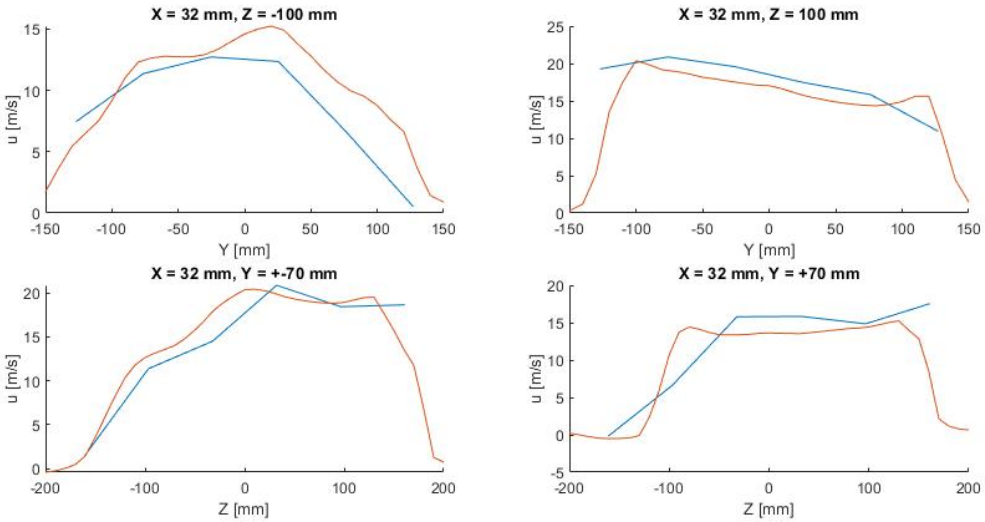

Figure 5.20: Here the value for u, along four arbitrary lines in space, is plotted. The blue line gives the result of the LDA measurement, the red line gives that of the PIV measurement.

5.3.3. Results: Positions B, C & D

At the intermediate positions B, C and D, the results revealed no new information. For this reason these are placed in the appendix, in order to keep this chapter as clear as possible. See Appendices B.1, B.2 and B.3.

5.3.4. Results: Position E

In Figure 5.21a it can be seen that the jet is still attached to the top wall, however its cross section has increased significantly. In Figure 5.21b shows the vertical velocity component, below the jet, a large downward motion was measured, this consistent with the large recirculation zone of Figure 5.4. Due to some technical difficulties, it was not possible to measure $\bar{w}$ in the lowest region of the channel. The turbulence intensity still has the peak slightly below the jet, see Figure 5.21c.

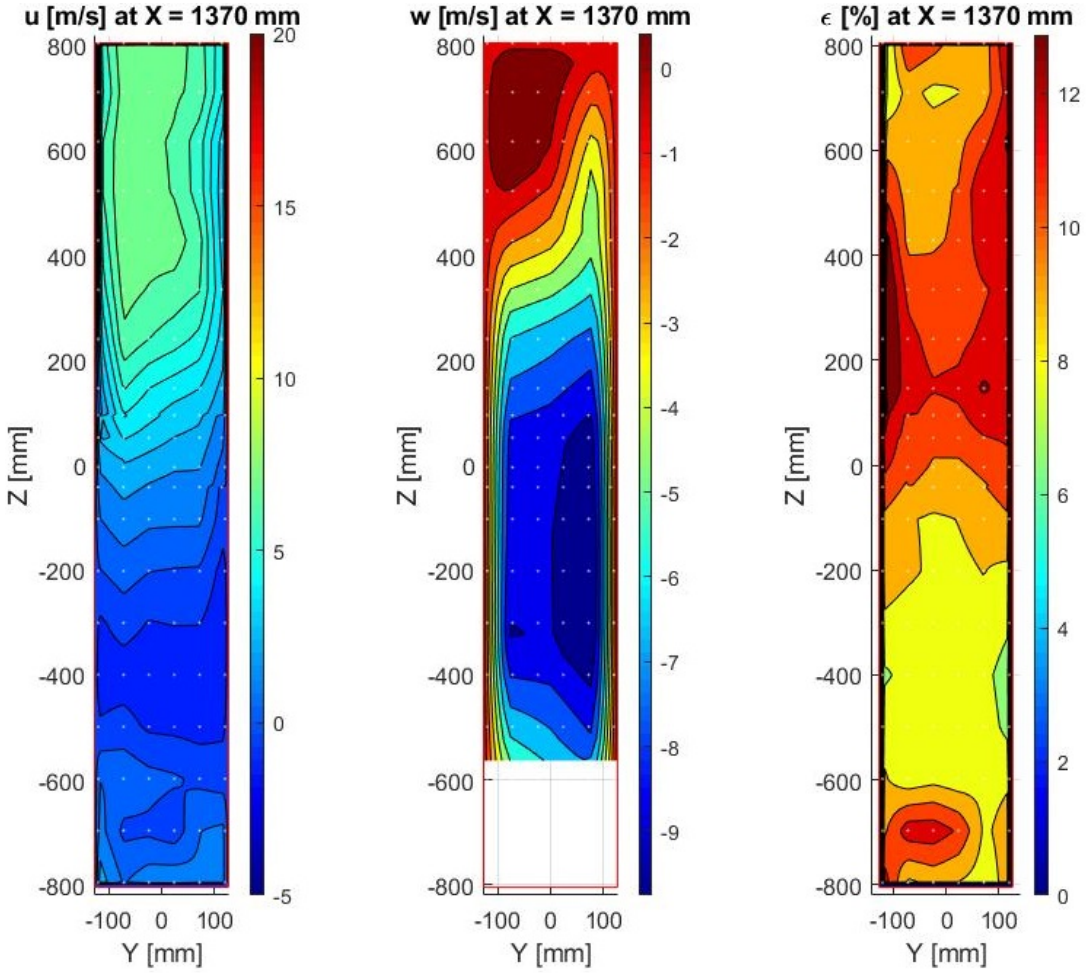

(a) The $\bar{u}$ velocity component. $(-1.2 \rightarrow 7.8\,m/s)$ (b) The $\bar{w}$ velocity component. $(-9.8 \rightarrow 1.4\,m/s)$ (c) The turbulence intensity. $(0 \rightarrow 14.2\,\%)$

Figure 5.21: The results of LDA measurements at position E.

5.3.5. Results: Position F

Here, the velocity inside the channels was measured, at $25\,mm$ into the channels: In every other channel a single measurement was performed at $Y = 0\,mm$. See Figure 5.22: To be consistent with the presentation of data at other positions, a contour plot is used to show the mean velocity field. However, $\bar{u}$ was only measured along a single line. So to not give the impression that the velocity was measured in a plane, also a line plot is given.

Note that at position F, the measured velocities are considerably higher than those at position E (Figure 5.21a). This is as expected; the plates of air preheater model at position F reduce the flow area by half. A final observation must be that near $Z = 400\,mm$, back flow is observed. This is consistent with the smaller recirculation zone shown in Figure 5.4.

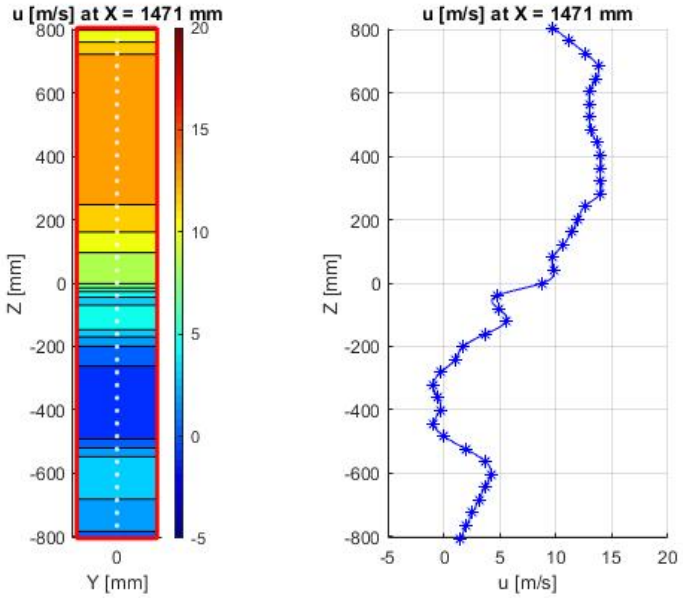

Figure 5.22: The velocity as measured with LDA, inside the channels of the stack of plates. Please note the specific points where a measurement has been done; these lay along a single line. The contour plot is shown to be consistent with the presentation of data at all previous positions, but let it not give the impression that measurements where performed all over the cross section. $(-1.0 \rightarrow 14.1\,m/s)$

5.4. Pressure measurements

Wall pressure measurements were performed at six cross sections throughout the windtunnel, see Figure 5.23. Amongst them are positions A and E, again referring to Table 5.1 and Figure 5.8, as knowledge of these pressures is required for assessing the systems performance. The numbers in the figure (5.23) indicate at how many separate points per cross section a measurement was taken. For the cases of cross sections A and E (diffuser throat & outlet), you can see in Figure 5.24 where exactly the measurements were taken. Here, every wall pressure measurement is represented with a vector that also gives the measured value. For the return duct the number of measurement points was spread out evenly along the perimeter of the channel.

As only wall pressures were measured, it was not possible to find a mean pressure over a cross section by solving the surface integral of Equation 5.1, which would have been the preferred method, see Section 2.5.

$$p = \frac{1}{Q} \int_A pu \, \mathrm{d}A \tag{5.1}$$

For positions A and E (Figure 5.8 and Table 5.1), the mean pressure was derived making use of the simplification presented in Equation 4.4, as at these positions there was knowledge of the velocity field (which is required for this method).

At the other positions, G, H, I & J, there was no knowledge of the velocity field, and so an even more simplistic approach was required. As before (Section 2.5), the observation was made that the pressure was more constant along horizontal lines, than along vertical lines, and so to find a mean pressure over a cross section the following algorithm was applied. Firstly along horizontal lines the arithmetic mean pressure was taken, then out of those, again the arithmetic mean was taken, this was assumed to be the mean pressure in the cross section.

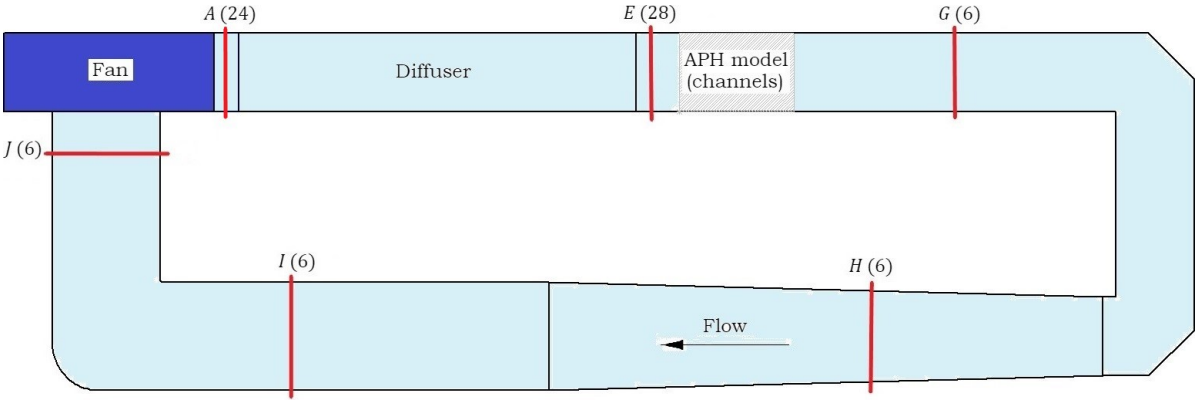

Figure 5.23: Positions throughout the windtunnel where wall pressures were recorded, the numbers indicate at how many points per cross section, a measurement was taken. The fan is on the top left, the stack of plates is indicated by the area shaded in grey.

5.4.1. Results: Positions A, E and the return duct

For positions A and E (again, see Figure 5.8 and Table 5.1), the wall pressures recorded are shown in Figure 5.24. In red the wall of the channel is shown, the blue arrows give the pressure. A vector pointing outward represents a pressure larger than that of the surroundings, a inwardly pointing vector represent a negative relative pressure.

The mean pressures were found to be -75.4 and $12.1\,Pa$ at positions A and E respectively. The pressure recovery is thus $\Delta p = 87.5\,Pa$. The wall pressures measured throughout the return duct are presented in Table 5.2 and Figure 5.25, together with the results found at A and E.

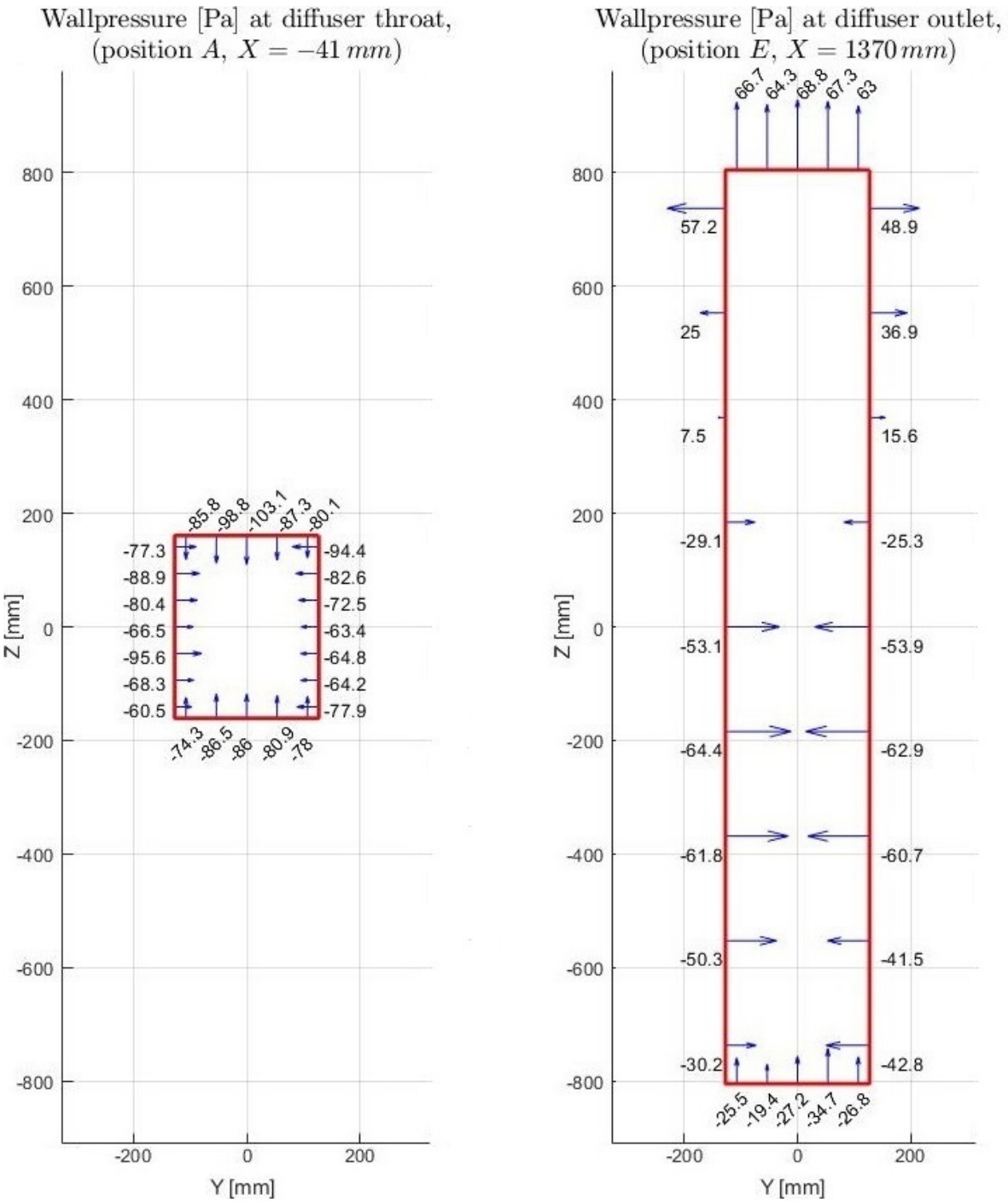

Figure 5.24: The wall pressures measured in cross sections of the diffuser throat (position A) and the diffuser outlet (position E). The mean pressure for the diffuser throat was found to be $-75.4\,Pa$, for the diffuser it was found to be $12.1\,Pa$.

Position	Pressure [Pa]
A	-75.4
E	12.1
G	-55.3
H	-61.2
I	-116.6
J	-138.1

Table 5.2: Wall pressures at the locations specified in Figure 5.23.

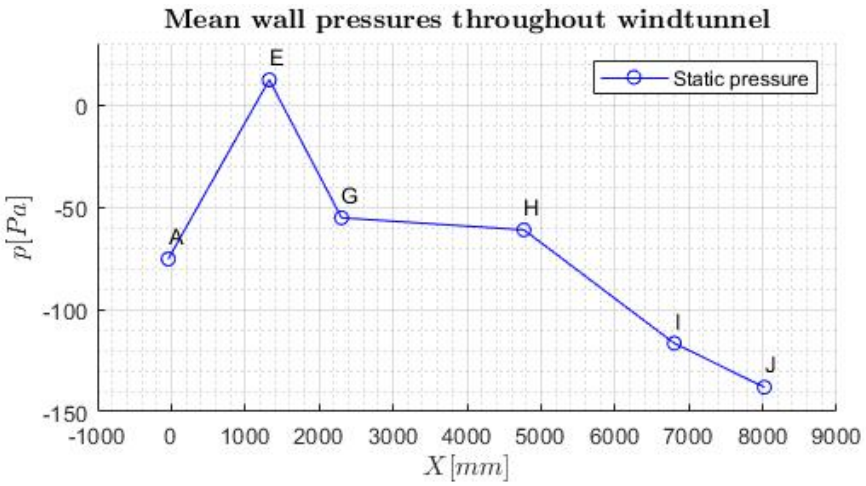

Figure 5.25: Mean wall pressures over the axis of the windtunnel, the positions of the specific measurement is denoted above each data point. The positions are specified in Figure 5.23.

6

Analysis

In this chapter, the performance of the diffuser will be quantified using the theory explained in Chapter 2, making use of the results presented in Chapter 5.

6.1. Current system performance

6.1.1. Performance parameters

In Chapter 2, four performance parameters were defined; the static pressure recovery coefficient, the static pressure recovery efficiency, the dissipation in the diffuser and the kinetic energy flux factor at the diffuser outlet. All these were derived from the data gathered. In the following sections these parameters will be presented.

Static pressure recovery coefficient

The static pressure recovery coefficient was found using Equation 4.3 and the approximation of Equation 4.4, this resulted in $C_p = 0.46$. This is slightly higher than expected, from literature (Blevins, 1984) there was the rough estimate of 0.35. As said in Section 3.2, this estimate applies to a diffuser with free discharge, a uniform flow at the inlet, and a boundary layer of $2\delta_1/W_1 = 0.015$.

Static pressure recovery efficiency

The static pressure recovery efficiency of the diffuser was found to be $\eta = 48\%$, based on the definition of Equation 2.6. Again, this is slightly higher than expected. Based on the rough estimate for C_p given in Blevins (1984), it was expected that $\eta = 36\,\%$.

Kinetic energy flux factor at diffuser outlet

Numerical integration was used to solve for the kinetic energy flux factor, see Equation 2.4. It was found that $\alpha_2 = 4.53$. (The kinetic energy flux factor at the diffuser throat was found to be $\alpha_1 = 1.64$.)

Time rate of energy dissipation in the diffuser

The discrete equations of 4.5 through 4.7b were used to solve for the time rate of energy dissipation in the diffuser[1]. It was found that energy is dissipated at a rate of $\dot{W}_{dissipation} = 95.3\,W$.

Here, the dissipation of energy, has contributions of kinetic energy and pressure work. Respectively these terms were 195.0 and -99.8, where a positive number indicates a decrease in flow of energy between the diffuser throat and diffuser outlet, for the specific type of energy. In other words, over the diffuser an energy conversion process occurs, from kinetic energy into pressure energy.

[1] In equations 4.5 through 4.7b, for the surface integral at A_1 (diffuser throat) the data measured at measurement position A was used, see Figure 5.8. Similarly, for the surface integral evaluated at A_2 (outlet) the data measured at position E was used.

An important remark is that the kinetic energy terms are derived from the mean velocity field. The energy related to turbulent fluctuations is thus disregarded. The nonlinear relation between velocity and kinetic energy causes the actual time averaged flow of kinetic energy to be higher than that predicted based on the mean velocity. What effect this will have on the dissipation that was found, cannot be said without having a description of the velocity field in space ánd time.

Some analysis was performed to estimate the error introduced into the kinetic energy term, by deriving it from a mean velocity field. See Appendix A.2: For a hypothetical flow, that has only the dimension of time, the average flow of kinetic energy was derived analytically twice: Firstly based on the mean velocity field, and secondly, based on the time dependent velocity. Comparing the two gave an estimate for the error.

The flow studied was $u(t) = \bar{u} \cdot (1 + B\,sin(t))$. It was found that for $B = 0.2$, the above mentioned error to the calculated average flow of kinetic energy will be $-6\,\%$. The $B = 0.2$ was chosen arbitrarily and acts as an example. The result of the analysis in Appendix A.2, cannot directly be used to predict an error in the kinetic energy derived from measurements, as the flow in the diffuser does not correspond to the function of $u(t)$. For future work however, an estimate for B can be derived from LDA measurements as LDA can, at high frequency, measure the actual velocity. Furthermore both the velocity and turbulence level are not constant over their cross sections, futher complicating this.

6.1.2. Flow rate

Flow rates were found for all the cross sections that were measured via numerical integration of the velocity field. By continuity all these should be the same. An overview of the results is given in Table 6.1. Per position the flow rate found is given, for position A the flow rates derived from both the LDA and PIV measurements are shown. For positions A and E, where PIV was used, in a volume the velocity field was measured. This volume consists of a finite number (depending on the resolution of the measurement) of cross sections. In each of these cross sections, a flow rate is defined. So, effectively in these volumes several flow rates were measured. By continuity these should all be equal, in practice they are not. For these sets of flow rates, the mean was taken on and shown in Table 6.1, the standard deviation is given as well.

Through all measurements conducted, a mean flow rate of $Q = 1.14\,m^3/s$ was found. This corresponds to a Reynolds number of $Re = 2.7 \times 10^5$. This number is based on the mean velocity ($\bar{u}_1 = Q/A_1$) at the throat, and the hydraulic diameter in the throat.

Position	Q [m^s/s]	σ [m^s/s]	Deviation from mean [%]
A (PIV)	1.14	0.0041	-0.1
A (LDA)	1.17		$+2.5$
B	1.14		-0.1
C	1.17	0.0287	$+2.5$
D	1.07		-6.3
E	1.16		$+1.6$
Mean	1.14		

Table 6.1: The volume flow rates derived from the measurements results. For the PIV measurements, several flow rates were found as the PIV measurements were not in a single cross section, for these the mean is depicted including the standard deviation over the number of cross sections. On the right the deviation from the mean is given, where the mean is simply the arithmetic mean out of all the flow rates given in the middle column.

6.1.3. A macroscopic description of the measurement results

Literature suggested that the diffuser would operate in bistable steady stall regime / fully developed two-dimensional stall regime, see Figure 2.5. This means that after startup of the fan, the jet will randomly stick to either one of the diverging walls. After that, the position of the jet will remain fixed. Literature suggests that it is more or less random to which wall the jet will stick (Kibicho and Sayers, 2008). This was not the case for the diffuser tested.

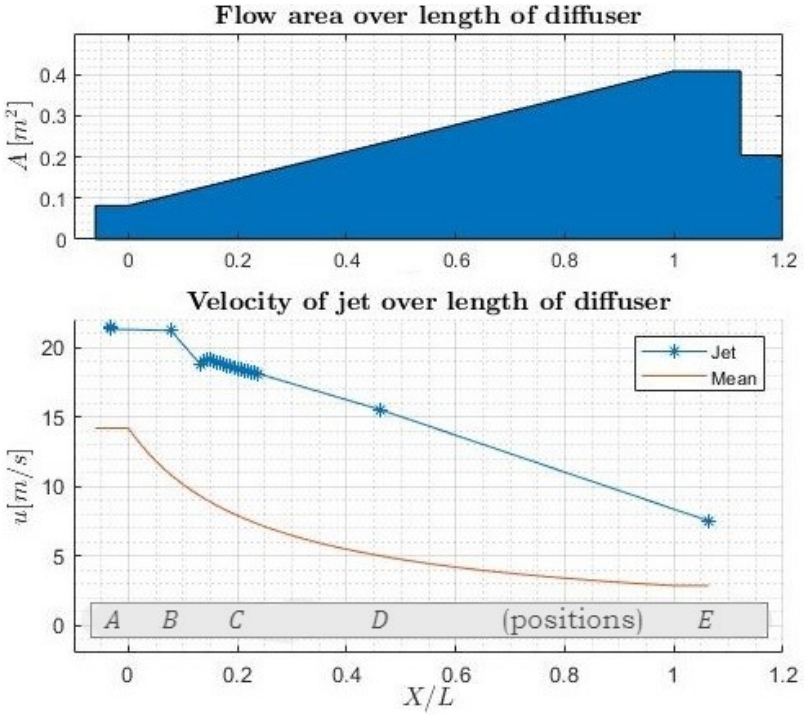

Figure 6.1: The top graph shows flow area of the channel over its length. In the lower graph the behavior of the jet over the length of the diffuser is shown. Here, the velocity of the jet was defined as the top 10% of all velocity data points (per cross section), the X-dimension is normalized with the diffuser centerline length, so at the diffuser throat, $X/L = 0$, at the diffuser outlet $X/L = 1$. The red line indicates how in the ideal case the velocity would be, based on the simple $\bar{u} = Q/A(X)$. In the grey bar, the positions of the corresponding data points are given, referring to Figure 5.8 and Table 5.1.

The jet would at all times be at the same position. It most likely has to do with the non-uniform velocity profile at the diffuser throat. It overcomes the effect of some perturbation that determines the position of the jet, in case of a uniform flow.

By visual inspection, at the diffuser throat ($40\,mm$ upstream of it, to be more exact) the jet covers approximately two thirds of the cross section, see Figures 5.10a and 5.10b. Looking at the contour plots of $\bar{u}$ (Figures 5.10a, 5.10b, B.1a, B.2a, B.6a & 5.21a), it can be seen that with this slowing down, the area of the jet increases, which is as expected.

With Figure 5.4 an interpretation was given of how the velocity field looks like, based on the visualization with plastic strips in the flow. The results from the quantitative measurements support that underneath the jet a large recirculation zone exists.

In Figure 5.22 it can be seen that there is some backflow in the channels downstream of the diffuser. In order to prevent this backflow, the stack of plates should give a higher resistance, or some other mechanism could be used to create a more uniform flow to the upstream side of the plates (air preheater model).

Jet velocity

In Figure 6.1 it can be seen that the jet does slow down. At the diffuser outlet, position E, the jet does still have a velocity of $u_{jet} = 2.7 \times u_{mean}$. The jet will impinge on the inlet of the air preheater, leading to high losses. Furthermore, the high velocity jet will locally decrease the metal temperature of the heat exchanger. This local cooling can lead to corrosion.

Distribution of mass flow over height of plate stack

See Figure 6.2, in the left graph the cummulative fraction of mass flowing above height Z, is plotted over the height of the air preheater model (position F, defined in Figure 5.8 & Table 5.1). It can be seen how uneven the distribution is; the top half of the plate stack accounts for $84\,\%$ of the total mass flow. In the right graph the velocity profile is given. The performance of the heat exchanger will be affected adversely, by this uneven distribution of mass flow.

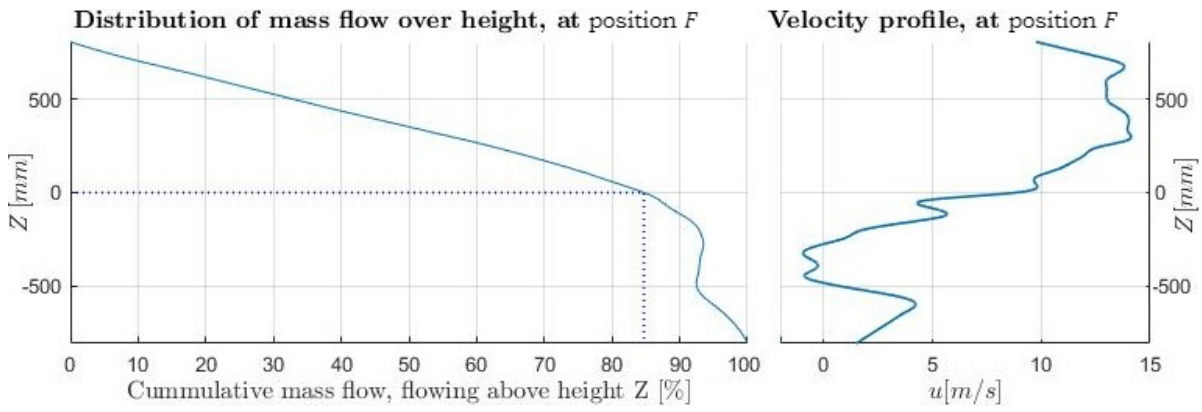

Figure 6.2: In the left graph the cummulative mass fraction that flows above height Z is plotted. The graph applies to position F, i.e. the flow in the plate stack, see Figure 5.8 and Table 5.1. Note that for the current system, $84\,\%$ of the total mass flow, flows through the top half of the plate stack. The right graph gives the velocity profile at the same position.

Similarity: Freely blowing fan and fan with ducting

Looking at the results presented in Section 5.3.2, it stands out that the velocity fields of the fan with and without ducting are very alike. See Figures 5.10a & 5.10b for the results with the ducting, and 5.16a & 5.16b for those without. For now this applies only to this specific fan. However if at some point it is clear that the actual shape (so, disregarding other parameters such as pressure and the velocities themselves) of the velocity field at the fan outlet, is insensitive to the downstream conditions, measuring a fan that blows freely into space can provide useful information.

6.1.4. A comparison: fan spec sheet vs. measurements

The hydraulic power of the fan was calculated in the same way as the time rate of energy dissipated in the diffuser, see Equations 2.7a through 2.7c. The power found consisted of a rate of pressure work term, and a kinetic energy term (upstream of the fan, $v\,\&\,w$ were unknown and assumed to be zero). The power was found to be $P_{fan} = 241.2\,W$. The contributions of the kinetic energy, and pressure terms were $169.8\,W$ and $71.4\,W$ respectively.

Below a comparison will be made between the measured fan performance, and the specifications of the fan. The fans hydraulic power of $241.2\,W$ that was measured, is based on the difference in flow of kinetic energy between the fan in- & outlet, and the rate of pressure work done by the fan. The hydraulic fan power as provided by the manufacturer (Casals Ventilation, 2018), has a different definition: It is based on the flow of kinetic energy through its outlet (as opposed to the difference between in- & outlet), and the rate of pressure work done by the fan. Using this definition it was found that $P_{fan} = 301.1\,W$, at a flow rate of $Q = 1.14\,m/s$. According to the manufacturer at his flow rate the power output of the fan should be $411.2\,W$ as can (more or less) be seen in the fan curve (Figure 3.3).

Furthermore, looking at the separate terms the hydraulic fan powers (the one predicted, and the one measured) are built up out of it can be seen that the distribution of energy between kinetic energy[2], and energy of pressure, is very much different for the two cases, see Table 6.2:

This difference in contributions of the two terms has to do with the method used for rating the fans. According to the Air Movement and Control Association (AMCA, 2007), centrifugal fans are usually tested with an outlet duct of certain length, the pressure and velocity are then measured some distance downstream of the fan. This distance is in the range of 10 hydraulic diameters (of fan outlet). The goal of that is to measure a more developed velocity field, that better characterizes the fan. Over the length of this duct, an energy conversion process occurs: The non-uniform velocity profile at the fan outlet, becomes more uniform over the length of the duct, and as said in Chapter 2, this leads to static pressure recovery.

[2]Similar to the dissipation in the diffuser (Section 6.1.1), the contribution of kinetic energy is slightly off as only the mean velocity field is considered, recall that 'an amplitude for the fluctuation of $(B \cdot \overline{u}) = 0.2$ will lead to an underestimation of approximately 6%'.

Contribution to fan power	Measured [W]	Fan specs [W]
$\dot{W}_{pressure}$	71.4	339.2
$\dot{E}_{kin}$	229.7	72.0
P_{fan}	301.1	411.2

Table 6.2: The fan power as measured, and the fan power as expected from the fan specifications, at the measured flow rate of $Q = 1.14\,m^3/s$. Note that $\dot{E}_{kin}$ is the flow of kinetic energy downstream of the fan (not the difference in flow of kinetic energy over the fan).

This difference in position of where the measurements were taken, explains the difference in the relative size of the pressure & kinetic energy contributions, to the fan power.

Furthermore, to quote AMCA (AMCA, 2007, p. 3); 'In any installation where uniform airflow conditions do not exist, the fans performance will be measurably reduced', and (AMCA, 2007, p. 29): 'in most cases it is not practical for the fan manufacturer to supply this duct[3] as part of the fan, but rated performance will not be achieved unless a comparable duct is included in the system design'. To conclude it is likely that this discrepancy in predicted and measured performance has to do with the different methods for the fan rating, and the methods used in this work. Still, when looking at the total energy that is added to the flow, the discrepancy is too large and cannot be caused by a too short length of straight duct downstream of the fan.

An explanation for the low measured fan power might be that the geometry of the 90° turn upstream of the fan is such that an unfavorable flow enters the fan (even though the turn has guiding vanes and rounded inner and outer edges, see Figure 3.9). Still in the same AMCA document, System Effect curves are described. In these the losses related to a straight duct downstream of the fan, that is shorter than the 100% effective duct length (≈ 4.5 for this case) are quantified. Using Figures 7.1 (p. 25) and 8.3 (p. 31) (AMCA, 2007), it was found that 200 to $250\,Pa$ (based on the mean velocity of $13.9\,m/s$) are lost due to this mismatch. This estimate is of a correct order of magnitude and so the geometry of ducting upstream of the fan is a plausible cause for the poor fan performance.

To conclude this section, it must be said that after comparing the measured fan power, to that predicted based on the fan curve, it is clear the fan is not performing well. This however gets worse, when it is considered that based on observation, an electrical power of $630\,W$ flows into the fan. An overall efficiency of the fan can be defined as the power added to the flow ($241.2\,W$) normalized with its electrical power input, this gives a fan efficiency of 38 %.

6.1.5. Pressure over windtunnel

With Figure 5.25, the results of wall pressure measurements have already been presented. For the present section these will be combined with data of the velocity, as to gain an understanding of the stagnation pressure.

At the diffuser throat and the diffuser outlet (indicated with the red dots in Figure 6.3) the dynamic and static pressure terms are mass flow rate weighted averages (Equation 6.1, the simplification of Equation 4.4 was also used). At other positions, the dynamic and static pressures will be based on more simplified, one dimensional formulas (Equation 6.2).

$$p_{tot} = \frac{1}{Q}\int_A pu\,\mathrm{d}A + \frac{1}{2}\rho\bar{u}^2\alpha \tag{6.1}$$

$$p_{tot} = p + \frac{1}{2}\rho\overline{u}^2 \text{ (where: } \overline{u} = Q/A) \tag{6.2}$$

In Figure 6.3 the results are shown; the horizontal axis denotes the distance towards the origin, along the axis of the channel (as if it were straight). The top graph shows the area of the cross sections along the channel, which as explained, for all points except the first two, was used to derive the dynamic pressure. In the lower graph, the dynamic pressure, static pressure and stagnation pressures are plotted.

[3]The straight duct that has the length of approximately 10 hydraulic diameters.

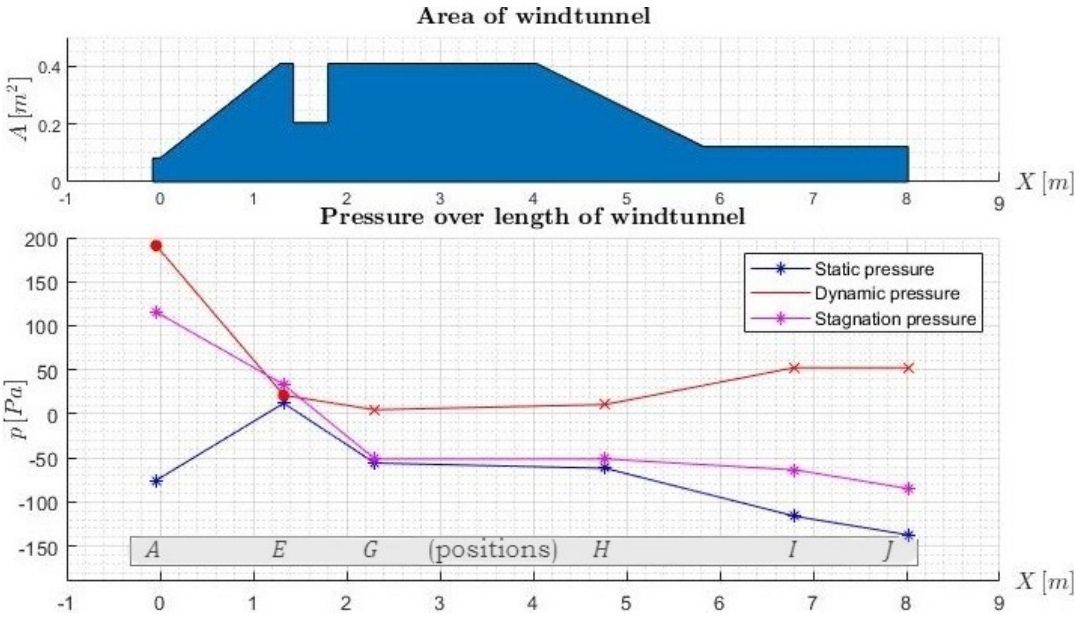

Figure 6.3: Above the cross sectional area of the channel is plotted, as function of X (where X is the coordinate in the streamwise direction, as if the system was along a straight line). Below, the pressures are plotted, also as function of this X. In the grey bar in the middle, it is indicated to what position along the windtunnel, the point in the graph below corresponds, the positions are explained in Figure 5.23. For the dynamic pressure at locations A and E, the method of Equation 6.1 was used, for the remaining locations, that of 6.2 was used.

Below for every interval in the graph of Figure 6.3, the behavior of the static, dynamic and stagnation pressure will be elaborated on:

- A to E: Over the diffuser, the dynamic pressure reduces and the static pressure increases. As said before, this occurs at low efficiency which can also be seen from the large decrease in stagnation pressure.
- E to G: This section includes the stack of plates which explains the drop in static pressure. At both positions the area of the cross section is the same, however the average dynamic pressure is higher at position E, is there, there is a non-uniform velocity profile.
- G to H: This is the 180° turn, and approximately half the nozzle in the return duct (see the upper graph). Very low losses occur in this section.
- H to I: This section includes the second part of the nozzle and a straight duct. As compared to the part of the windtunnel to the upstream side, high losses occur here. Most likely this is caused by a vena contracta at the end of the nozzle.
- I to J: This last part of ducting includes the 90° turn, although this turn has been optimized with guiding vanes and rounded edges, a high pressure drop was found over this short piece of ducting. This is expected, as locally the cross section of the channel is small, and thus the flow velocity is high.

6.2. Summary of performance

In the current section a brief overview will be given of the performance as measured, for the conditions set by the fan and the geometry of the channel. The fan used was a $750\,W$ centrifugal fan with a one-sided inlet, it was observed that $630\,W$ of electrical power flows into the fan. The diffuser has an area ratio of $A_2/A_1 = 5$, an inlet aspect ratio of $W_1/b = 1.27$ end a length of $L/W_1 = 4$. The flow pattern observed in the diffuser is that of 'fully developed two-dimensional stall', which is as predicted in Figure 2.5. The jet would at all times lay against the top surface of the diffuser. In Table 6.3, all relevant parameters are shown.

Flow rate	Symbol	Value
Volume flow rate	Q	$1.14\,m^3/s$
Reynolds number	Re	2.7×10^5
Static pressure recovery coeff.	C_p	0.46
Static pressure recovery efficiency	η	$48\,\%$
Diffuser outlet kinetic energy flux factor	α_2	4.53
Mass flow through top half of channels		$84\,\%$
Dissipation in diffuser	$\dot{W}_{dissipation}$	$95.3\,W$
Hydraulic fan power	P_{fan}	$241.2\,W$

Table 6.3: Overview of the performance of the fan/diffuser system. The hydraulic fan power, is the rate of energy transferred to the flow.

7

Conclusion & future work

This final chapter will firstly give a summary of previous chapters, and it will give some discussion and recommendations for future work.

7.1. Summary

7.1.1. Motivation

In heavy duty industry, air preheaters are used to increase the thermal efficiency of fired heaters. These air preheaters have ambient air on their cold side. The air is fed through by a centrifugal fan, placed on the upstream side of the heat exchanger, out of sheer necessity these two are often connected with a widening transition duct of unfavorable geometry. A large area ratio combined with a short length of the duct, causes high losses when the air flows through this large angle diffuser.

Diffusers in general have been studied for many years, much information is available on them. The diffusers studied were generally subject to a uniform velocity profile. The flow emerging from centrifugal fans, is not uniform at all, this poses a problem in predicting the performance of the system consisting of the fan, diffuser and heat exchanger. Besides that poor predictability, the performance itself of these systems is poor. This gave rise to a need for research on systems built up out of a centrifugal fan, a large angle diffuser and some resistance downstream of the diffuser. It was decided that the starting point for the research had to be an experimental approach, as CFD results for diffusers are not reliable, ánd for CFD adequate knowledge of the boundary conditions must be available, these of course have to be determined empirically. A windtunnel with a scaled down diffuser was built to study the flow in large angle diffusers and to eventually come up with efficient solutions. This last part is beyond the scope of this work.

7.1.2. Background

As a fluid flows through a diffuser, the average velocity goes down as the ducts cross section increases. With that, the static pressure should increase. In other words, an energy conversion process occurs; kinetic energy is converted into energy of pressure.

Inefficient flow through large angle diffusers is caused by flow separation, which in its turn is caused by the adverse pressure gradient inherent to a flow that is slowing down. If flow separation occurs, effectively the duct does not widen, and although the mean flow velocity (over a cross section) does decrease over the diffuser length, little kinetic energy is converted into fluid pressure.

Four performance parameters were chosen, with which to describe the flow in the system. The static pressure recovery coefficient, C_p, and the static pressure recovery efficiency (η) were used to characterize the performance. Respectively they describe how effectively, and how efficiently kinetic energy is converted into pressure. The rate of dissipation of energy in the diffuser, $\dot{W}_{viscous}$, is another performance parameter chosen, and lastly there is the kinetic energy flux factor at the diffuser outlet, α_2. It is a measure for how uniformly the

mass flow is distributed over the cross section, which very much influences the performance of the downstream equipment. In this work the C_p was calculated slightly differently than traditionally in literature. The renewed method better copes with flow non-uniformities as compared to the traditional method, that is based on a one-dimensional expression for C_p.

Existing solutions to improve the flow in large angle diffusers often aim to spread the flow by offering extra resistance. Most commonly this spreading action is done by inserting perforated plates into the flow. These methods are effective in creating a more uniform flow at the diffuser outlet, however it goes without saying that improving the flow by adding resistance is by no means an elegant solution. Also literature suggests that the outcome is very sensitive to the placement and porosity of the resistance used.

A more efficient way to spread the flow is to use guiding vanes near the diffuser throat. With longer vanes, the duct is split into multiple *subdiffusers* that have a more favorable geometry, however frictional losses will then increase. With shorter guiding vanes, these frictional losses will not increase significantly, however with these it will be harder to control the flow.

7.1.3. Setup

A diffuser test platform was built with which diffusers of various geometries can be studied as the measurement section can be replaced easily. A single-inlet centrifugal fan is used to drive the flow through the windtunnel. A straight transparent section of length $78\,mm$ was in between the fan and the diffuser, this allowed for measuring the velocity field at the inlet of the diffuser, which is the position where it is most important to have accurate knowledge of the flow field.

For this work, one diffuser has been studied. It had an area ratio of $A_2/A_1 = 5$, a length of $N/W_1 = 4$ and a throat aspect ratio of $W_1/b = 1.27$. Based on the geometry of the diffuser it is expected that the flow in the diffuser would have 'bistable steady stall', or 'fully developed two dimensional stall'. Downstream of the diffuser was a short straight section followed by a stack of plates that simulated the resistance offered by what in industry would be an air preheater (no heat transfer would occur in it). The geometry was such that in between the plates channels existed with a thickness equal to that of the plates, i.e. $9\,mm$. The width and length of the channels were $254\,mm$ and $370\,mm$ respectively. These channels had optical access making it possible to measure the distribution of mass flow over the channel its height, at the exact position where it is most important to know this distribution, namely in the air preheater model. All ducts downstream of the air preheater model were constructed from wood, and gave no optical access for velocity measurements. The overall length of the windtunnel was approximately $4\,m$, the height and width were $1.7\,m$ and $1.2\,m$. See Figure 7.1 for a 3D render of the system.

7.1.4. Measurement techniques

To analyze the system, knowledge of the velocity field and pressures was required. Velocities were measured with LDA and PIV, the two methods side by side could act as validation. The results showed good similarity. A $500\,mW$ 'Dantec Dynamics' LDA system was used for point wise velocity measurements. With the PIV system used (a 'Litron Lasers' YAG laser & 'Dantec Dynamics' camera) it was possible to measure the two in-plane mean velocity components. A method was constructed with which it was possible to measure all three mean velocity components in a volume, with the PIV system at hand.

Regarding the pressure; only wall pressure measurements were taken. For measuring pressures in the bulk of the flow, a pitot tube would have to be aligned with the local direction of the flow. This would have been highly impractical, as the flow is turbulent and also the mean flow direction depends on the position in the channel.

7.1.5. Results

From preliminary tests, where flexible strips showed the local direction of the flow, it was clear that (indeed) a jet exists, and that it lays against the top surface of the diffuser. Below it, a large recirculation zone exists. The laser optical measurements backed up the results of the visualization with flexible strips, furthermore they gave quantitative information of the

flow.

The flow rate was found to be $Q = 1.14\,m^3/s$, the kinetic energy flux factor at the diffuser outlet was $\alpha_2 = 4.53$. For the rate of dissipation, and the pressure recovery effectiveness and efficiency the results from wall pressure measurements were used as well. These were $\dot{W}_{dissipation} = 95.3\,W$, $C_p = 0.46$ and $\eta = 48\,\%$.

For the fan, the rate of energy transferred to the flow could be estimated as the conditions downstream of it were measured, for the upstream conditions a flat velocity profile of $\bar{u} = Q/A$ was assumed. The relevant pressures were measured. It was found that an energy rate of $241.2\,W$ is added to the flow, this includes kinetic energy, pressure terms, and that of changes in elevation. A comparison with the specifications of the fan did raise some questions. Firstly it is claimed that the fan has a power of $750\,W$. Whichever definition for power is used there, it is clear that the fan is performing poorly considering that roughly a third of the claimed fan power effectively is transferred to the flow. It was measured that $630\,W$ of electric power enters the fan, and with that the image painted is slightly better. Still the fan operating very inefficiently, which might have to do with the nature of the flow entering the fan.

To conclude this section, an interesting observation was that no less then 84% of the total mass flow, flows through the top half of the channels in the plate stack. The flow just upstream of the air preheater model, the still has a jet velocity of $u_{jet} = 2.7 \times u_{mean}$, where u_{mean} is the mean velocity in the cross section. This high velocity jet impinges on the plates.

7.2. Conclusion

The main goal of this research was to gain an understanding of the flow in large angle diffusers that act as a transition duct between a centrifugal fan, and an air preheater.

The need for this research arose from two factors: Firstly, these systems have been found to perform poorly in industry. Secondly, previous work in the field of diffuser flow mostly focused on diffusers that were subject to a uniform inlet velocity profile. Diffusers downstream of centrifugal fan are not subject to a uniform inlet velocity profile, and so effectively there was a lack of previous work on this fan-diffuser system.

The tool used in this research was a testing platform. It was designed and built specifically for this research. This testing platform is a closed loop windtunnel. It has a diffuser shaped transparent measurement section that can easily be replaced for one of another geometry. With this flexible setup, multiple diffusers can be characterized in a single windtunnel without having to build a windtunnel specifically for each diffuser that is to be studied. Before building a diffuser in industry, a scaled down model can be fitted to the windtunnel. This scale model can then be used to study that specific shape, with the goal of optimizing the flow in it.

Four easy to use scalars were set, these were used to quantify the performance of any diffuser. (1) The static pressure recovery coefficient, (2) the static pressure recovery efficiency, (3) the kinetic energy flux factor at the diffuser outlet and (4) the time rate of energy dissipation in the diffuser were used for this. All of these could easily be measured in the measurement section. They must be seen as output variables, any intended optimization to a diffuser should be observed in a change in at least one of these four variables. They cannot act as indicators on how the geometry should be modified for an optimization, for this the velocity field as a whole should be used.

So far, one diffuser has been fitted to the windtunnel. In multiple cross sections the flow rate was measured. The flow rates found were in good approximation to one another, to some extend this indicates that the testing platform is working well.

The diffuser would, according to literature that focuses on diffusers with a uniform inlet velocity field, operate in the bistable steady stall regime (based on its geometry). Literature suggested that in this flow regime, the jet can stick to either one of the diverging walls (Kibicho and Sayers, 2008). Once the jet sticks to a wall, its position would remain fixed. This behaviour was not observed. At all times the jet would remain attached to the top wall.

An explanation for this could be: For a uniform inlet flow, any of many perturbations can cause the flow to separate from one, and attach to another wall. To the observer, this comes across as a random process. Now however, if the incoming flow is non-uniform the effect of

perturbations is overcome. There is deterministic relation between the nature of the velocity field at the diffuser throat, and the position of the jet. For now, the optimization of the flow in the diffuser that was tested is regarded as future work.

7.3. Future work

There are three categories on which future work in this research can focus. Firstly, there are some improvements that can be made on the testing platform. These have the goal of requiring data more easily. Secondly, work can be done on fan-diffuser systems in the context of the fired heater configuration shown in Figures 1.1 & 2.1. Lastly, future work can focus on the flow in the diffuser that was characterized.

7.3.1. Testing platform: Differential pressure as indicator for flow rate

In order to asses future improvements to the diffuser, it is important to observe any change in volume flow rate that might be the result. Before, this volume flow rate was found via numerical integration of the velocity field in some cross section. This is rather time consuming, and so to be able to more quickly see changes in the volume flow rate, another method is proposed. Over some parts of the windtunnel, the pressure drop has good correlation with the flow rate. The part best suited is that between approximately halfway the nozzle in the return duct (to eliminate the effect of the second turn in the windtunnel), and some distance downstream of that, see Figure 7.1. In the nozzle a uniform flow is expected, and it was observed that in the nozzle, the pressure is quite constant over the cross-section. At this moment, only for one condition (in terms of pressure drop and flow rate) measurements have been done. For this reason the proposed method of monitoring the volume flow rate via a differential pressure, can only be used for qualitative purposes.

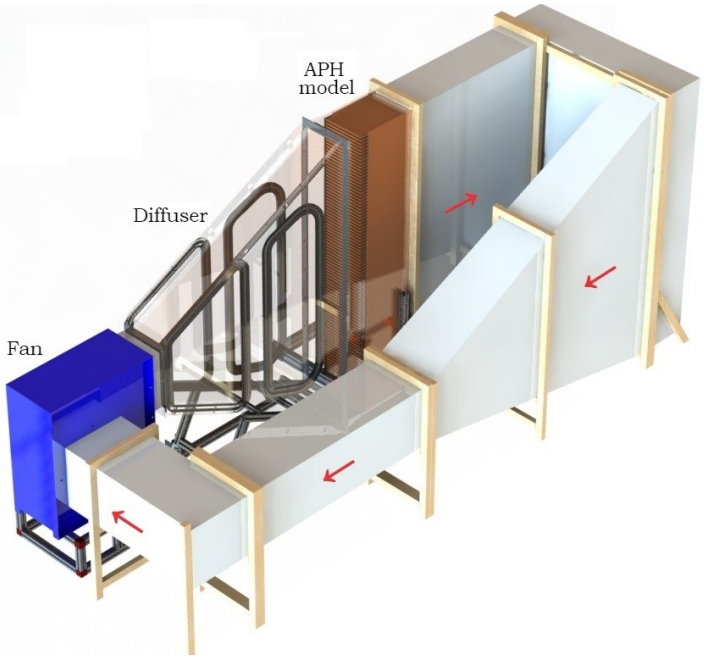

Figure 7.1: Impression of the windtunnel built. The red arrows indicate the direction of the flow.

7.3.2. Fan-diffuser system in the context of a fired heater with an air preheater

Induced draft

The essence of the problem in the fan-diffuser system, is the diffuser. It can however be eliminated, the centrifugal fan that drives the flow could be placed downstream of the air preheater. Some practical consideration on this: The fan will be exposed to high ($615\,K$) temperatures. The fan will have to be placed high above ground level: In Figure 2.1 a schematic

representation of an air preheater is given. Here it can be seen that the cold side air exits the air preheater on the high side of the unit. With forced draft, as shown in the figure, the fan will be down low. With induced draft the fan will have have to be several meters above the ground. The weight and vibrations of the fan can then be problematic.

7.3.3. Proposed improvements to the fluid mechanics of a large angle diffuser

As a starting point for future work on the flow in the diffuser that was characterized, it is recommended to focus on short guiding vanes, see Section 2.6. These should be placed near the diffuser throat. Their goal is to split up the single jet that was found, into several jets whose orientation can be controlled with the angle of the guiding vanes. Good knowledge of the mean velocity field is present, this can be used to determine optimum positions & orientation for the guiding vanes. With guiding vanes near the diffuser throat, on large scale good uniformity of the flow can be achieved at the diffuser outlet. Ideally the jets will slow down and spread out evenly of the cross section, such that local non-uniformities disappear as well. It however is likely that the several jets will still exist at the diffuser outlet, then, a perforated plate could be used. This will, at the cost of a high pressure drop, even out the small scale non-uniformities.

A

Appendix A

A.1. Hydraulic power / time rate of dissipation

Departing from the first law of thermodynamics combined with the Reynolds transport theorem, gives:

$$\frac{\mathrm{d}E}{\mathrm{d}t} = \dot{Q} - \dot{W} = \oiint \epsilon \rho \overline{u} \cdot \overline{n} \, \mathrm{d}A \tag{A.1a}$$

where $\dot{Q} = 0$, as an adiabatic system is assumed. The terms $\overline{u}$ and $\overline{n}$ respectively denote the velocity vector, and the outward pointing normal unit vector. Furthermore, ϵ represents the energy per unit of mass in the flow, here, static pressure is included in it:

$$\epsilon = \frac{\mathrm{d}E}{\mathrm{d}m} = \frac{1}{2}u^2 + \frac{1}{2}v^2 + \frac{1}{2}w^2 + p/\rho \tag{A.1b}$$

Combining the above equations, and rewriting for a system with one inlet (A_1) and one outlet (A_2), gives:

$$\dot{W} = \int_{A_1} \frac{1}{2}\rho u\left(u^2 + v^2 \ + w^2 + p/\rho\right) \mathrm{d}A - \int_{A_2} \frac{1}{2}\rho u\left(u^2 + v^2 \ + w^2 + p/\rho\right) \mathrm{d}A \tag{A.1c}$$

In the above equation the separate terms of kinetic energy and pressure work can be recognized, splitting up gives:

$$\dot{W} = \Delta\dot{E}_{kin} + \dot{W}_{pressure} \tag{A.1d}$$

$$\Delta\dot{E}_{kin} = \int_{A_1} \frac{1}{2}\rho u\left(u^2 + v^2 + w^2\right) \mathrm{d}A - \int_{A_2} \frac{1}{2}\rho u\left(u^2 + v^2 + w^2\right) \mathrm{d}A \tag{A.1e}$$

$$\dot{W}_{pressure} = \int_{A_1} pu \, \mathrm{d}A - \int_{A_2} pu \, \mathrm{d}A \tag{A.1f}$$

The above three equations were used in this work to find both the time rate of energy dissipation in the diffuser, or the hydraulic power of the fan.

A.2. Error estimation for flow of kinetic energy

In this work the energy dissipation in the diffuser and the hydraulic fan power were calculated. The terms of kinetic energy were derived from the measured mean velocity field. This introduces an error in the kinetic energy term. When using the actual, time dependent, velocity field, the calculated flow of kinetic energy will be higher. For some hypothetical flow $u(t)$, which is only a function of time, it was investigated what effect it has when the flow of kinetic energy is derived from the mean velocity field.

$$\dot{E}_{kin} = \int \frac{1}{2}\rho u^3 \,\mathrm{d}A \tag{A.2a}$$

$$u(t) = \bar{u} \cdot (1 + B\,sin(t)) \tag{A.2b}$$

The average flow of kinetic energy, based on the mean velocity $\bar{u}$ is:

$$\dot{E}_{kin}(\bar{u}) = \int \frac{1}{2}\rho \bar{u}^3 \,\mathrm{d}A = A \cdot \frac{1}{2}\rho \bar{u}^3 \tag{A.2c}$$

The average flow of kinetic energy, based on the actual velocity $u(t)$ (when $t \to \infty$):

$$\dot{E}_{kin}(u(t)) = \lim_{t\to\infty} \frac{1}{t}\left(\int_0^t \int_A \frac{1}{2}\rho(u(t))^3 \,\mathrm{d}A\,\mathrm{d}t\right) = \lim_{t\to\infty} \frac{1}{t}\left(A \cdot \int_0^t \frac{1}{2}\rho(u(t))^3 \,\mathrm{d}t\right) \tag{A.2d}$$

Substituting the expression for $u(t)$ into the above equation, gives:

$$\dot{E}_{kin}(u(t)) = \lim_{t\to\infty} \frac{1}{t}\left(\int_0^t \int_A \frac{1}{2}\rho(u(t))^3 \,\mathrm{d}A\,\mathrm{d}t\right) = \lim_{t\to\infty} \frac{1}{t}\left(A \cdot \int_0^t \frac{1}{2}\rho(\bar{u} \cdot (1 + B\,sin(t)))^3 \,\mathrm{d}t\right) \tag{A.2e}$$

and rewriting gives:

$$\dot{E}_{kin}(u(t)) = A \cdot \frac{1}{2}\rho \bar{u}^3 (1 + \frac{3}{2}B^2) \tag{A.2f}$$

To conclude, the error made when a flow of kinetic energy is based on the mean velocity field is (for velocity $u(t)$):

$$1 - \frac{\dot{E}_{kin}(\bar{u})}{\dot{E}_{kin}(u(t))} = \frac{\frac{3}{2}B^2}{1 + \frac{3}{2}B^2} \tag{A.2g}$$

And so, the larger the amplitude of the fluctuations in the flow, B, the larger the error that is introduced. As an example, for a flow $u(t)$ where $B = 0.2$, the flow of kinetic energy will be underpredicted by 6 %, if for the calculation the mean velocity is used.

In practice the magnitude the fluctuations, B, is unknown. For future work however, an estimate for B can be derived from LDA measurements as LDA can at high frequency, measure the actual velocity.

A.3. Nondimensionalization of Navier Stokes for non-inertial f.o.r.

Sardar (2001, p. 17) non-dimensionalized the Navier Stokes equation for a non-intertial frame of reference, presented below. It was done in a study concerning centrifugal fans, which is why a non-inertial frame of reference was used. The last three terms represent the body forces, Corioles forces and the centripetal forces respectively.

$$\begin{array}{llllllllll} x^* = x/L; & y^* = y/L; & z^* = z/L; & r^* = r/L; \\ U^* = U/U_\infty; & V^* = V/U_\infty; & W^* = W/U_\infty; & \\ p^* = p/p_\infty; & t^* = t/\tau; & B_k^* = B_k/g; & \tau = 1/\Omega \end{array}$$

Figure A.1: The geometric and flow parameters of the Navier Stokes equation in Equation A.3 are normalized using these ratios.

$$\frac{\partial \overline{u}}{\partial t} + \overline{u} \cdot \nabla \overline{u} = -\frac{\nabla p}{\rho} + \upsilon \nabla^2 \overline{u} + \overline{B}_f - 2\Omega \times \overline{u} - \Omega \times (\Omega \times \overline{r}) \tag{A.3}$$

Substituting all variables shown in Figure A.1 into Equation A.3, and dividing by U_∞^2/L results in the following non-dimensional form of the Navier Stokes equation:

$$[Str]\frac{\partial u^*}{\partial t^*} + u^* \cdot \nabla u^* = -[Eu]\nabla p^* + \frac{\nabla^2 u^*}{[Re]} + \frac{B_f^*}{[Fr^2]} - [Str](\Omega^* \times u^*) - [Str^2](\Omega^* \times \Omega^* \times r^*) \tag{A.4}$$

Where the terms in square brackets are the non-dimensional groups relevant to this problem:

$$Re = \frac{\rho\, u\, D_h}{\mu} \qquad Str = \frac{f\, D_h}{u} \qquad Eu = \frac{\Delta p}{\rho\, u^2} \tag{A.5}$$

B

Appendix B

In Appendices B.1, B.2 and B.3 the results are shown for the measurement positions reffered to as B, C and D. These positions are defined in Table 5.1 and Figure 5.8.

B.1. Results: Position B

In Figure B.1b and B.1b the u and w velocity components are plotted for Position B (see Section 5.3). The measurement method used here was LDA. Generally, the results are as expected, considering the data that has been presented in the previous section for position A. On the top left however (ranging from $Y = -127$ to $-30\,mm$) both plots show some strange behavior.

A possible explanation for it might be the trajectory of the laser beams used to characterize the flow: For measuring the w-component the top laser must pass through the top wall of the channel. For measuring the u-component, the laser closest to the diffuser throat must pass through the top channel wall as well, considering that at this position B the channel height increases over X. Note that the LDA system was positioned on to the side of the channel of positive Y. This is explained in more depth in Section 4.3.5.

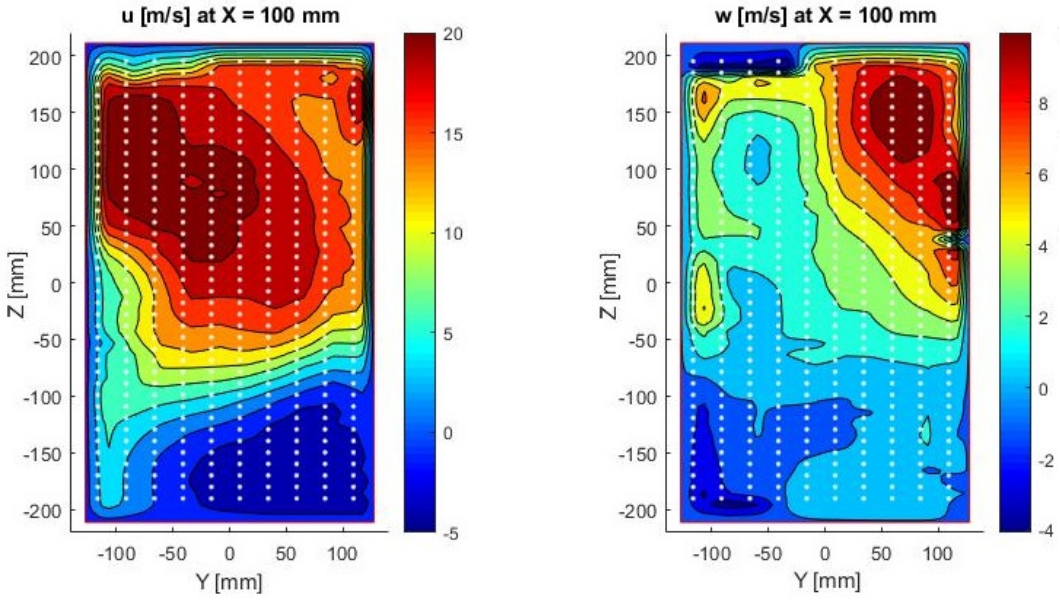

(a) u (b) w

Figure B.1: Results of a LDA measurement in the plane of $X = 100\,mm$ (position B).

B.2. Results: Position C

At position C PIV measurements where performed, and so using the method of combining the data gathered in the horizontal and vertical PIV-planes (see Section 4.4.4), again a $3D3C$ description of the mean velocity field was found. In Figures B.2a, B.2b & B.2c the three mean velocity components are shown, for some cross section within the volume characterized. Again the swirling secondary motion of the jet can be seen. Figures B.3a & B.3b again show the mean velocity field, the first one gives the raw data. The latter one, presents corrected data, that better shows the swirling motion.

A correction was formulated (the term in brackets, in Equation B.1), that would be subtracted from the w that was measured; it was the measured u multiplied with the vertical distance from the center line divided by the horizontal distance from the point where the inner top wall and inner bottom wall would hypothetically coincide. In other words, the vertical velocity component that is already expected from the widening of the duct is subtracted from the measured vertical velocity, shown in Figure B.3a. This method gave a very intuitive result, again showing the swirling motion around the jet, in a more easily fashion than via plotting ω_X.

$$w_{i,j,k}^{modified} = w_{i,j,k} - \left(u_{i,j,k} \cdot \frac{Z_k}{(X_i - X_{focal})}\right) \tag{B.1}$$

In Figures B.4a, B.4b and B.4c all components of the vorticity are given. In the middle one of the three a region of high vorticity is present. It indicates a rolling motion, along the line of $Y \approx 0\,mm$, where the above flow would flow out of the plane of the paper. This again goes hand in hand with the large recirculation zone described in Section 5.1. Lastly for position C, in Figure B.5, the turbulence intensity is plotted. It can be seen that along the (same) line of $Y \approx 0\,mm$, a high level of fluctuations is present. This is the shear layer separating the jet from the backflow.

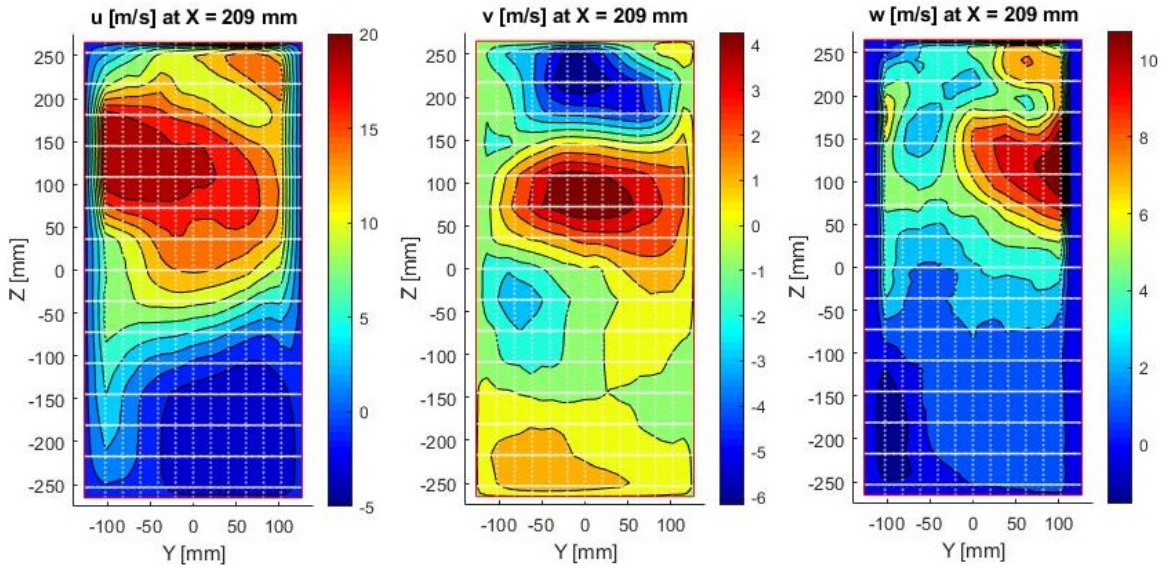

(a) u (b) v (c) w

Figure B.2: These are the results of PIV measurements, and combining the data to a $3D3C$ description of the mean velocity field, shown here for a single cross section.

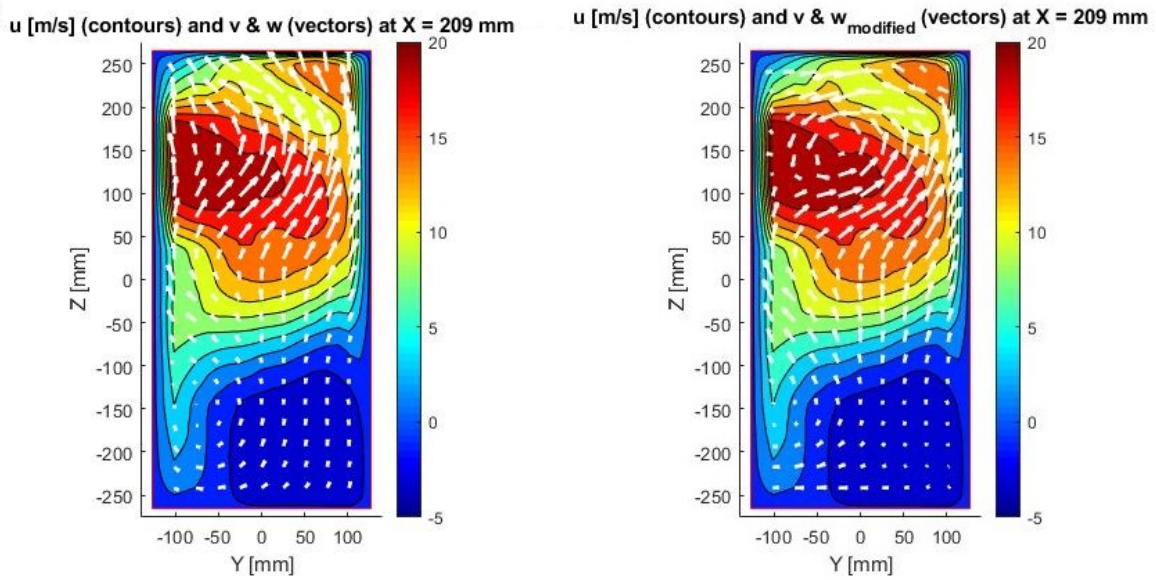

(a) Measured velocity field. (b) Modified velocity field.

Figure B.3: All three velocity components in a single cross section. The left one present the data as measured, whereas in the right one the w component has been modified. The goal of this was, to more clearly show the rotation in the flow. The contours give u, the vectors give v and w.

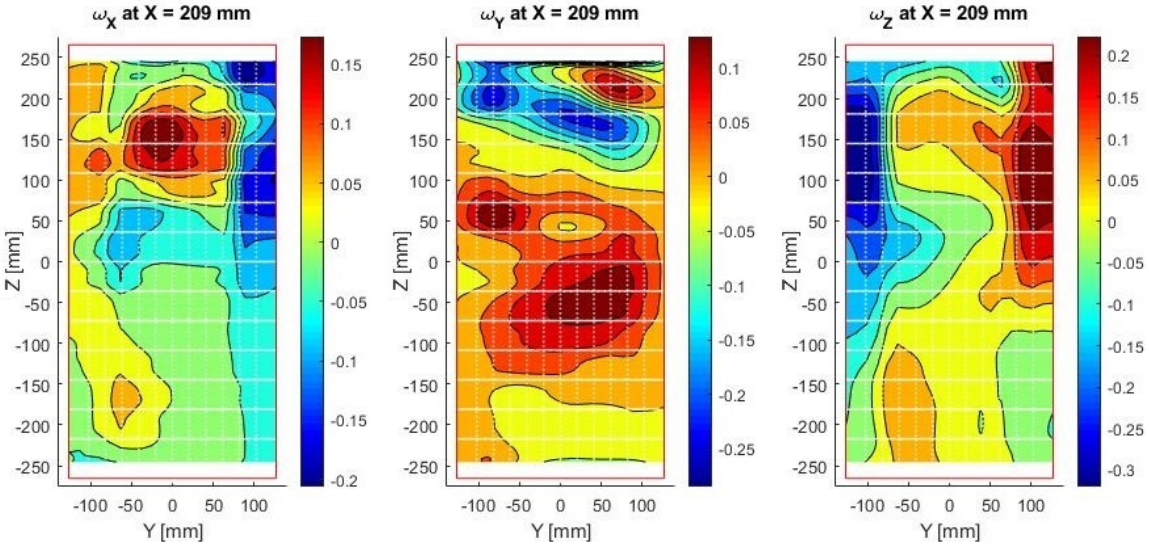

(a) The X-component. (b) The Y-component. (c) The Z-component.

Figure B.4: All three components of the vorticity, derived from PIV measurements.

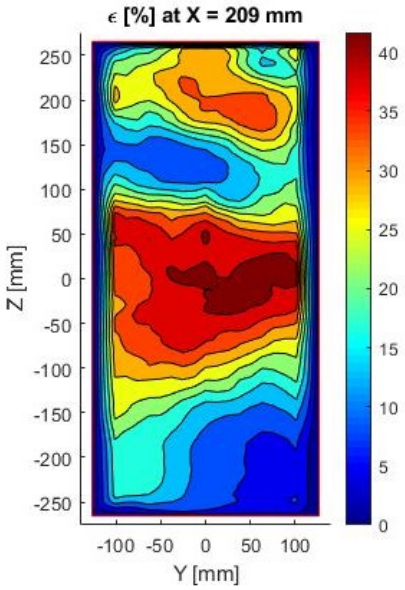

Figure B.5: The turbulence intensity in percentages, derived from the PIV measurements.

B.3. Results: Position D

In Figure B.6a the u-component of the flow is presented. Once more, the jet can clearly be seen. Once more, a swirling motion of this jet can be seen when also looking at Figure B.6b. The turbulence intensity (see Section 4.5.2 for the definition used) is plotted in Figure B.6c. A shear layer below the jet can be seen, pointed out by the high turbulence intensity centered around $Z = 150\,mm$.

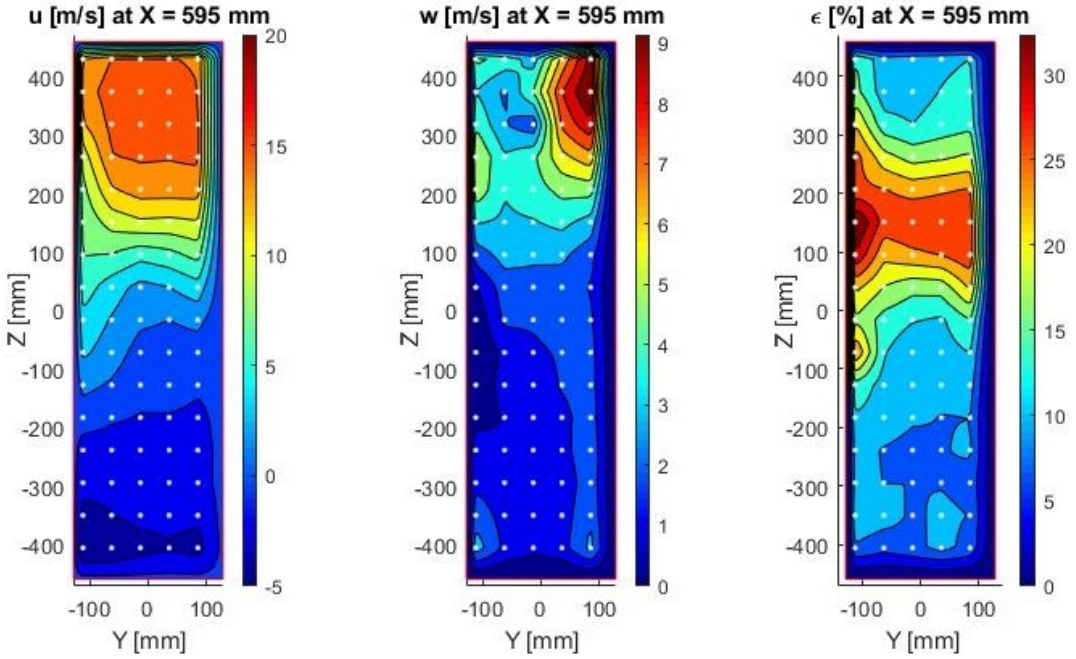

(a) The u velocity component. (b) The w velocity component. (c) The turbulence intensity.

Figure B.6: The results of LDA measurements at position D.

Bibliography

AMCA. Fans and Systems (Publication 201-02). 2007. URL https://www.techstreet.com/hei/products/preview/1133885.

RD Blevins. Chapter 7.4. In *Applied Fluid Dynamics Handbook*, chapter 7.4 & 7.5, pages 144–155. Van Nostrand Reinhold Co., 1984.

Klaus Brun and Rainer Kurz. Analysis of Secondary Flows in Centrifugal Impellers. *International Journal of Rotating Machinery*, pages 45–52, 2005.

Casals Ventilation. Specifications of MBRC 40/12 M4 0.75kW, 2018. URL https://fanware.casals.com/50/fans/199.

Dantec Dynamics. BSA flow software, 2019a. URL https://www.dantecdynamics.com/bsa-flow-software-for-lda-and-pda.

Dantec Dynamics. DynamicStudio, 2019b. URL https://www.dantecdynamics.com/docs/products-and-services/fluid-mechanics/piv/0455_v1_DS_DynamicStudio%20Base%20Package.pdf.

J. C. Gibbings. The pyramid gauze diffuser. *Ingenieur-Archiv*, 42(4):225–233, 1973. ISSN 00201154. doi: 10.1007/BF00533610.

I E Idelchik. *Handbook of hydraulic resistance*. BHB, 1986. ISBN 9781567002515.

Karanja Kibicho and Anthony Sayers. Experimental Measurements of the Mean Flow Field in Wide-Angled Diffusers: A Data Bank Contribution. *International Journal of Science, Engineering and Technology*, 33(September):342–347, 2008.

S Kline and R Fox. *Optimum design of straight-walled diffusers*. Dept. of Mechanical Engineering Stanford University, Stanford Calif., 1958.

Ola Logdberg. Vortex generators and turbulent boundary layer separation control. 2006.

Mathworks. Interpolation for 3-D gridded data in meshgrid format, 2019a. URL https://nl.mathworks.com/help/matlab/ref/interp3.html.

Mathworks. Numerical gradient, 2019b. URL https://nl.mathworks.com/help/matlab/ref/gradient.html.

C.A. Moore and S.J. Kline. Some effects of vanes and of turbulence in two-dimensional wide-angle subsonic diffusers. *National Advisory Comittee for Aeronautics*, 1958.

M. N. Noui-Mehidi, J. Wu, I. D. Šutalo, and C. Grainger. Velocity distribution downstream of an asymmetric wide-angle diffuser. *Experimental Thermal and Fluid Science*, 29(6):649–657, 2005. ISSN 08941777. doi: 10.1016/j.expthermflusci.2004.10.002.

Jared Remster, David Ma, Omer Hashmi, and Goutam Shahani. Selecting the " Best " Fired Heater. 2013.

Robert Jorgensen. *Fan Engineering*. Howden North America Inc., 8th edition, 1982.

B. Sahin and A. J. Ward-Smith. The use of perforated plates to control the flow emerging from a wide-angle diffuser, with application to electrostatic precipitator design. *International Journal of Heat and Fluid Flow*, 8(2):124–131, 1987. ISSN 0142727X. doi: 10.1016/0142-727X(87)90011-7.

Asad Sardar. *Centrifugal fans: Similarity, Scaling Laws, and Fan Performance*. PhD thesis, State University of New York, 2001. URL http://www.turbulence-online.com/Publications/Theses/Sardar01.pdf.

Frank White. *Fluid Mechanics*. McGraw-Hill, 2011. URL https://docs.google.com/file/d/0B9JtpWUzKcwkNC11OC1mQ0NzZjg/edit?pli=1.

Gherardo Zambonini. *Unsteady dynamics of corner separation in a linear compressor cascade*. PhD thesis, 2016.